Kiepenheuer-Institut für Sonnenphysik

Document code: EX/PL-SNT/125

File name:
D80.2_Final_Proposed_Instr_Concepts.pdf

Date: May 29, 2017

Project Ref.: 312495

PROJECT

SOLARNET

TITLE

FINAL PROPOSED INSTRUMENT CONCEPTS AND OPERATION PLAN

WORK-PACKAGE (DELIVERABLE NR)

WP80: SYNOPTIC OBSERVATIONS: SOLAR PHYSICS RESEARCH INTEGRATED NETWORK GROUP – SPRING

(D80.2)

AUTHORS LIST

Name	Function
Sanjay Gosain	WP80 Lead Scientist
Markus Roth	WP80 Leader
Frank Hill	WP80 Participant
Joachim Staiger	WP80 Scientist
Haosheng Lin	WP80 Participant
Wolfgang Zima	WP80 Scientist
Dirk Soltau	WP80 Scientist
Miroslav Klvaňa	WP80 Participant
Michal Sobotka	WP80 Participant

APPROVAL CONTROL

Control	Name	Organization	Function	Date
Prepared	Sanjay Gosain	KIS	WP80 Lead Scientist	28/02/2017
Revised	Markus Roth	KIS	WP80 Leader	27/03/2017
Approved	Markus Roth	KIS	Technical Manager	30/03/2017
Authorized	Manuel Collados	IAC	Proj. Coordinator	29/03/2017

DOCUMENT CHANGE RECORD

Issue	Date	Change Description
01	28/02/2017	Initial Issue
02	27/03/2017	Final Issue

TABLE OF CONTENTS

SUMMARY

High-resolution telescopes (such as SST, GREGOR and the future EST and DKIST) allow observations of only a small fraction of the solar surface. Real-time context data showing the large-scale dynamics and magnetism at different layers of the solar atmosphere are crucial to understand the global behavior of solar phenomena. However, despite the amount of information coming from space and ground-based full-Sun telescopes, real-time information about the variation of important parameters such as velocities, magnetic field and intensity at different solar layers is still lacking. To this aim, a network of telescopes with a small aperture but a large field-of-view can provide useful data to prepare observing campaigns with large-aperture high-resolution telescopes and complement the data taken with them. Distributed in a world-wide network, these small apertures can represent an invaluable supporting tool for coordinated observations with the major infrastructures. While space platforms can also provide nearly-continual solar observations, networks formed out of ground-based telescopes have several advantages, e.g. the network instrumentation can be repaired when it fails or upgraded when new technology and/or science requirements demand it; and the network lifetime is in principle infinite.

This document describes the technical concept developed under Solarnet WP80 “Synoptic Observations: Solar Physics Research Integrated Network Group (SPRING)” for the setup of a new ground-based network for continuous solar observations serving a large research community.

LIST OF ABBREVIATIONS

AR	Active Region
BiSON	Birmingham Solar Oscillation Network
CM	Collimated Mount
CME	Coronal Mass Ejection
DKIST	Daniel K. Inouye Solar Telescope
EST	European Solar Telescope
FDIS	Full-disk
FPI	Fabry-Perot Interferometer
FSR	Free spectral range
FW	Filter Wheel
FWHM	Full width at half maximum
GONG	Global Oscillation Network Group
HELLRIDE	Helioseismic Large Region Interferometric Device
ISS	Integrated Sunlight Spectrometer
LCVR	Liquid crystal variable retarder
MDI	Michelson Doppler Imager (aboard the Solar and Heliospheric spacecraft SoHO)
NIR	Near Infrared
NSO	National Solar Observatory
PCU	Polarization Calibration Unit
PMOD	Physikalisch-Meteorologisches Observatorium Davos
RA	Right Ascension
SDO	Solar Dynamics Observatory
S_MAG	Magnetograph Instrument for the SPRING Network
SIM	Spectral Irradiance Monitor
SOLIS	Synoptic Optical Long-term Investigations of the Sun
SORCE	Solar Radiation and Climate Experiment satellite

SPRING	Solar Physics Research Integrated Network Group
SRD	Science Requirement Document
SSI	Solar spectral irradiance
TM	Telecentric Mount
TSI	Total solar irradiance
UV	Ultra-violet
VTF	Visible Tunable Filter
VTT	Vacuum Tower Telescope

1. INTRODUCTION

Sun – our day time star is crucial for life on Earth. It has been realized that it is the only star that is available to us for detailed observations, thus it has been sometimes called an astrophysical laboratory. The phenomena that we observe on Sun are easily extrapolated to other similar stars that we can never resolve. An important property of the Sun is that it is a variable star. The eleven-year activity cycle and twenty-two-year magnetic cycle are most prominent variable time-scales. On smaller time-scales periodicities of one and two years have been reported in various activity indices. A prominent periodicity of ~155 days, also known as Reiger period, has been found in magnetic flux emergence as well as solar flares. Our understanding of the physical processes in the Sun that lead to such variability is very poor. Careful measurements of the Sun's properties, not only on its surface but also in its interior by helioseismology, over many solar activity cycles are crucial to decipher the internal workings of the Sun.

Only with long-term systematic observations the eleven and twenty-two year cycles of the Sun could be discovered. More recently, in the last few decades by monitoring Sun's radiative output we have learnt that the solar constant is not constant, i.e., the total solar irradiance (TSI) varies with the eleven-year activity period by a small amount of 0.15%. Explanation of TSI is still being sought after very vigorously. Similarly, from many years of careful monitoring of solar surface oscillations (Sun's heartbeats) helioseismologists have revealed the plasma flow properties in the solar convection zone. Zonal bands of faster and slower rotation have been found and their slow migration towards solar poles and equator remain a puzzle. More recently the nature of solar meridional flow, its variability, hemispheric asymmetry and cell structure are being hotly debated, as these flows have strong implications for our understanding of solar dynamo mechanism, which is believed to be responsible for governing the generation of solar magnetic fields in active latitudes.

Further, in recent decades humans have become extremely dependent of space technologies such as communication satellites for mobile phones, global positioning satellites, television, internet, meteorological satellites for weather forecasting, etc. Such technologies in space, including infrastructure on ground such as power grids are extremely vulnerable to solar eruptive phenomena such as solar flares and coronal mass ejections (huge blobs of magnetized plasma). Such phenomena, when they are directed towards Earth, can severely impact the Earth's magnetosphere and cause large scale geomagnetic storms. Predicting such geomagnetic storms and radiation environment near Earth due to the Sun is called space-weather. For reliable operation of space and ground based technological infrastructures as well as for the safety of astronauts during manned space missions and passengers/crews during commercial flights over Earth's polar regions, we need to monitor solar variability on short time scales and in near real time. Such careful monitoring of the Sun is therefore very necessary to make reliable space weather forecasting.

In the era of large aperture (albeit limited field-of-view) ground-based solar telescopes, a robust ground-based network of synoptic research facilities is lacking. The only ground based synoptic facilities that exist presently for careful long-term monitoring of solar oscillations and surface magnetic field vector are aging GONG network and SOLIS (single-node facility), respectively. Both are run by National Solar Observatory, USA. While space based observatories such as SDO can provide synoptic observations of the Sun, these cannot be relied upon for space-weather prediction as they are themselves vulnerable out there. Further, the failures of satellite observatories cannot be predicted and unlike ground-based facilities these cannot be fixed or upgraded.
Studies confirm that best duty cycle of observations can only be achieved by a network approach such as GONG network (a network of six sites distributed globally). While GONG is still operational its scope is somewhat limited, as it was basically designed in the nineties for helioseismology in single spectral line.
SPRING is intended to be the first synoptic-network facility to be built for carrying out integrated solar physics research. It will benefit from technological improvements in last few decades in the field of detectors, optical fabrication, control systems, computational power and data bandwidths, which will enable observations of much better quality for much wider research community, including multi-wavelength helioseismology and space weather research.

2. SCIENCE GOALS

2.1 Introduction

The main purpose of this document is to define the technical science-driven requirements for the data products to be delivered by the Solar Physics Research Network Group (SPRING). These science requirements for SPRING are described in deliverable D80.1 and for completeness they are summarized in the following.

Solar physics currently aims at solving the following big scientific questions:
• How is the solar magnetic field generated, maintained and dissipated?
• How are the solar corona and the solar wind maintained and what determines their properties?
• What triggers transient energetic events?
• How does solar magnetism influence the internal structure and the luminosity of the Sun?

For answering these questions it requires both high-resolution observations with upcoming future telescopes of the 4m class, but in addition synoptic observations can strongly contribute to answer these questions by addressing research topics that can only be answered by having a full-disk view on the sun. Besides providing the context information to high-resolution solar telescopes, such a synoptic network of smaller-size telescopes with a view on the whole solar surface can:
• Discriminate between solar dynamo models

• Determine the characteristics of angular momentum transport inside the Sun
• Observe, identify and characterize magnetic reconnection
• Determine the role of induction effects near the surface for the global field
• Observe, identify and characterize acoustic and magneto-acoustic waves in the upper atmosphere
• Determine the role of the interaction of interior flow and magnetic fields
• Enable statistical analyses with large sample sizes
• Establish reliable space weather prediction
• Compare the Sun with stars which differ in magnetic activity through asteroseismology

In order to determine the scientific and technical requirements for such a new network their definition was elaborated by four working groups that addressed the four main scientific themes:
(i) Synoptic magnetic fields
(ii) Solar seismology
(iii) Transient events
(iv) Solar awareness
Each of these four themes itself encompasses a variety of analyses, with varying sensitivity to instrumental and system parameters, which shall be presented in the following sections

2.2 Science Drivers

2.2.1 Synoptic Magnetic Fields

Sunspot and the chromospheric filaments (prominences) are the hallmark of solar activity and cycle. These (and other similar type) features were subject of numerous studies, and we now know more about their formation and evolution than just a few years ago. Still, many questions about the long-term changes in properties of these features remain unanswered. Do mean properties of sunspots, e.g., their maximum field strength, radius, contrast with the photosphere, formation depth etc. remain constant over the long period? How do the properties of the large-scale magnetic field affect the formation of the chromospheric filaments? Can we predict the most likely location of future coronal holes or a chromospheric filament based on the evolution of the magnetic field of active regions? How do the properties of the magnetic field change in bipolar groups with the phase of the solar cycle, e.g. compactness or looseness of the leading or following polarity, and their mutual inclination relative to vertical direction? Any systematic changes in these properties are likely to reflect the changes in the toroidal field at the location of the sunspot formation zone, e.g., in the overshoot region, and thus, will be useful for dynamo modeling of the solar cycle.
Overall, the solar atmosphere is a single system unified by the presence of large-scale magnetic fields. Topological changes in the magnetic field that occur at one place may have consequences for coronal heating and eruptions for other, even remote locations. To better understand the large-scale connectivity and its changes over a solar cycle requires long-term observations of vector magnetic fields. The

connectivity is likely to be affected by the level of activity, reflected in the number of active regions, and the large-scale pattern of the magnetic field, e.g. the presence and absence of filaments, large-scale neutral lines and coronal holes. Again, this will require synoptic long-term observations. Changes in the large-scale connectivity may lead to the remote triggering of flares and filament eruptions as well as enhanced coronal heating in localized areas distant from areas of magnetic field changes due to new flux emergence.
In this sense a full disk vector magnetograph will serve as a context imager for high resolution instruments as DKIST and EST to facilitate a better target selection by providing at first an indication of the sunspot penumbra development or a new flux emergence, which then allows studying these processes with higher spatial and temporal resolution.

Mission
The mission of the magnetograph instrument for the SPRING Network (S_MAG thereafter) is to take synoptic full disk measurements of the Sun at all polarization states sufficiently well enough to derive the full magnetic field vector in areas of weak (i.e., quiet Sun) and strong (i.e., sunspots) magnetic field with moderate spatial and temporal resolution (1 arc second pixel size and one hour cadence) in the wavelength range that includes the spectral lines that form in the photosphere and the chromosphere with relatively high spectral sampling (< 2.5 pm). The S_MAG design should include a flare-mode to increase cadence to 10 minutes at the expense of spatial size of recorded area. The S_MAG design should ensure high stability of polarimetric measurements over the lifetime of the instrument, to allow an easy upgrade of key components whenever needed, and at a low level of instrumental polarization, or alternatively a simple observing procedure to determine the instrumental polarization.
In the end, the overarching assumption is that S_MAG is the synoptic full disk magnetograph for the solar physics community to study the long-term and large-scale evolution of solar magnetic fields and to provide the context data in support of various missions and for Space Weather forecast.

2.2.2 Solar Seismology
Since the magnetic field and activity cycle must originate from inside the Sun, knowledge of the changes in the dynamics and structure of the solar interior on decadal time scales is vital if we are to understand the physical mechanism of the solar dynamo. This information can only be obtained from long-term helioseismic observations. In this section we briefly review the requirements for solar seismology.
Information about the changes in the solar structure large scale flows, e.g. rotation rate and meridional flow is obtained from the solar eigenoscillations. The dominant source of changes in these global eigenmodes is the differential rotation of the Sun as a function of depth and latitude. Solar cycle variations of the frequencies are primarily the result of the zonal flow known as the torsional oscillation. There is evidence that the position as well as the transition of the rotation rate across the

tachocline, where the internal solar rotation rate changes from differential to rigid, shows some temporal variations. A second shear zone in differential rotation is in the sub-surface layers. In these two shear zones the solar dynamo could operate.

Recent measurements of the meridional flow reveal its extent over the whole convection zone with a possible multi-cellular structure in latitude and depth. Determining precisely the amplitudes of the convective flows and the structure and temporal evolution of the meridional flow will be one of the research foci of the coming years.

A major research area of solar physics concentrates on local helioseismology, where the oscillations are analyzed in a variety of techniques that do not consider the Sun as a global entity but instead focuses on specific localized areas. In terms of long-term solar cycle variations, these techniques have the great advantage that they are not restricted to results that are symmetric across the solar equator. They can thus reveal north-south hemispheric asymmetries in both the zonal and meridional flows that can be correlated with the hemispheric asymmetries in the magnetic field discussed earlier. Recent assessments of the large- and small-scale dynamics in the convection zone suggest smaller amplitudes for such convective flows than reported from theoretical models. This raises fundamental questions how a star maintains its heat transport and redistributes its angular momentum that lead, e.g. to the observed differential rotation.

Helioseismic studies of the internal structure focus primarily on inversions for the wave speed, which depends on the temperature, composition, and magnetic field of the internal solar plasma. Unfortunately, it is not possible to reliably separate the effects of these three physical quantities since, unlike for velocity, they do not depend on the propagation direction of the wave. Nonetheless, it is possible to detect changes in the subsurface wave speed over the cycle. These changes are usually attributed to the surface magnetic field, but they may well have an additional thermal component. In addition, deeply situated magnetic or thermal variations at the base of the convection zone could explain some of the observed variations.

Mapping the structure and evolution of active regions is a challenging effort, too, since acoustic waves passing through them experience strong modifications. This results in ambiguities in the various helioseismic interpretations of flows and structures within sunspots and their surroundings. New constraints that could be incorporated into helioseismic analyses may come from vector magnetic field data along with the velocity signal of the wave field measured in multiple heights of the atmosphere.

Such studies are closely connected to seismic studies of the solar photosphere, chromosphere, and corona. High-frequency waves above the acoustic cut-off frequency of the Sun propagate into these layers. Furthermore structures like sunspots and prominences show oscillations on their own. Studies of these high-frequency waves in the solar atmosphere and magneto-acoustic waves in sunspots and magnetic loops promise new insights in the structure, formation, and evolution of solar activity phenomena.

Mission

Enabling improved and continued measurements for studying the internal dynamics and structure of the Sun requires a SPRING Doppler Imager. The near-surface but invisible layers of the Sun are changing over several timescales. To draw these conclusions required data that were available over several decades. In spite of this, there are still unanswered questions and the need for even longer data sets: We know that the underlying Hale solar activity cycle actually covers 22 years rather than the 11 years on which we see the sunspot number vary. We have not yet had consistent helioseismic measurements over a single Hale cycle. This needs to be achieved with the new SPRING Doppler Imager. The effects that we need to measure are not large and require consistency in the data over very long periods of time. We must be confident that observed variations are genuinely due to the Sun and not a consequence of a change in the observing methods. A key attribute of any robust detection is that there are multiple, independent observations of it. We have already seen this in the case of the quasi-biennial signal. On the other hand, it is important that instrumentation changes to take advantage of new improvements in technology. These changes should be arranged so that there are always periods of overlap for inter-calibration studies. We absolutely must have long-term consistent solar observations if we are ever going to understand the solar activity that underlies the potentially harmful effects of space weather.
In order to extend the helioseismic capabilities to probe the structure and flows below and around sunspots, and magnetic loops, the solar oscillations need to be observed in multiple spectral lines from the photosphere to the chromosphere and at a higher temporal cadences in the order of 10 s.

2.2.3 Solar Flares and Transient Events

The main sources of major disturbances of space weather in the heliosphere are violent eruptions occurring on the Sun. Solar flares and coronal mass ejections (CMEs) are the most energetic eruptions in our solar system. They are driven by strong localized magnetic fields concentrated, at the photospheric level, in sunspots, which vary in occurrence frequency and size during the 11-year solar cycle. Additionally, this variation in the solar magnetic field also relates to an 11-year cycle in the occurrence of strong space weather events and storms at Earth. Coronal mass ejections are huge clouds of magnetized plasma expelled into interplanetary space with speeds of some hundred, up to a few thousand kilometres per second. They often occur in close association with erupting filaments/prominences.
Flares manifest as radiation enhancements across most of the electromagnetic spectrum, as a result of accelerated particle beams and excessive heating of the different layers of the solar atmosphere. Flares, CMEs, and filament eruptions are thought to be different manifestations of the same underlying physical process, namely the release of vast amounts of magnetic energy by the process of magnetic reconnection. However, they may or may not occur together, with the association rate being a steeply increasing function with flare importance. In the strongest and thus most geo-effective events, typically both a flare and a CME are observed. For instance, recent statistical studies of filament eruptions were showing that about 55% of the 98 events analyzed were associated with CMEs and that active region filament eruptions have considerably higher flare association rates (95%) compared to the

eruption of quiescent filaments (27%). In general, the time sequence indicates that firstly a filament is activated, starts to rise, and within some tens of minutes, a flare and/or a CME occurs. Phenomena commonly associated with these energetic processes are filament rise, particle acceleration, bright ribbons in the lower atmospheric layers, and post-flare loops.

Current models assume that a flare is produced through magnetic reconnection associated to the formation of a current sheet. The intermittent nature of the non-thermal electron beams emitted during a flare can result in variations in chromospheric and coronal emission over very short timescales. These variations, appearing for instance in lines such as the Balmer series, CaII H, K, and in the 1560 nm continuum, arise from a combination of energy and ionization imbalance and chromospheric condensation. The chromospheric plasma is heated to very high temperatures, creating an overpressure making it expand into the overlying post-flare loops.

Flare ribbons observed in chromospheric lines are produced as a response of the dense layers of the atmosphere to bombardment from high energy particles (electrons, protons, and ions) accelerated in the flare reconnection site. The spectral line intensities, varying on sub-second timescales, depend strongly on the energy fluxes of these particles due to the heating of the chromospheric plasma and the non-thermal collisional excitation of the atomic levels. One of the possible diagnostic mechanisms capable of creating polarization in chromospheric lines is therefore the impact line polarization. The impact polarization of these lines would be sensitive not only to the distribution function of the particles, but also to the distribution function of the return neutralizing current. Spectropolarimetry of flare ribbons carried out with THEMIS indicates that the line intensities and polarization may also be generated by the return current.

White-light flares represent the most extreme conditions reached in solar flares with energies comparable to some of their stellar counterparts. Although they are not believed to be fundamentally different from lower energy events, they are rarely observed. There is a distinct time delay between the white-light emission in the core of the flare kernel and its outer region (halo). This suggests that the core is heated directly by the electron beams while the heating of the halo is a secondary effect and raises the prospect of using white-light emission as a diagnostic for the energy of the electron beams. It has been suggested that all flares have some white light components which are only resolvable with ground-based instruments. A synoptic study of flares with decent spatial and temporal resolutions afforded by a ground based synoptic network would aid in verifying/refuting this idea and would improve our understanding of the radiative back-warming process that are believed to be responsible for this white light emission in less energetic flare events.

Magnetic configuration and evolution

The free energy required to power the flare event implies that there must be a strong deviation of the magnetic field from its potential state. Solar flares occur preferentially in active regions with strong magnetic shear and regions with complex magnetic morphology. Magnetic complexity can be evaluated by studying the fractal dimensions of active regions and by estimating the magnetic shear along the polarity

inversion line. Active regions with higher complexity produce flares more frequently and larger flare events.
Magnetic helicity is a useful quantity for determining the degree of instability reached by a filament, leading to a filament eruption and possibly to a flare. This parameter quantifies how much a set of magnetic flux tubes are sheared and/or wound around each other. In a plasma with high magnetic Reynolds number, the magnetic helicity is almost conserved on a time scale smaller than the global diffusion time scale, even when considering the effects of magnetic reconnection. Therefore, in the solar corona, the magnetic helicity can be injected only through the photosphere by newly emerging flux or by horizontal motions of the field-line footpoints, while its excess can be expelled only by CMEs. Several recent studies have stressed the importance that knowledge of the magnetic helicity variation might have in eruptive phenomena. Therefore its determination is crucial to predict filament eruptions and the associated flares and/or CMEs.
The lack of variations in the photospheric magnetic field during the flare has led to the prevailing idea that the free energy that drives the flare comes from the currents in the outer atmosphere, where most of the energy release occurs. Recent observations with GONG and MDI show abrupt, permanent changes of the photospheric magnetic field associated with the largest. The rate of change is tens of Gauss per minute and can be as high as 200 Gauss per minute. These variations may be due to changes in the direction or strength of the magnetic field or a combination of both. However, it is impossible to resolve this issue with the GONG and MDI observations, which are limited only to the line-of-sight component of the field. High cadence vector magnetograms are essential for this problem.

Mission
Solar flares vary in magnitude and duration from rare white-light events to common microflares and other sub-arcsec rapid energy releases. The associated CMEs are the primary cause of adverse space weather conditions which can in turn have an impact on the safety of Earth-orbiting satellites and astronauts. Although flares are now viewed as high-energy processes, which take place mainly in the corona, the response of the photosphere and chromosphere to the flare-energy transport is very complex. The energy radiated from the lower atmosphere forms an important part of the flare energy budget and it is of high importance for diagnostics of the particle beams originating at the coronal reconnection site. It is therefore essential that the photospheric and chromospheric signatures and processes involved are well understood.

Current models of the flare line and continuum emission incorporate the solution of hydrodynamics, statistical equilibrium, and radiative transfer equations. The models show that the increased transition region and coronal density lead to dramatic increases in the line- and continuum emission in UV and optical wavelengths. In these simulations, the hydrogen continua initially decrease in intensity within the first second of the flare before they increase steeply later in the event. This is the result of the non-thermal ionization from the electron beam. The timescales of the continuum dimming depend strongly on the energy of the incoming electrons. Therefore, it is

crucial to obtain observations from the very beginning of the flare with very high temporal resolution of 0.1 s.
Since the chromospheric spectral lines susceptible to the impact polarization are formed under non-LTE conditions and they are sensitive to scattering line polarization, the linear polarization observed in flares can also be interpreted as being due to radiation transfer effects. Such observations can provide essential diagnostic information for the energetics and dissipation mechanisms of the accelerated particles and reveal the relative importance of different polarizing mechanisms.
It is worth noting that it is crucial to capture (almost) simultaneously the state of the solar atmosphere in multiple layers, in order to avoid cross-talk introduced by the rapid evolution of both solar structures and Earth's atmosphere seeing. Also, an instrument that would provide very sensitive (of the order of 5 Gauss) measurements of the solar magnetic field at different heights would be extremely appropriate to help constrain the magnetic field vector reconstructed by current and future inversion and/or extrapolation software. Such extreme sensitivity and high cadence would prove very important when dealing with rapid changes of the magnetic field associated with the largest flares.

2.2.4 Solar Awareness

2.2.4.1 TSI/SSI

Solar radiation is the principal source of energy entering the Earth system. As such, the variation in the Sun’s radiative output, solar irradiance, is a prime candidate driver of externally driven changes to the Earth’s climate. The total solar irradiance (TSI), i.e. the spectrally integrated radiative power density of the Sun incident at the top of Earth’s atmosphere, has been monitored almost continuously since 1978 through a succession of space borne radiometers and was found to vary on different time scales. Most noticeable is the 0.1% modulation of TSI in phase with the 11 yr solar cycle. Changes 2–3 times larger than this are observed on timescales shorter than a few days. Original time series of measured values differ in terms of the absolute level. For many years, the canonical value of the average TSI was 1365.4 ± 1.3 Wm−2 whereas now the most accurate and generally accepted value is 1361 ± 0.5 Wm−2. Besides, the records from the various instruments also show considerable differences on the decadal trends
Measurements of the solar spectral irradiance (SSI) are not continuous over the satellite era and until recently have concentrated on the ultraviolet (UV) radiation, because of the larger relative variability of SSI below 400 nm and the impact of these wavelengths on the terrestrial atmosphere through radiative heating and ozone photochemistry. SSI variations differ from those observed in the TSI. The variability of visible and NIR (near-infrared) bands barely exceeds 0.5% over a solar cycle; in the near UV and shorter wavelengths variability increases with decreasing wavelength, reaching several percent at 200–250 nm, and several tens of percent, and even more, below about 200 nm. These bands are almost completely absorbed in the Earth’s middle and upper atmosphere and are the primary agent affecting heating, photochemistry, and therefore, the dynamics of the Earth’s atmosphere.

Early satellite measurements of the solar UV variability have shown a qualitatively consistent behavior, which is fairly well reproduced by SSI models. This situation changed with the launch of the Spectral Irradiance Monitor instrument (SIM) onboard the Solar Radiation and Climate Experiment satellite (SORCE) in 2003, which was shortly after the maximum of solar cycle 23. The SORCE/SIM data showed a 2–6 times greater decrease of the UV radiation between 200 and 400 nm over part of the declining phase of solar cycle 23 compared to earlier measurements and models. The larger decrease measured in the UV, which exceeds the TSI decrease over the same period by almost a factor of two, is compensated by an increase in the visible and NIR bands. Variability out-of-phase with solar activity is indeed predicted by some SSI models in the NIR, but with a significantly lower magnitude than found by SORCE/SIM. The inverse variability observed by SIM in a wide integrated band in the visible was, however, unexpected. It can be interpreted as a result of effects induced by the evolution of surface magnetism in the solar atmosphere. However, other observations and analyses of existing long-term SSI data show results in contrast with those derived from SORCE/SIM.

Physics

It was noticed soon after the beginning of routine monitoring of TSI from space, that changes in TSI were closely related to the evolution of different brightness structures on the visible solar disc. These brightness structures (such as sunspots, pores, faculae, plage and network) are manifestations of the solar magnetic field emerging at the Sun's surface.

Models relating variation in solar irradiance at timescales greater than a day to photospheric magnetism have made significant progress in explaining most of the apparent trends in solar irradiance measurements. Most recent results show that models accounting for the variation in solar irradiance by the intensity deficit and excess facilitated by photospheric magnetism replicate up to 92% of the variability in the PMOD TSI composite 1978-2012, including the long-term trends at solar cycle minima, and 96% over cycle 23. The same models also reproduce most of the variability of SSI measured on rotational time scales, especially between 400 and 1200 nm.

Most successfully models consider contributions of different brightness structures to the irradiance change separately. The solar energy output results thus from the sum of the fluxes emerging from all the features observed on the solar visible surface (corresponding to the solar photosphere); the number and type of disk features accounted for depends on the model. Usually these models require the surface area covered by each photospheric component as a function of time, and the brightness of each component as a function of wavelength and of the position on the solar disc.

The main uncertainties in current irradiance models concern the wavelength range 220–400 nm, where the magnitude of the variations differs by as much as a factor of three between existing models, and comparison with SIM measurements. Indeed, the magnitude of the long-term trends derived from the models is smaller with respect to that derived from SIM measurements at almost all wavelengths and even oppose in the visible between 500 and 700 nm and NIR range between 1000 and 1200 nm. Besides, in spite of a general consensus among reconstructions of TSI variations on

the decadal and rotational time scales, the model based estimates of the long-term (secular) change of TSI since the Maunder minimum differ by almost a factor of four. Finally, other mechanisms of solar irradiance variations than effects of surface magnetism have also been proposed, related to physical processes in the solar interior, but both supporting and rebuttal evidences are still lacking.

Mission

Lack of continuous measurements, insufficient overlap between different instruments, and proper calibration of instrument degradation once instruments are in space constitute the main current problems of existing irradiance measurements. On the other hand, overcoming the inaccuracies and shortcomings of current irradiance models still require major efforts to resolve the mechanisms responsible for the measured variations, to improve the spectral synthesis and models atmospheres employed in irradiance reconstructions, and to understand the relationship between indices of solar activity and solar irradiance.

2.2.4.2 Space Weather and Space Climate

Except for localized regions near planets or minor bodies, the heliosphere is dominated by material emanating from the Sun. Space weather and space climate consider the time varying environmental conditions in the heliosphere, including conditions in the near-Earth space defined by the magnetosphere down to the ionosphere and thermosphere, occurring on short- (from second to a few days) and long-term (from tens to thousands of years) time scales, respectively. The technology-dependent society, the human and robotic exploration in space, and Earth's climate are vulnerable to variations of the conditions in the heliosphere. The source of these variations is the Sun. Indeed, the large scale structure and dynamics of the magnetic field in the heliosphere is governed by the solar wind flow, which has its origin in the magnetic structure of the solar corona driven by the emergence of magnetic flux, plasma motions

in the photosphere and transient solar eruptions (flares, CME) in the atmosphere. Most of the flux emerged in the photosphere forms chromospheric or coronal loops that do not contribute to the heliospheric magnetic field carried by the solar wind, but a fraction of flux extends out to form the heliospheric magnetic field, whose variations are an important source of geomagnetic activity. Interplanetary transients and geomagnetic disturbances are related to the changing magnetic fields on the solar atmosphere, which indirectly modulate also the flux of high-energy galactic cosmic rays entering the solar system from elsewhere in the galaxy.

Understanding of the origin of space weather and space climate, and advancing current forecasting capabilities of the events affecting the environmental conditions in the heliosphere, imply a better knowledge of the structure and dynamics of both the magnetic field and large-scale motions in the solar atmosphere on time scales from a few seconds to several decades and even centuries.

Physics

Space weather and space climate research aim to produce reliable forecasts and nowcasts of the conditions in the heliosphere driven by processes on the Sun. This requires understanding of the origin of heliospheric disturbances at the Sun and of the

subsequent effects of their propagation in the interplanetary space. By focusing on the initiation process only, there is still much fundamental research on the Sun as the driver of the space weather and space climate waiting to be done, as both the short- and long-term evolution of the solar magnetic field impose forces affecting the whole heliosphere.

Striking eruptive events that are driven by the evolution of magnetic fields at small scales in the solar atmosphere, such as flares and coronal mass ejections (CMEs), initiate the interplanetary disturbances occurring on the time scales from seconds to a few days. Solar flares are among the most energetic events in the heliosphere. They occur in active regions (ARs), by involving processes at various heights in the solar atmosphere that are powered by the magnetic field. Observations show that the photospheric topology of magnetic field is one of the key factors in determining the evolution of ARs. There is a general trend for large regions to produce large flares, and for more complex regions to generate more numerous and larger flares than other regions of comparable size. Emergence of a bipolar region that interacts with preexisting magnetic field in the corona, and activation of a filament with destabilization in the subsisting magnetic region, are identified as precursors events preceding the onset of flares. However, the precise conditions required to create the enormously energetic (up to 1033 erg on the timescale of hours) flare events are as yet unknown. On the other hand, CMEs consist of large structures containing plasma and magnetic fields that are expelled from the Sun into the heliosphere. They remove built-up magnetic energy and plasma from the solar corona. Most of the ejected material comes from the low corona, although cooler, denser material probably of chromospheric or photospheric origin is also sometimes involved. The CME plasma is entrained on an expanding magnetic field, which commonly has the form of a flux rope.

Initiation of flares and CMEs follows storage of energy in closed magnetic field regions on the solar atmosphere over a certain period of time. Then they consist of a series of processes, including reconnection, particle acceleration and propagation, waves, etc.

and ending by a restructuring of the magnetic configuration with a release of magnetic energy. We still do not know neither the signatures of the energy build-up in active regions or the triggers of the energy release that can lead to large flares and CMEs. Identification of pre-eruption signatures and triggers is thus crucial in deciding whether and when the event will occur.

In the long-term time scales, the large-scale solar magnetic field introduce cyclic and aperiodic changes in the electromagnetic forces acting in the interplanetary space. It is known that the Sun’s low-order magnetic multipoles play a central role in the evolution of the magnetic field in the heliosphere on time scales from years to centuries. Indeed, the long-term variation of the radial component of the interplanetary magnetic field approximately tracks that of the total dipole moment, with additional contributions coming near sunspot maxima from the quadrupole moment and from CMEs. Recent results indicate that the hemispheric asymmetry in the flux generation and meridional flow contribute to the asymmetric polar fields affecting e.g. the position of the heliospheric current sheet.

In the flux transport dynamo, the origin and evolution of the dipole field are closely related to the emergence of active regions and the subsequent dispersal of their flux over the photosphere. Continuous monitoring of the flux emergence and dispersal in the lower atmosphere is needed to constrain e.g. flux dynamo models, as well as potential field source surface models employed to study the environmental condition within the heliosphere in time.

The mission

Lack of high temporal and spatial resolution observations and low-noise measurements of the magnetic field obtained simultaneously at various heights in the solar atmosphere has prevented the conclusive identification of the fundamental precursor and triggering processes of the magnetic field evolution in AR hosting eruptive events. We still lack a quantitative understanding of how the magnetic complexity in a source region relates to CME productivity.

Similar studies applied to regions hosting flares produced still inconclusive results. On the other hand, direct measurements of the magnetic field in the solar atmosphere date back only late 1950s. Vector magnetic field measurements are available only since 2003.

Therefore, multi decadal- and longer-term variations of the magnetic field properties on the solar atmosphere need to be inferred from other indirect measurements of solar magnetic fields, e.g. time series of sunspot numbers. An improved knowledge of the variation of the magnetic field over the cycle in full-disk observations, as well as of the relation between solar activity indices and field measurements, is needed to improve our current knowledge of the long-term solar variability and its effects in near-Earth space, atmosphere and climate.

2.2.4.3 Sun-As-A-Star

The Sun is the only star for which intensity patterns, plasma motions, and magnetic fields properties can be derived in great detail at various heights in the solar atmosphere, by using direct spectro-polarimetric measurements obtained at high-temporal and spatial resolution, at various spectral ranges. Nevertheless, disk-integrated observations of the solar atmosphere represent important input data to both stellar and solar research. Indeed, analysis of simultaneous disk-resolved and disk-integrated observations of the solar atmosphere allow for investigations of the contribution of individual solar features and physical processes of the solar atmosphere to the solar spectrum. This provides interpretation of stellar spectra with unique data that cannot be obtained from observation of other stars still imaged with insufficient resolution to allow direct measurements of the plasma motions and magnetic fields. Moreover, several programs have been taking regular sun-as-a-star observations on various lines of the solar spectrum since late 1960s and these measurements now constitute a record of the long-term variation in solar activity available for use in models.

The mission

The main objective is to continue the Sun-as-a-star observations. The results of the synoptic measurements of full-disk solar magnetograms carried out on a daily basis

at various observatories, starting at the Mt Wilson Observatory in the late 1950s, have been stored as are at the various sites and also further processed to produce e.g. time series of disk-integrated solar magnetic field measurements. These series include e.g. measurements of the fractional solar surface covered by magnetic fields, as well as the ones of the low-order coefficients of the spherical harmonics that decompose the magnetic field observations as a function of the surface latitude and longitude. The former data have been employed to model e.g. solar irradiance variations. On the other hand, the time series of the multipole coefficients have been used to study e.g. the dominant length scales and symmetries of the observed field, as well as to predict the value of the sunspot numbers at the next solar maximum.
Since late 1960s Ca II K line profiles of the Sun were also obtained both integrated over the solar disk and at given latitudinal bands at e.g. the National Solar Observatory and at the Kodaikanal Observatory, by using high-resolution spectrographs. For the subsequent decades, these K-line monitoring programs have produced almost daily measurements of several parameters characterizing the Ca II K-line measurements. The daily observations of the disk integrated Ca II K emission at the NSO Kitt Peak have been obtained with the Integrated Sunlight Spectrometer (ISS) of the SOLIS telescope since 2006. The ISS monitors the solar emission at nine different wavelength bands regularly.

A recent analysis of the NSO CaII K data indicates that the temporal variation of the measured line parameters consists of five components, including the solar cycle eleven year period, a quasi-periodic variation with 100 day period, a broad band stochastic process, a rotational modulation, and random observational errors. Besides, It has been reported a weak dependency of intensity in the Ca II K line core measured in the quiet chromosphere with the phase of the solar cycle. This dependency has been attributed to the signature of changes in thermal properties of basal chromosphere with the solar cycle.

3. OBSERVATIONAL REQUIREMENTS

The SPRING observables can be grouped into three categories as: (i) measures of solar intensity, I(x,y), (ii) spectra, I(x,y,λ), and (ii) spectropolarimetry, I(x,y,λ,S), where S is the Stokes parameter for polarization analysis of light. Further, these measurements span a wavelength regions from 400-1500 nm, field-of-view (FOV) of full-disk (~2000”), and a temporal cadence ranging from ~30 seconds to tens of minutes.

3.1 Choice of angular resolution and camera detectors:

Initial discussions about the observational requirements for SPRING during Workshops organized at Titisee, Freiburg, Boulder, USA and Slovakia, stressed on

aiming for 1 arc-sec resolution (0.5 arcsec/pix) in all data sets acquired. However, it was noted that aiming for sub-arcsec resolution over full-disk FOV is not feasible due to (i) detector requirements, (ii) data transfer rates, and (ii) seeing limited nature of observations.

For example, aiming for 0.5 arc-sec resolution (0.25"/pixel), twice that of the Helioseismic and Magnetic Imager (HMI) instrument onboard the Solar Dynamic Observatory, would require 8k x8k (64 Mpix) cameras. Most of the cameras available in the market at present reach at most 12 Mpix (4k x 3k), at readout rates ~10-20 fps. Further, the pixel size in these sensors is quite small, ~3 to 4 microns. Such small pixels have very low full well capacity, typically ~10,000 electrons.

Further, the angular resolution for SPRING observations is expected to be limited by the atmospheric seeing because the conventional adaptive optics (AO) works on limited FOV (few tens of arcsec). Multi-conjugate adaptive optics (MCAO) can correct larger FOV than conventional AO, however, the technology is still in its infancy and corrections over full-disk FOV are impractical. However, a tip-tilt image stabilization system would improve quality of observables by correcting global image wandering due to tracking or seeing induced (low order) errors.

As a practical solution, an angular resolution of 1 arc-sec (0.5 arcsec/pixel), which would require 4k x 4k detectors, is sought. Such detectors are not easily available, however. For example, 4kx4k CCD used in SDO/HMI was custom built and achieves frame rates of 2 frames per second, which is too slow for ground based observations. Advances in scientific CMOS sensors are progressing rapidly and are slowly becoming mainstream sensors for scientific applications. Andor technologies and PCO GmbH are leading the development of scientific CMOS cameras, with 4kx3k configurations already available. The 4kx4k cameras are on the horizon and are planned for the DKIST project as well. Here in this study we will assume that the cameras are 4kx4k for magnetic and velocity field measurements and 8kx8k for a high-resolution context imager.

3.2 List of Observables

Key scientific areas addressed by synoptic facility, SPRING, are:

1. Synoptic magnetic fields (Solar Magnetic Cycle, activity complexes)
2. Synoptic velocity fields (Solar Internal Flows, global and local seismology)
3. Transient events (Space Weather, flares, active region evolution)
4. Solar awareness (Sun Climate, High resolution context images)

The Table 2.1 below lists the various observables as demanded by the SPRING science goals (See science requirement document). The science goals are grouped into broad categories (column 2). In column 3 a justification is given for the science goal. In column 4, we list the required observable quantities and in column 5 we give details of observing parameters. We aim to obtain the observables 1-3 in the Table 3.1 with spatial sampling of 0.5 arc-sec per pixel (1 arc-sec resolution), while for high-resolution context imager (observable 5) we aim to obtain the filtergrams at a spatial scale of 0.25 arc-sec per pixel (0.5 arc-sec resolution). Finally, the disk integrated irradiance measurements will be unresolved spatially.

Regarding helioseismology higher spatial resolution full-disk observations help to achieve higher angular degree l which allows seismic probing of the shallow layers. With 0.5 arc-sec per pixel sampling we aim to achieve same angular degree, l, resolution as obtained by SDO/HMI.

The spectral resolution required to record the observables is typically a fraction of the width of solar spectral lines. The goal for SPRING is to have spectral resolution corresponding to FWHM of about ~80mÅ to sample typical solar photospheric spectral lines adequately.

Finally, the temporal resolution is dictated by the science goal, for e.g. for synoptic studies of solar magnetic fields we need to obtain at least one observation per day. For monitoring active region evolution, we need magnetograms every 5 to 10 minutes. Further, helioseismology measurements require continuous time series of observations for long periods to attain high temporal frequency resolution, and each single measurement must be made in less than or equal to a minute for photosphere and less than or equal to 30 seconds for chromosphere.

The requirements for context imager and solar irradiance monitor are different from the above-mentioned requirements. The irradiance measurements are required at a cadence of few per day, with high spectral resolution and with many spectral lines for maintaining consistency with archival data. While for context imager the cadence of observations will be in different in two modes (i) one per minute per wavelength during normal operation, and (ii) at higher cadence during coordinated campaigns with large aperture telescopes.

Table 3.1: List of observables and the detailed observing parameters as required by different science goals.

S. No	Science Goal	Justification	Observables Req.	Observing parameters
1.	**Synoptic Magnetic Fields:**Long-term monitoring of solar magnetic fields	Solar magnetic cycle, relation with internal flows, solar dynamo	Vector Magnetometry of the full solar disk in multiple sensitive solar spectral lines	FOV: Fulldisk Spatial Res: 1arcsec Spectral Res: 100mA Temporal Res: Few per day Spectral Lines: Fe I 6173, Fe I 6302, Fe I 5250, Ca II 8542, He I 10830, Fe I 1.5 micron
2.	**AR evolution and Transient Events:** Solar Flares, flux emergence and cancellation, Helicity flux, free energy evolution in Active Regions	Understanding magnetic origin of solar flares, flare precursors, driving coronal MHD simulations for space weather predictions, estimate of magnetic free energy and helicity.	High cadence vector magnetic fields of the full solar disk in multiple spectral lines	FOV: Fulldisk Spatial Res: 1 arcsec Spectral Res: 100 mA Temporal Res: one per 10 minute Spectral Lines: Fe I 6173, Fe I 6302, Fe I 5250, Ca I 8542, He I 10830, Fe I 1.5 micron
3.	**Helioseismolog**	Internal flow structure	Velocity maps of	FoV: Full disk + prominences

	y:Solar internal flows and waves in solar atmosphere	and its variation with solar cycle, impact on dynamo action, properties of acoustic and magnetoacoustic waves in solar atmosphere, subsurface structure of active regions, meridional flows	the full solar disk in multiple spectral lines	Spatial Res: 1 arcsec Spectral Res: 100 mA Temporal Res: One velocity map per line per 30 seconds Spectral lines: See Table 1.2 below**
4.	**Solar Awareness:** Total and Spectral solar irradiance (TSI, SSI)	Monitor Sun-as-a-star spectral properties, magnetic activity and its signatures on radiative output.	Spectrophotometry of unresolved solar radiation.	FOV: Unresolved Solar light Spatial Res: Unresolved Spectral Res: 20 mA Temporal Res: One per day
5.	**Context Imager** for Upcoming Large Aperture Telescopes.	Provide complementary information over larger FOV to support small FOV observations by future large aperture telescopes	High resolution imaging in different broad and narrow spectral bands, including continuum images	FOV: Full disk Spatial Resolution: 0.5 arcsec (after post processing) Spectral Resolution: broad band (0.25 to few Angstroms) Temporal Resolution: Few per minute or as demanded by coordinating observer.

3.3 Choice of spectral Lines: SNR and sensitivity requirements

3.3.1 Choice of spectral lines for helioseismology

The selection of spectral lines to be used in the helioseismic analysis of waves in the solar atmosphere should be such that their formation height samples the distinct heights in the solar atmosphere. Based on the analysis of formation height using line contribution functions and response functions a set of lines was chosen for the multiline helioseismic study carried out by Staiger (2008) and Wisnieweska (2016). In the Table 3.2 below we list these lines and their formation height estimates, when available. These are graphically depicted in Fig 3.1., where the range of formation height spans many different layers from the deep photosphere to the chromosphere. We also computed the intensity and velocity response function of some of these photospheric lines using the LTE radiative transfer code SIR (Ruiz Cobo & del Toro Iniesta, 1992). These are shown in Figure 3.2, upper panel: temperature response and lower panel velocity response. It can be seen that the velocity response of narrow and deep photospheric lines is stronger than shallower lines such as Fe 1 1.56-micron line. For all lines the response peaks near the wings of the lines as expected. Also, the velocity and temperature response in the line core shows the range of heights in the solar atmosphere where the lines are sensitive to perturbations to these quantities.

Estimation of velocity sensitivity for spectral lines:

We also compute the velocity sensitivity, limited by the photon noise alone, according to the method discussed by Bouchy et al. (2001), which is given by

$$\delta V_{RMS} = \frac{c}{Q\sqrt{N_{e^-}}} \quad (3.1)$$

Where, Ne^-, is the total number of photoelectrons collected by the detector in all wavelength samples across the line, c is the velocity of light and Q is the quality factor of the spectral line. The Q-factor depends upon the slope of the line wings and is given by

$$Q = \frac{\sqrt{\sum W(i)}}{\sqrt{\sum A_0(i)}}.$$

Where, $A_0(i)$ is the observed intensity of the spectral line along the pixels, i, in the spectral direction and W(i) are the weights, given by

$$W(i) = \frac{\lambda^2(i)\,(\partial A_0(i)/\partial\lambda(i))^2}{A_0(i) + \sigma_D^2}.$$

The quantity σ_D is the detector noise, such as flat, dark and bias noise. It should be noted that the velocity sensitivity of a spectral line mainly depends upon the shape factor Q. Even though Doppler sensitivity increases with longer wavelength the shape factor is most dominating factor.

To make an estimate of the velocity sensitivity in typical setup we assume here that the measurements of spectra are carried out by a tunable filter of band pass FWHM=80mA and that detector readout noise is negligible. The left column of Table 3.2 lists the various spectral lines that are being considered for helioseismic measurements. For some of these lines the formation height estimates are available from Wisneweska et al 2016. In column five of the Table we compute the SNR per pixel required to achieve the velocity sensitivity of 10 m/s when the line is sampled uniformly across at least 40 wavelength points. The column six lists the Q-factor (or shape factor) of the line which determines the sensitivity of the line to measure Doppler velocity. It can be noticed that the chromospheric lines typically have low Q-factor due to their broad shapes while photospheric lines are narrow and hence have higher Q-factor. This is also reflected in SNR requirements, which are higher for chromospheric lines.

Table 3.2 below lists the spectral lines selected for Doppler measurements. Lines in red color are chromospheric, rest are photospheric. The typical error in velocity measurements based on typical filter based measurement setup.

S. No.	Spectral line (Å)	Element	Formation Height (km)	SNR required	Q-factor of the line
1	3933	Ca II K		1400	3400

2	3968	Ca II H		1000	4600
3	5173	Mg I b1	595±5	450	10300
4	5250	Fe I		250	18900
5	5434	Fe I	556±25	350	13800
6	5576	Fe I	310±15	350	13300
7	5890	Na I D2	927±35	450	11000
8	5896	Na I D1		550	8500
9	6173	Fe I	276±26	320	14700
10	6301	Fe I	337±23	350	13300
11	6302	Fe I		320	15500
12	6563	H I α	1200-1700	600	8100
13	6768	Ni I		300	16000
14	7090	Fe I	284±32	420	10800
15	8542 (4Å window)	Ca II		800	6000
16	10830	He I		1400	600
17	15648	Fe I		500	9500

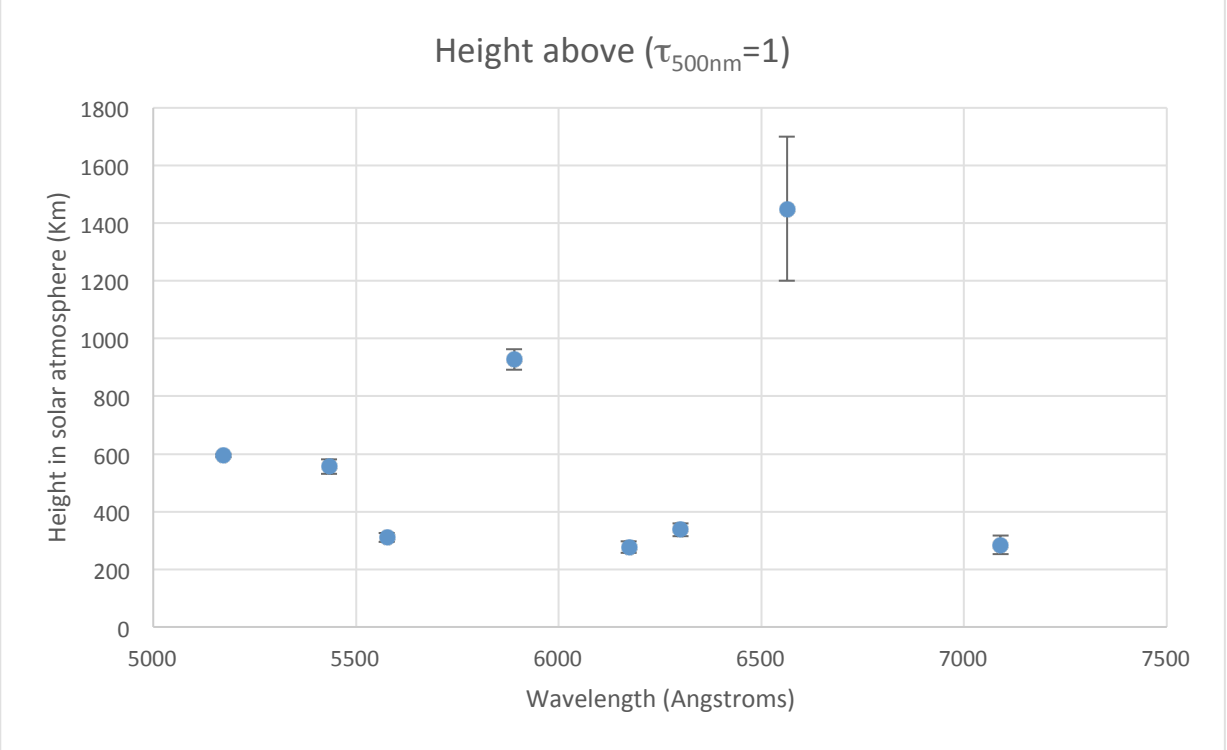

Figure 3.1. The formation height of solar spectral lines is graphically represented here. Left and right panels are the same with only the x-axis being compressed in the right panel to show the range spanned by the lines.

The goal for SPRING Doppler measurements is to achieve a velocity sensitivity of about 10 m/s, like GONG and HMI. Calculations show that with single exposure (considering a pixel with typical full well limit of 40 ke) measurement will not be enough to achieve 10m/s sensitivity. We would need to accumulate several frames per wavelength step to reach the desired value of 10m/s. The number of frames that need to be accumulated will be computed in the later sections. Here we mention that the number of frames is typically ~10 for photospheric lines and ~50 for chromospheric lines.

It should be noted that in practice the velocity sensitivity will be limited not by the photon noise but by the other fluctuations in the intensity measurements mainly due to image motion due to atmospheric seeing while the spectral measurements are being made. Since these factors are beyond our control in the instrument design we stick to the numbers from photon noise considerations alone. The use of auxiliary data such as white light images acquired with the spectral data can be used to correct for seeing errors.

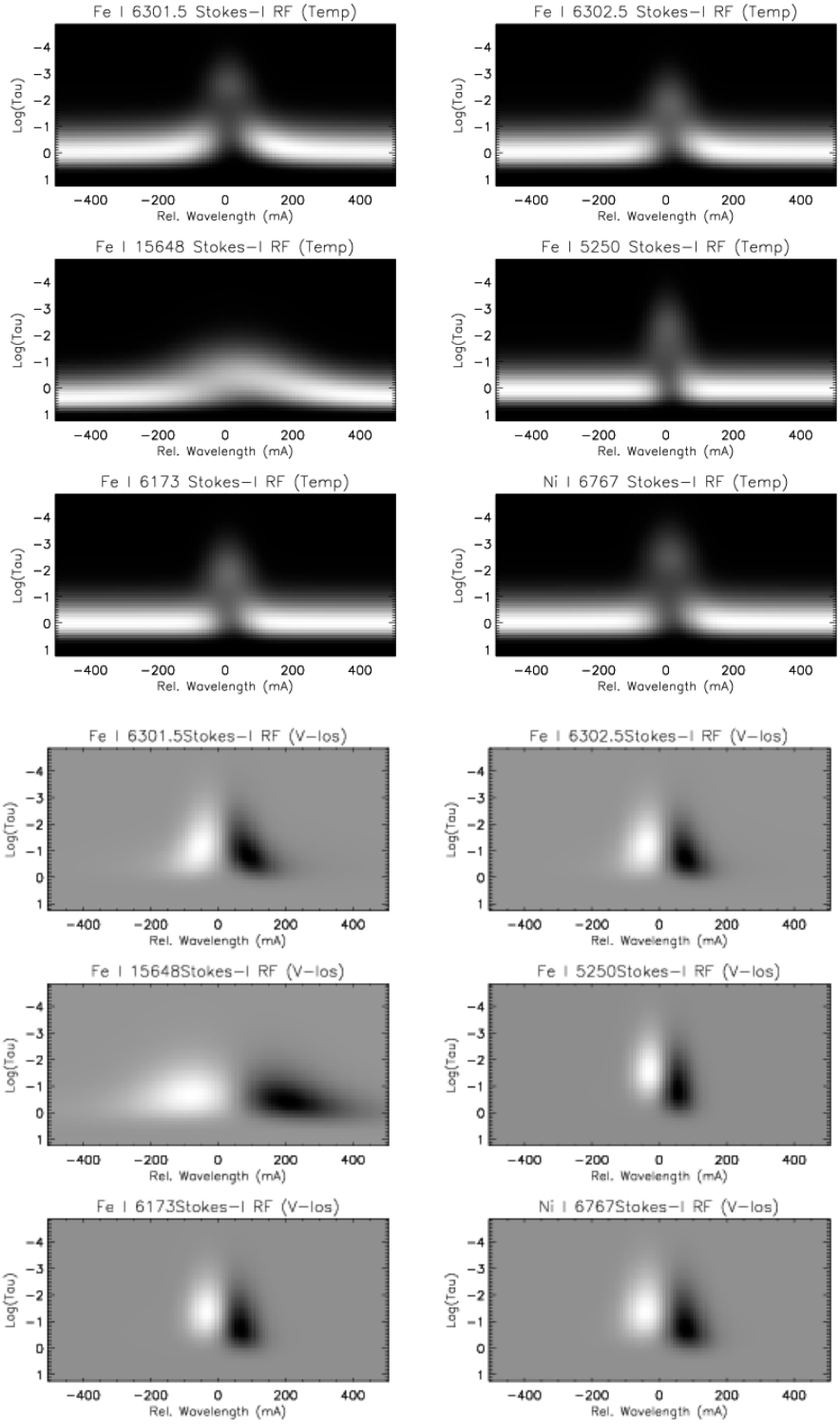
Fe I 6301.5 Stokes−I RF (Temp)
Fe I 6302.5 Stokes−I RF (Temp)
Fe I 15648 Stokes−I RF (Temp)
Fe I 5250 Stokes−I RF (Temp)
Fe I 6173 Stokes−I RF (Temp)
Ni I 6767 Stokes−I RF (Temp)
Fe I 6301.5Stokes−I RF (V−los)
Fe I 6302.5Stokes−I RF (V−los)
Fe I 15648Stokes−I RF (V−los)
Fe I 5250Stokes−I RF (V−los)
Fe I 6173Stokes−I RF (V−los)
Ni I 6767Stokes−I RF (V−los)
Log(Tau)
Rel. Wavelength (mA)

Figure 3.2: The intensity and line-of-sight velocity response functions computed from SIR radiative transfer computation code for various photospheric lines are shown (see title of each panel for details).

3.2.2 Choice of Spectral Lines for Magnetic Field measurements

The magnetic field sensitivity of lines used with Zeeman diagnostics depends on Lande g-factor and wavelength. The spectral lines for magnetic field measurements with SPRING needs to be chosen to sample different heights in the solar atmosphere. Again, the selection of lines should be done to have overlap with other instruments and lines used in existing synoptic records such as Kitt Peak records. Such lines are 630.1 nm with SOLIS/VSM at NSO, Fe 5250 at Wilcox Solar Observatory, He I 10830 and Fe 1 1564.8 nm at Mitaka, NAOJ.

For solar spectral lines with identical magnetic splitting, the Zeeman sensitivity of lines increases with increasing wavelength. To determine a spectral line's sensitivity in measuring the solar magnetic field one can take the ratio of the magnetic Zeeman splitting, proportional to $\lambda^2 g_{eff,}$ and the Doppler line broadening, proportional to wavelength λ. This ratio then varies as λg_{eff}.

Some of the lines listed in Table 3.2 for velocity measurements may have poor sensitivity for magnetic field measurements. To rule out such lines we compute the Zeeman splitting for the lines listed in Table 3.2 for a field strength of 10 G in velocity units (i.e., $v_H=\Delta\lambda_H/\lambda c$, where $\Delta\lambda_H$ is the Zeeman splitting corresponding to 10 G and c is the velocity of light) and call it magnetic sensitivity and then compare it with the velocity sensitivity (Q-factor, section 3.2.1). The scatter of the v and B sensitivity is plotted in Fig 3.3 below. The green dashed line selects a region where the lines have simultaneously better magnetic and velocity sensitivity. We select these lines for further study.

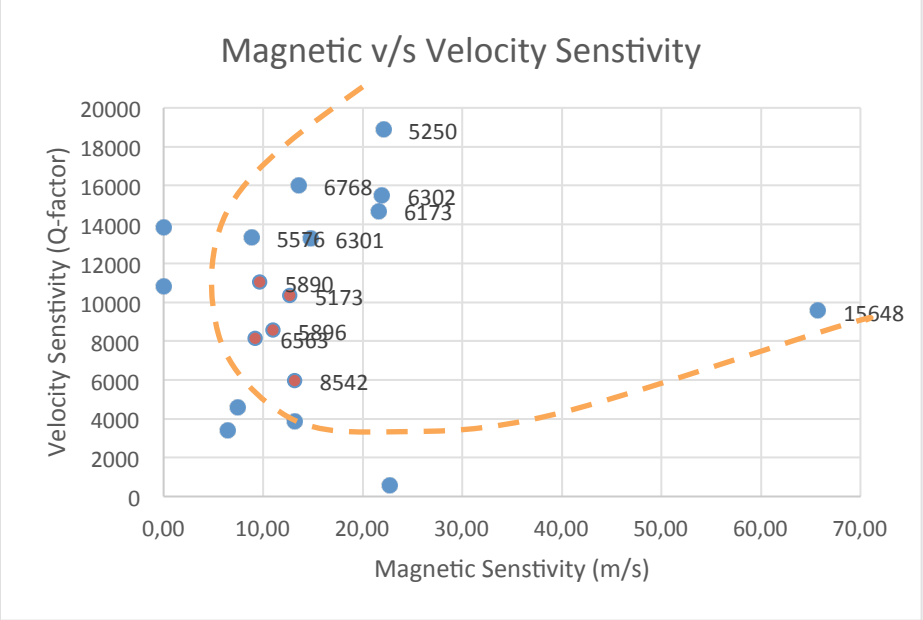

Figure 3.3 Plot of Zeeman sensitivity v/s Doppler sensitivity of spectral lines in Table 3.2

These selected lines are listed in Table 3.3 below. Chromospheric lines are marked in red color. The Lande g-factor is listed in column 2 for these spectral lines and magnetic sensitivity for 10 G is in column 3 in velocity units. We note that for most of these selected spectral lines the Zeeman splitting is equal or higher than the velocity sensitivity requirement of 10 m/s in previous section 3.2.1. Thus, keeping SNR requirements of the measurements the same as in Table 3.2, would allow for a longitudinal magnetic field sensitivity of ~20 G in most of these spectral lines using the center-of-gravity (COG) method.

Table 2.3 Table of spectral lines with respective Zeeman sensitivities

Line	Lande g-factor	Magnetic Sens. (m/s)
5250	3	22
5576	1.13	9
6173	2.5	22
6301	1.67	15
6302	2.49	22
6768	1.43	14
15648	3	66
5173	1.75	13
5890	1,17	910
5896	1.33	11
6563	1	10

8542	1.1	13

The sensitivity to transverse field will be much poorer than 20 G, since the transverse Zeeman effect is proportional to the square root of Stokes-Q, U (linear polarization) signal. To find an estimate of the SNR requirement for transverse fields in different lines we synthesize Stokes profiles using the LTE radiative transfer code (SIR; Ruiz cobo & del Toro Iniesta, 1992) under the HSRA (Harvard Smithsonian Reference Atmosphere) model atmosphere assumption. These profiles are shown in Fig 3.4 and 3.5 for a model field strength of 100 and 200 G, respectively. The field azimuth and inclination angle are chosen as 100 degree each. Only photospheric lines are synthesized.

These profiles show that the typical SNR requirement for 20 G longitudinal fields (Stokes-V) is about 300-600, while for transverse fields (Stokes Q, U) a SNR of 1000 will lead to a sensitivity of 100-200 G, depending on the lines.

For chromospheric fields the signals are even weaker. As an example, we synthesize Stokes profiles for Ca II 854.2 nm spectral line in a HSRA model atmosphere with uniform magnetic field of Bx, By, Bz=100 G (a total field strength=173 G), using NICOLE, a NLTE radiative transfer code (Socas-Navarro et al. 2015). Figure 3.6 shows that the signal level in Stokes Q, U require SNR between 1000-2000, while in Stokes-V require SNR of few 100s. However, these are conservative estimates as HSRA is a quiet sun model atmosphere, in sunspots for example the intensity is much lower than quiet sun and there will be scattered light as well, therefore SNR in ~2000 or greater will be required for reliable transverse field measurements.

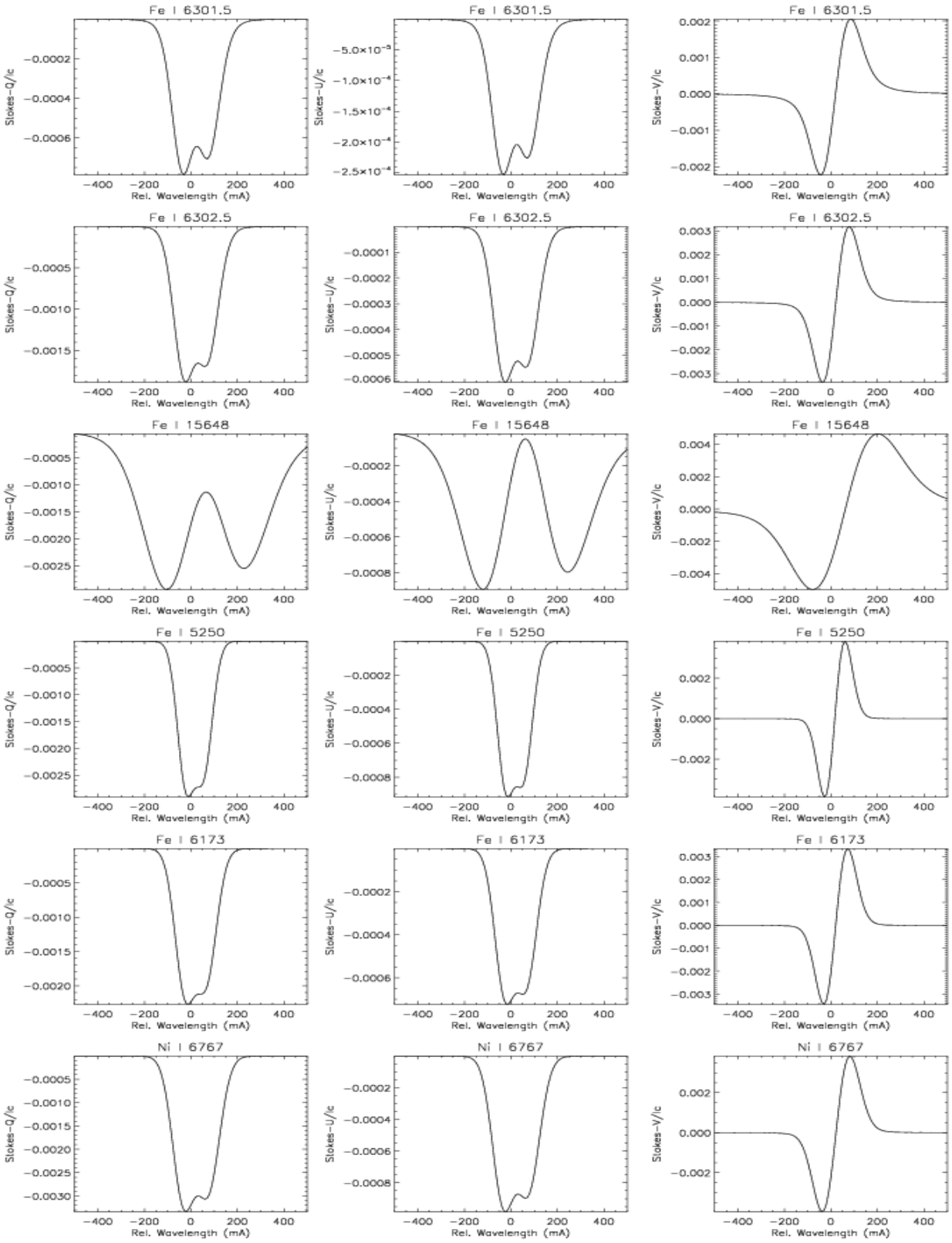
Fe I 6301.5
Stokes-Q/Ic
Stokes-U/Ic
Stokes-V/Ic
Fe I 6302.5
Fe I 15648
Fe I 5250
Fe I 6173
Ni I 6767
Rel. Wavelength (mA)

Figure 3.4: Stokes, Q, U and V profiles synthesized using SIR code for a field strength of 100 Gauss, inclination and azimuth angle of 100 degree each.

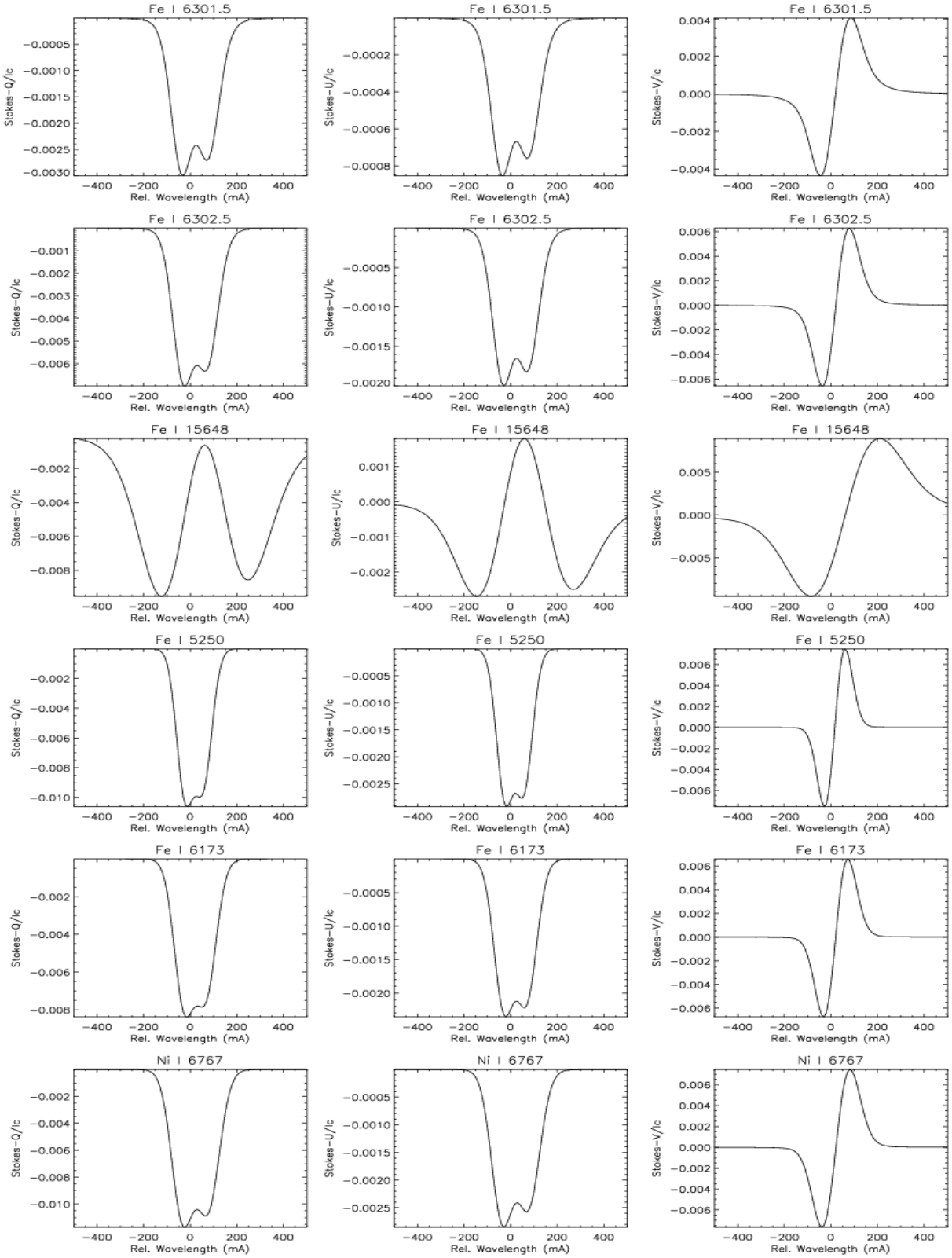
Fe I 6301.5
Stokes-Q/Ic
Stokes-U/Ic
Stokes-V/Ic
Fe I 6302.5
Fe I 15648
Fe I 5250
Fe I 6173
Ni I 6767
Rel. Wavelength (mA)

Figure 3.5: Stokes, Q, U and V profiles synthesized using SIR code for a field strength of 200 Gauss, inclination and azimuth angle of 100 degree each.

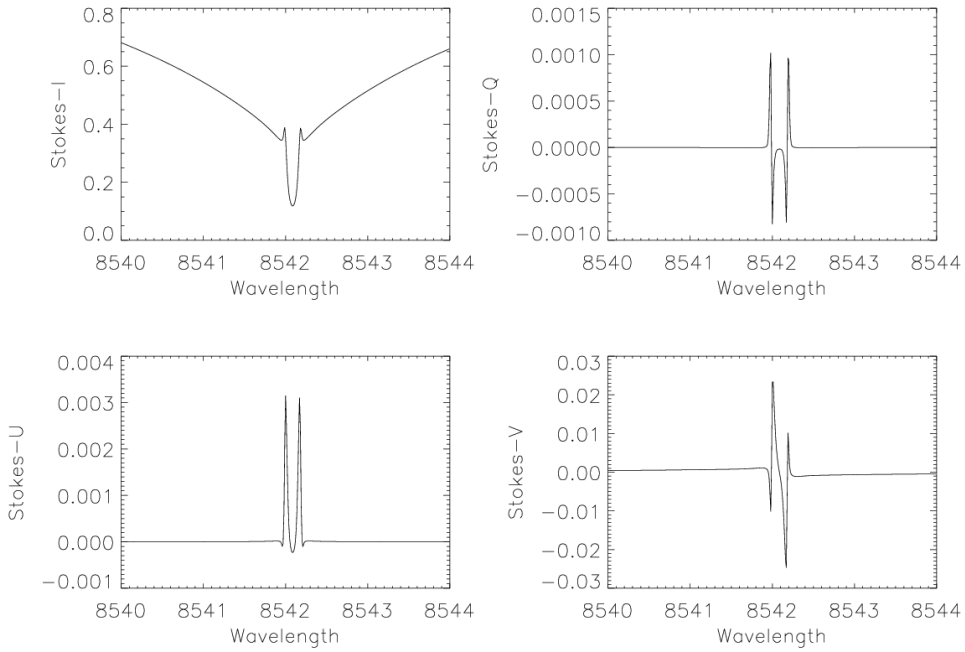

Figure 3.6: Synthetic Stokes profiles for Ca II 854.2 nm, chromospheric spectral line, computed with NICOLE, a NLTE radiative transfer code, in uniform magnetic field Bx,By,Bz=100 G.

As an exception to the previous discussion, we also include the He I 1083 nm spectral line, which is a very valuable line for chromospheric diagnostics. Even though the velocity sensitivity of the line (Q-factor is quite low ~600) the magnetic sensitivity and diagnostic value of the line is very good and so we include this line in our list for magnetic field measurements. Further, the H-alpha line is dropped because its line formation is complex and interpretation of polarization signals is not very clear.

Table 2.4 Spectral lines selected for magnetic field measurements with the SNR requirements to obtain reliable field measurements.

Line	SNR Requirement (B-LOS/ 20G)	SNR Requirement (B-TRANS/ 100G)
5250	300	500
6173	320	500
6301/6302	350	1000/500
6768	300	500
15648	500	500
10830	1400	1500

5173	450	1500
5890	450	1500
5896	550	1500
8542	800	1500

4. TELESCOPE/LIGHTE FEED DESIGN CONCEPT

4.1 Telescope Aperture Size

The aperture size for meeting the requirements of the angular resolution is only 25-35cm, from the short to the long wavelength range of the spectral lines considered. However, the main criterion for the aperture size of the telescope for SPRING comes from SNR considerations, number of spectral lines, and the requirement to observe them in a short time interval of ~30 seconds. The list of lines given in Table 3.2 and 3.4 and the SNR requirements, with a constraint of obtaining the full set of data in less than a minute, suggests that an aperture size of at least 50 cm is a must for typical system transmission and spectral passband of spectrometer. Thus, the telescope for SPRING needs not be diffraction limited, as the Rayleigh resolution of a 50 cm aperture telescope is far superior than the SPRING requirement of 1 arcsec. It is known that the number of photons per diffraction limit is conserved, regardless of the aperture of the telescope, so the large aperture is needed in SPRING to collect more photons to meet the observational requirements.

However, a larger aperture telescope has its own problems. The drawbacks are, (i) an increased cost of the project (cost of telescope goes as D^3), (ii) complexity introduced by heating issues, (iii) large and bulky mechanical mounts, (iv) higher maintenance costs, and (v) issues with acceptance angle of narrow passband filters.

In deciding for the telescope aperture one also must keep in mind about the backend systems. Here we assume that the fulldisk images inherently require very good geometric accuracy, i.e, the distortions should be minimal to co-align images from the same instrument in different spectral bands and times, as well as co-alignment with other space and ground based telescopes. Further, helioseismology requires high degree of geometric accuracy for accurate determination of oscillation modes. Also, given the time constraints on multi-line data (whole set of observations within 30 seconds), it is quite apparent that such observables would need a 2-D filtergraph for snapshot imaging at the cost of scanning in spectral dimension.

In the field of solar astronomy, Fabry-Perot etalons have seen a lot of application. Lyot type filters have also been used but mostly for morphological imaging such as H-alpha imaging of the chromosphere. Due to their limited transmission (3-4 %),

polarized nature (no dual beam polarimetry), smaller apertures (vignetting issues), and slow tuning, these filters have not been used much in high-cadence, multi-line, spectro-polarimetric observations of the fulldisk. So, the Fabry-Perot seem to be the most favorable option for such kind of observations. There are two types of Fabry-Perot etalons (i) air-spaced, generally the cavity is piezo tuned, and parallelism is maintained by servo controllers, and (ii) solid etalon, generally made of an electro-optic crystal such as Lithium Niobate ($LiNbO_3$), parallelism is achieved during fabrication and stays the same, tuning is achieved by changing the refractive index by applying an electric field to the crystal. The LiNbO3 etalons have the advantage that the parallelism is always the same and due to high refractive index of 2.23 the acceptance angle is large compared to air spaced etalon and thus relatively smaller apertures are needed. However, they are fragile, have more absorption than glass and their tuning speed is slower than piezo tuning of air spaced etalons. Unfortunately, the fabrication of LiNbO3 etalons has now stopped as the company that used to make them, CSIRO, Australia, has discontinued their production. While, air spaced piezo tuned etalons are still available. Here we assume that the design of SPRING will involve such etalons and hence keep in mind the impact of this situation on the telescope aperture selection.

4.3.1 Large Aperture Telescope with large aperture filters:

With a large aperture telescope and if a single filtergraph is to be used, such as an air spaced Fabry-Perot filter, then there is a problem of acceptance angle. The aperture of the largest etalons is 15-20 cm, and these are air spaced etalons with thick and heavy plates, mainly designed for operation on a stable optical bench. In an equatorial tracking system, the changing gravity vector causes changing flexure of plates and hence the passband of the filter is non-uniform and introduces systematic drifts. Further disadvantage of using a single etalon with a large telescope is that one needs quite large order sorting interference filters, and the sequential mode of observing in spectral domain is slower, i.e., due to bulkiness of etalon plates the tuning via piezo is slower compared to smaller etalons.

One can try to overcome the speed limitation by parallelizing the process, such as using dichroic beam splitters to split the beam in different spectral bands and observe the lines in parallel. However, here one would need again large aperture etalons (now one per spectral passband) and the flexure issue remains. A schematic of such a system is shown in the Figure 4.1 below. Note the lateral dimensions of the instrument become very large when such light distribution is implemented.

4.1.2 Large aperture telescope with small aperture filters:

Assuming one uses smaller aperture etalons to avoid flexure issues, and tries to implement parallel observing in different spectral domains, then one needs a different

type of light distribution system to feed each. A schematic of such a light distribution system is shown in Fig 4.2. Note that the lateral dimensions are not much here but the equivalent aperture of each lens-let is reduced to ~20-25 cm.

In summary if one wants to observe 10-12 lines, spanning 400-1500 nm, with a single large aperture telescope then one also needs to develop very complex mechanisms for filter wheels and light distribution optics so that the whole system becomes very complex, expensive and chances of failure increase significantly.

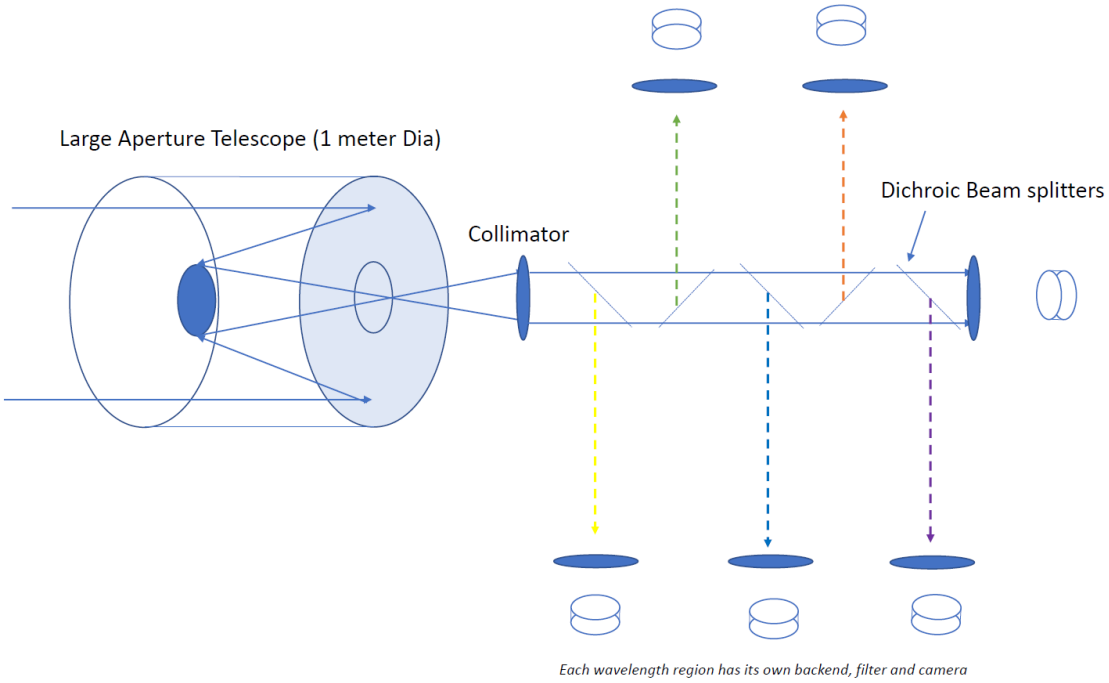

Figure 4.1: Schematic of a large aperture telescope with a light distribution system using dichroic beam splitters.

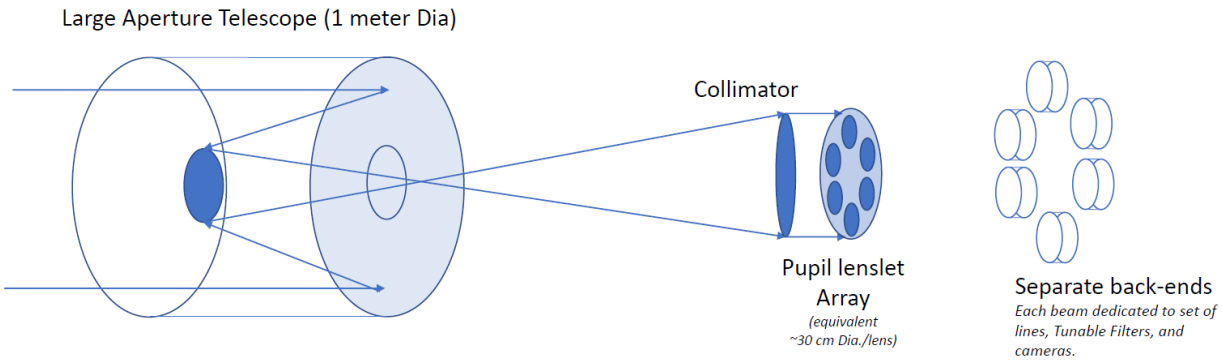

Figure 4.2: Schematic of large aperture telescope with light distribution system using lens-let array.

Further, if there is a problem with the telescope then all the observations suffer. Even with all the complexities it should be noted that the demand for a large aperture comes mainly from the need to observe many spectral lines in a limited amount of time, i.e., more photons and not the angular resolution. If one were to obtain observations in only one spectral line then even a 15-cm aperture refractor can do the job in << 1 minute at 1 arcsec resolution. For example, GONG has an effective aperture of 2.8 cm and still obtains a Dopplergram in a minute.

4.1.3 Multiple Parallel Telescopes with smaller filters:

One of the main design criterions for any long-term synoptic instrument such as SPRING is to have simplicity in design so that impact of component failures on the complete set of observables should be minimal and the costs involved are also small. This keeps failures minimal and repairs are manageable without severe impact on the network duty cycle.

With this approach in mind, we follow the idea that the list of spectral lines should be divided into three broad spectral regions blue-red (300-600nm), red-near-IR (600-900nm), nearIR-IR (900-1600nm), and for each of this spectral region we should then develop a separate, self-contained system, each with its own telescope, back-end optics and detectors. With this approach, we can also optimize each system for that wavelength range such as telescope aperture size, coatings, and detectors. We call these systems, fulldisk imaging telescope (FDT): FDIS-B (Blue), FDIS-R (Red), and FDIS-IR (Infrared).

FDIS-B: 3933, 3968, 5173, 5250, 5434 Angstroms
FDIS-R=5890, 5896, 6173, 6302, 6563, 6768 Angstroms
FDIS-IR=8542, 10830, 15648 Angstroms

There are many benefits of grouping the sub-systems by wavelength regions.

(i) SPRING is a community effort between many nations. Each subsystem then can be led by different partner institutes and integrated later to a common platform. This reduces costs, development time and later on running costs.
(ii) Failure of one system does not affect the data-stream from other systems. Only few wavelength channels suffer.
(iii) Three small telescopes cost less than one large telescope.
(iv) With three separate channels the cadence criterion for helioseismology to obtain Dopplergrams in several lines under 30 seconds is easily achieved.

As an example, we calculate the velocity sensitivity, using Eq (3.1), achieved by a typical Fabry-Perot based filtergraph instrument of nominal passband of 80 mA, with

typical system + atmospheric transmission of 3%, detector QE of 60%, exposure time of 10 milliseconds, 30 wavelength steps along the spectral line and accumulation of about 10 frames (assuming full-well ~40 ke, read speed of 50 fps) for various telescope aperture sizes, as shown in Fig 4.1. For all photospheric lines a sensitivity of 10 m/s is easily achieved by a modest aperture size of 25 cm or above. We also add 1 second of dead time for switching interference filters between observations. Even with smaller aperture of 10 cm this sensitivity can be achieved by accumulating a significantly larger number of frames, keeping the cycle time still under 30 seconds, thanks to parallel channels for different spectral regions. Regarding chromospheric lines, the velocity signals are typically much larger than the photospheric ones due to low plasma densities and hence a sensitivity of 10 m/s is not critical, even then, except for He I 1083nm, all chromospheric lines in our list can be measured with a sensitivity of < 50 m/s.

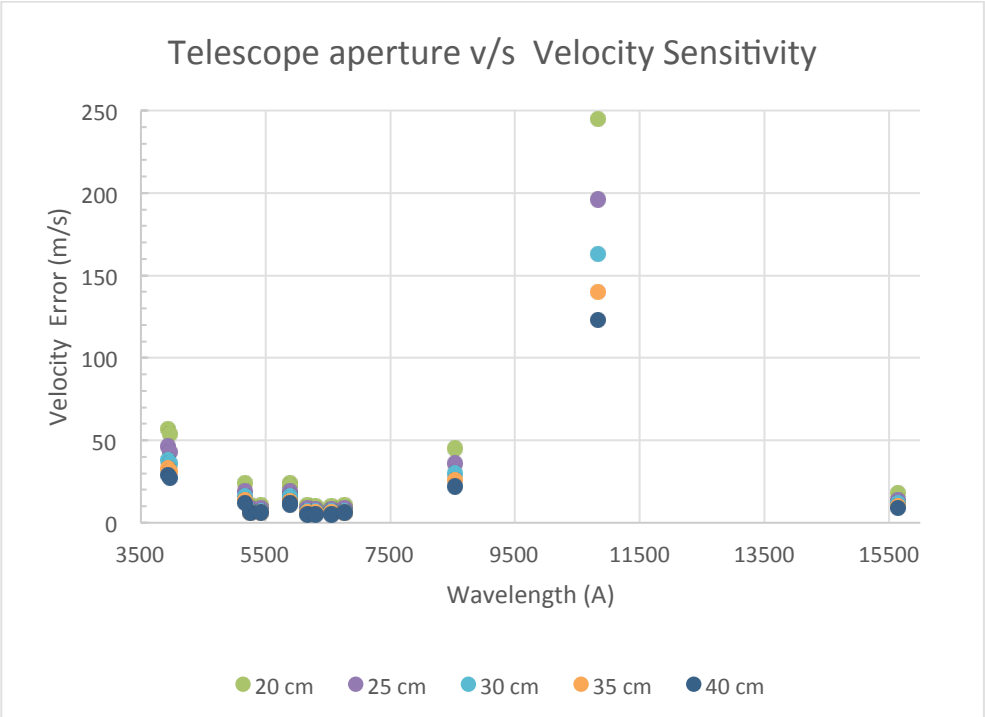

Figure 3.1: Velocity sensitivity as a function of wavelength (spectral lines), for different telescope aperture sizes is shown. A constraint of obtaining data in all wavelengths in less than 30 seconds was imposed.

A similar exercise for magnetic sensitivity shows that an aperture of 20 cm achieves the required SNR in 30 seconds for the three channels FDIS-B, FDIS-R and FDIS-IR. In Figure 3.2 we show the various values of the expected signal and time required to achieve observations of required SNR. These values are calculated for a telescope without obstruction such as the refractor. The SNR of > 1000 is obtained for each

spectral line. To keep room for the addition of more spectral lines in the future, it would be better to design the aperture size slightly larger than the optimal one computed here. Thus, we aim for a 25 cm aperture telescope for SPRING in all three channels FDIS-B, FDIS-R, and FDIS-IR.

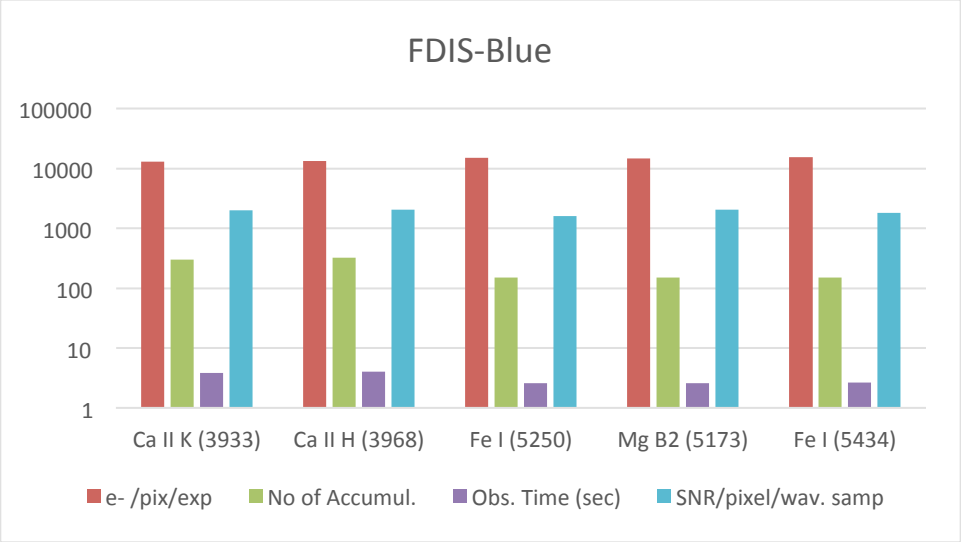

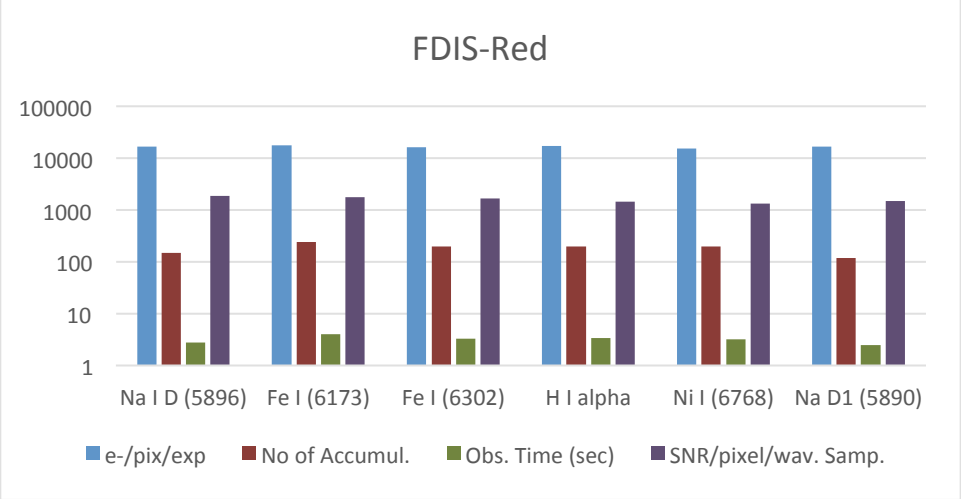

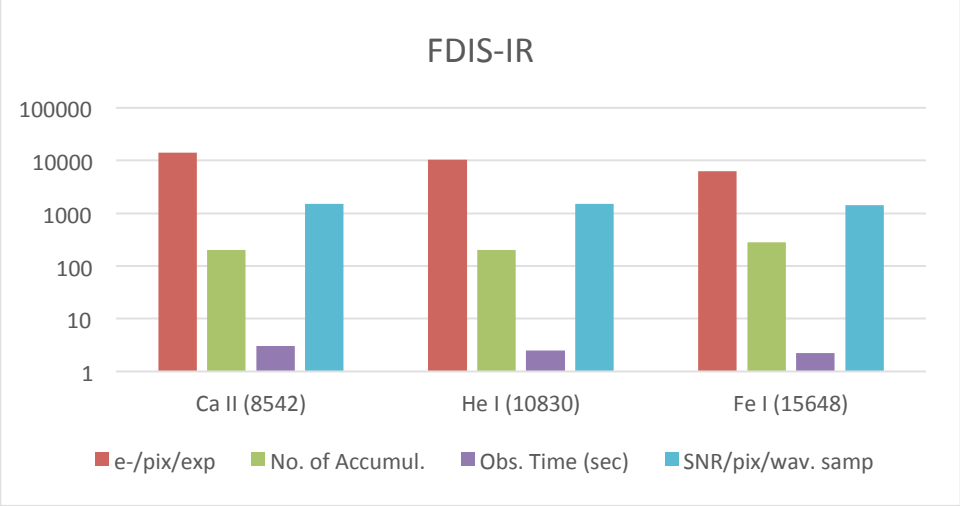

Fig 3.2: Computed values of electrons/pixel/exposure, no. of accumulations needed to achieve the required SNR, total observed time in seconds, and SNR per pixel per wavelength sample, for a telescope of 20 cm aperture for the three channels FDIS-Blue, FDIS-Red and FDIS-IR.

4.2 Telescope Type

We begin by listing existing full disk synoptic telescopes in the world below in Table 4.1. Most of the telescopes are based on a refractor design with apertures ranging from 10-20 cm in size, except for SOLIS/VSM, which is the only reflective telescope and has the largest 50 cm aperture. It is also noted that the instruments designed for magnetometry are all equatorially mounted except for GONG, for which polarimetry was added later. The details of these instruments are given in Table 4.1 and in captions for Fig 4.3 - 4.6.

Table 4.1: List of operational Full disk solar telescopes with polarimetry, ordered by decreasing aperture

S No	Telescope	Light-feed Type	Aperture	Polariz. free
1.	SOLIS/VSM at NSO, Tucson, USA	Reflector, equatorially mounted	Fulldisk optical telescope, modified Ritchey-Chritien design, 50 cm aperture	Yes
2.	Solar Magnetic Activity research Telescope (SMART), Hida Obsrvatory, Kyoto, Japan	Refractors, equatorially mounted	Fulldisk vector magnetograph 20 cm	Yes
3.	Solar Flare Telescope (SFT),	Refractors, equatorially	Fulldisk infrared spectropolarimete,r 15 cm	Yes

	Mitaka, NOAJ, Japan	mounted		
4.	Solar Magnetic Activity Telescope (SMAT), HSOS, China	Reflector, equatorially mounted	Fulldisk Vector Magnetography, 10 cm	Yes
5.	GONG, Worldwide network, NSO	Turret + refractor	Fulldisk longitudinal magnetograms; optimized for Ni 6768 line; 2.8 cm effective aperture	No

Figure 4.3 GONG turret system connected to shipping container which houses the instrument.

Figure 4.4: Left panel shows SOLIS, a 50 cm aperture full-disk telescope mounted on an equatorial mount. Righ panel shows the retractable dome that covers SOLIS.

Figure 4.5: Solar Magnetic Activity Research Telescope (SMART), Hida Observatory, Kyoto, Japan. It is a combination of four parallel telescopes, two performing full-disk H-alpha imaging and vector magnetography in the Fe I 630.2nm spectral line, and two telescopes performing high resolution (limited FOV) observations in 630.2 (vector magnetography) and H-alpha (core and wing emission).

Figure 4.6: The Solar Flare Telescope at Mitaka, NAOJ, Japan, is a combination of four parallel full disk telescopes performing (i) H-alpha and white-light imaging, (ii) infrared spectropolarimetry, (ii) G-band imager, and (iv) white light imager.

Here we discuss some aspects of these different types of light feed/telescopes.

Option 1: Turret type: The GONG instrument consists of two mirrors tracking the Sun in elevation and cross- elevation axes that feed light horizontally into a cargo container housing the rest of the equipment. The optical system is sealed by a filtered window and has an effective aperture of 2.8 cm.

For SPRING one can decide to go for a similar design, however, GONG was not designed for polarimetry and its image rotation will be an additional concern in the mechanical design of the camera assembly. A turret for 20 cm aperture refractor can be designed however, a normal shipping container as GONG may not have enough room for housing the suite of instruments that SPRING will contain. For polarimetry, there will be crosstalk between Stokes parameters, which will be time varying and will need proper modelling and frequent calibration.

In summary, such a system is feasible, however, it needs a much larger container design and light distribution system to feed various channels. Polarimetry will need frequent multi-wavelength calibrations and image rotation will have to be addressed.

Option 2: Refractor (achromatic doublet): Achromatic doublets up to 15 cm diameter are commercially available. However, for a 25 cm aperture one will have to design and ask for a custom fabrication. High quality achromatic doublets can be easily designed, furthermore, due to the specific wavelength range of FDIS-B, FDIS-R and FDIS-IR these need not be optimized over a very large wavelength range and hence the designs would be easier. Generally achromatic doublets are composed of two individual lenses made from glasses with different amounts of dispersion. Typically, one element is a negative (concave) element made from flint glass such as F2, which has relatively high dispersion, and the other is a positive (convex) element made of crown glass such as BK7, which has lower dispersion. The lens elements are mounted next to each other, often cemented together, and shaped so that the chromatic aberration of one is counterbalanced by each other.

A disadvantage of using refractors in a solar telescope is that the length of the system becomes too long when long focal lengths are involved, such as in the case of solar astronomy. Another disadvantage is that the active tip-tilt correction can be only performed after the prime focus and requires folding of the beam through an active mirror, where the pupil is imaged onto the active mirror.

Option 3: Reflective Folded Optics Design: Reflective designs have the advantage of a lower system length for the same effective focal length and hence the system can be made compact. Further, having an active secondary mirror helps in providing active correction for image motion correction and defocus.

As mentioned above the only existing synoptic facility that uses a reflective design is the SOLIS/VSM instrument. SOLIS/VSM is equipped with a 50 cm aperture

telescope with a quasi Ritchey-Chretien design with a two-field lens corrector to provide adequate image quality over the whole FOV, minimal geometric distortion, equal image size for all wavelengths, and a nearly telecentric beam to minimize FOV effects in the polarization modulators.

This design was chosen over a Schmidt-Cassegrain and Gregorian design for superior optical performance. The primary mirror is made of ULE to minimize temperature-induced aberrations. It is coated with overcoated silver. The secondary mirror is made of single crystal silicon. Regular glass-based mirrors with their low thermal conductivity would lead to large thermal gradients within the mirror substrate and therefore to intolerable optical aberrations. A fan system is designed to circulate the helium in such a way that the secondary mirror is cooled. Tests of the temperature gradients within the secondary mirror and temperature variations do not show significant aberrations.

The secondary mirror also acts as fast tip-tilt corrector to remove image motion due to seeing and telescope shake and has a focusing mechanism to maintain best focus. Helium filling provides about the same amount of convective cooling as air, while leading to about 10 times less seeing for a given temperature difference.

SPRING Front-end Design:

Considering all the parameters such as, the compactness, polarization free symmetric optical design, active tip-tilt corrector built into the system, we propose that a design like the proven SOLIS/VSM telescope be adopted for the SPRING FDIS instruments. Here we present a Ritchey Chretien type design which is basically a scaled down version of the SOLIS VSM design. The entrance aperture was reduced to 26 cm while the focal length is kept 333 cm, which gives an f/D ratio of 13. The design was optimized for the wavelengths ranging from 0.5 to 1.56 micron. The parameters of the SPRING FDIS are listed in Table 4.2. The optical layout of the telescope is given in Fig. 4.7. A field corrector lens is used to minimizing aberrations over the field-of-view. The corresponding spot diagram is shown in Fig 4.8 for different field angles and wavelengths. The performance is diffraction limited in all design wavelengths. Further, the image at the prime focus is nearly telecentric, so the angles through the following optics, will be homogenous. The telecentricity is depicted in Fig. 4.9, with lower, upper and chief-ray incidence angle as a function of image height.

The secondary mirror diameter is about 30% of the primary diameter. Back focal distance from the secondary is 35 cm, which provides ample space for accommodating calibration filters as well as tapping part of the beam for providing feedback to the secondary tip-tilt mirror to correct for defocus, seeing and tracking related image motion. The smaller aperture of the FDIS telescope is more suitable for moderate seeing conditions as typical r0 (Freid's parameter) is in the range of 5-10 cm on average, and the aperture is only 3-5 times larger than this value. Larger

apertures in general induce more image blur than smaller apertures for a given seeing condition.

Table 4.2: Telescope parameters for SPRING FDIS front-end

Parameter	**Value**
Entrance Pupil Diameter	254 mm
Secondary Diameter	80 mm (32% of primary)
Maximum radial field	0.28 degrees
Effective focal length	3327 mm
Image space f #	13.09
Back focal length	34.23
Image Diameter	32.5 mm
Wavelengths optimized	0.5,0.63, 0.85,1.08,1.56 μm
Image plane	Telecentric

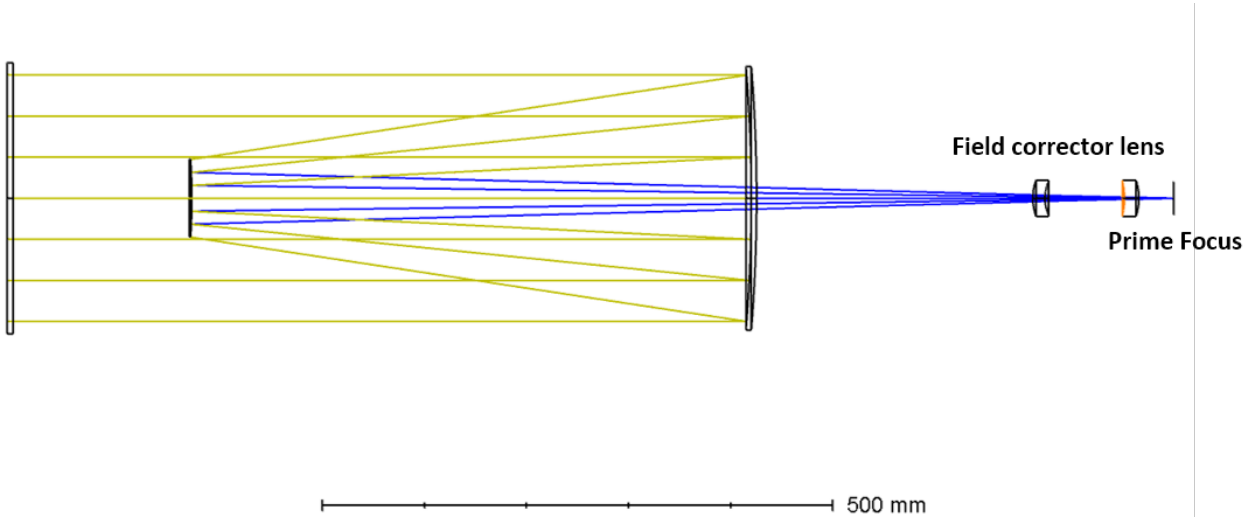

Figure 4.7: The optical layout of the SPRING FDIS telescope is shown. Total length is about 1.2 meters, focal length is 3.3 meters.

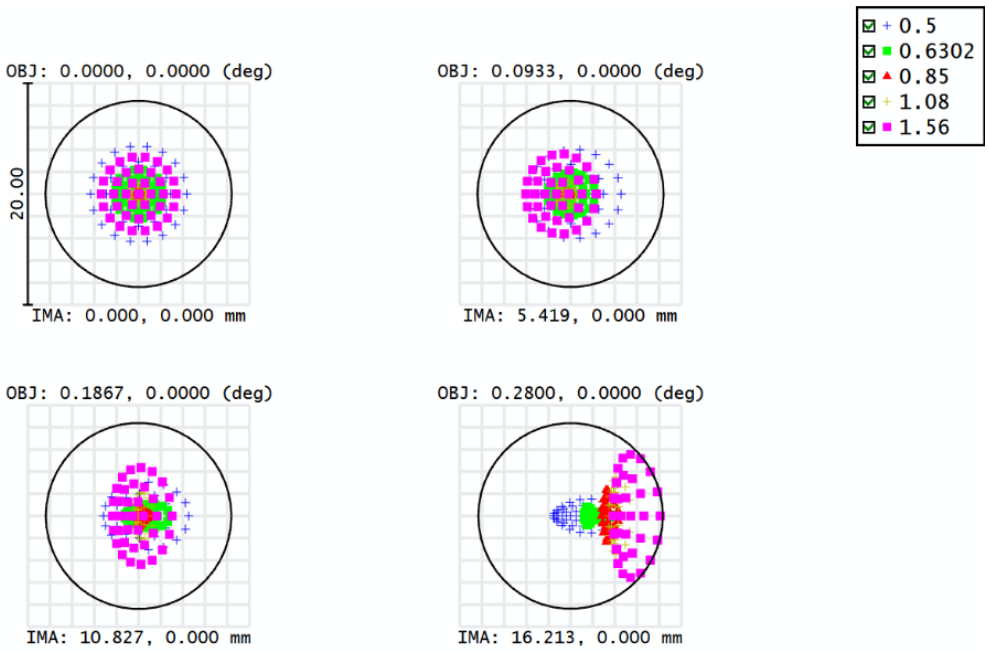

Figure 4.8 Spot diagram is shown for different field angles and for different wavelengths. The black circle marks the Airy disk corresponding to 0.5 micron wavelength.

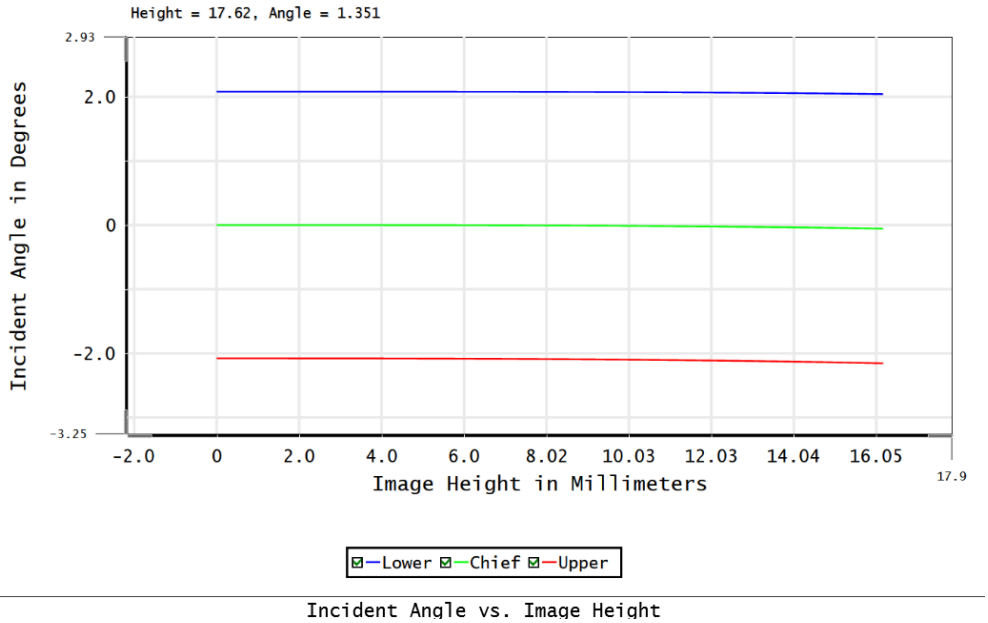

Figure 4.9: Incidence angle versus image height is shown here. The small variation of incidence angle with image height shows that the beam at the prime focus is nearly telecentric in nature.

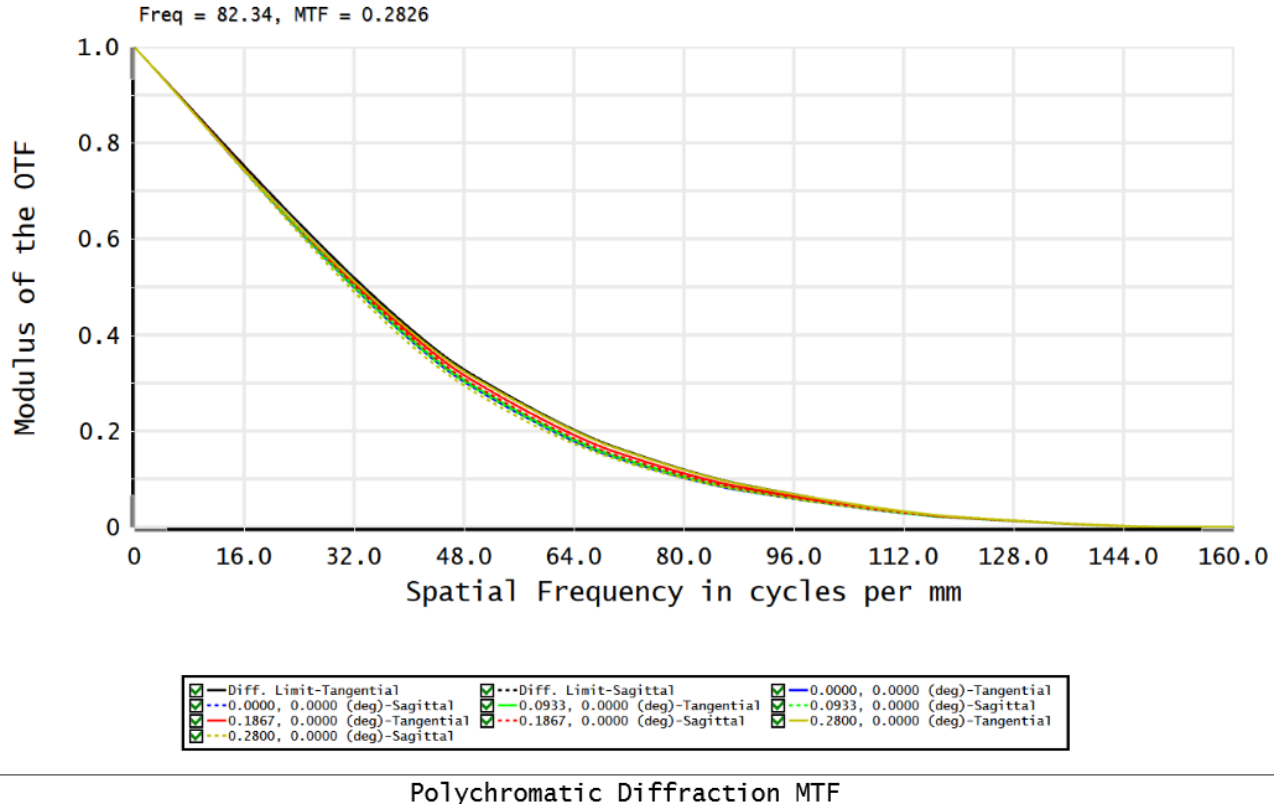

Figure 4.10: Polychromatic diffraction MTF is shown here for various wavelengths. The black line shows the diffraction limited MTF.

The modulation transfer function (MTF) of the SPRING FDIS telescope in Fig 4.10 shows that its performance is homogeneous over the wavelength range.

Telescope Mounts for SPRING: The smaller aperture telescopes FDIS(-B, R & IR) are compact enough that these can be mounted on equatorial systems. The beams can be folded if required after the prime focus, since the polarization modulation would take place before the beam is folded. A symmetric telescope directly looking at the sun without any oblique reflection is a prerequisite for accurate polarimetry.
The philosophy of SPRING would be to mount several telescopes on one mount, similar to SOLIS/VSM, except that the number of telescopes will be more in SPRING. Three FDIS telescopes of 25 cm aperture can be easily mounted on a platform side by side. The detailed mechanical design of the SPRING mount would depend upon the final choice and configuration of the suite of instruments. It has been discussed in the community that in the first priority would be to establish a core program of fulldisk multiline Doppler and magnetograms. There is interest in many other programs in the community such as flare research, in particular high cadence flare spectroscopy and polarimetry. These requirements call for a very focused instrument which must be developed by interested research groups and SPRING should be able to accommodate such non-core programs in few or all of the network nodes. Thus, the mechanical design of the SPRING equatorial mount should be such that it can accommodate third party instruments which require continuous monitoring

of the Sun such as flare research. There could be more such interests in the future such as the synoptic study of scattering polarization and the Hanle effect in the Sun and its solar cycle variability and also to understand the nature of turbulent magnetic fields.
When such interest is realized in the form of a set of instruments to be deployed, a rebalancing of the mount would be needed. An example of such a standard platform could be a flat breadboard type platform where any general purpose opto-mechanical mount could be used. Also, an extra set of the signal and power cables would need to be laid out for such future application. The telescope mount would need to be remote controllable and designed for automated operation. There should be a dedicated telescope control system, which will continuously monitor the local weather conditions and during inclement weather stops telescope observations, parks the telescope and brings the dome in close position. Pointing accuracy of the mount should be better than a few arcsec (5”-10”). Open loop tracking should be within a few arcsec (< 2” per 10 minutes), close loop tracking with guider (auxiliary guider tube, with quad cell or correlation tracker mounted parallel to the mount) better than 0.2” RMS over several hours during clear sky conditions. The mount should have fast and slow slew controls and should have emergency brakes. There should be enough clear room between telescope and dome so that operations are not hampered during various seasons. The ability to scan the Sun in RA and declination randomly up to several arcminutes, for flat fielding.
Due to diverse geographic locations of the SPRING telescopes (even different hemispheres of the Earth) require that the mount should have the ability to point and track the sun from horizon to horizon. Finite element analysis would need to be done for various elevation angles for all the locations to keep the flexure as minimal and uniform across the network as possible, for homogeneity of the data.
Further, the design of the mount should be adapted to the local climatic conditions such as excessive rains or humid conditions (during monsoon season, for example), or snow, or heat.

Dome design: The autonomous operation of the SPRING network of telescopes requires that the dome design should have a possibility for remote operation, autonomous operation, communication with telescope mount and weather station always to make sure the mount operation is not interfered with dome. The dome design for SPRING has the following options:
(i) a collapsible dome such as for GREGOR at VTT, or (ii) retractable dome such as for SOLIS/VSM (a shed which can be rolled back and forth when needed along with shutter which can be rolled up and down when the dome is in park position. The dome always slides in the sun shade-ward side to keep the dome seeing away from the telescope and not to obstruct the Sun itself.

5. BACK-END INSTRUMENTS

Concept 1: Fabry-Perot Interferometer based design

Full Disk Imaging Spectropolarimeter (FDIS)

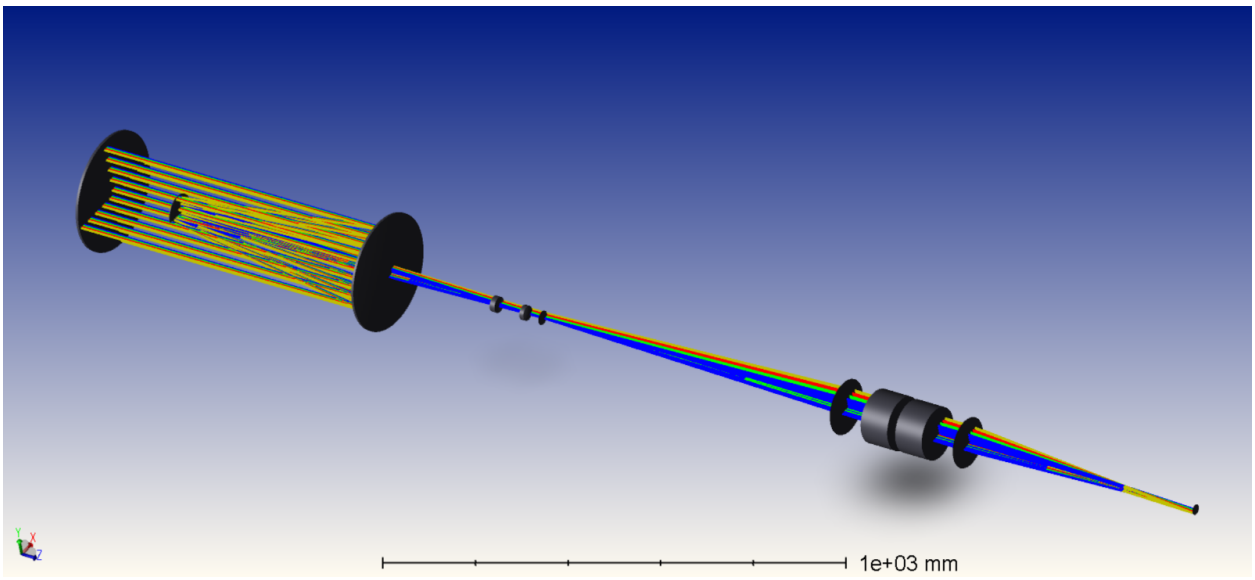

5.1 Introduction

The advantage of an FPI over other type of filters is, (i) high throughput, (ii) rapid wavelength tunability, and (iii) high spectral resolution. Fabry-Perot interferometers have been widely used in astronomical imaging spectroscopy, and in solar astronomy they have been used for imaging spectropolarimetry as well. There are various examples from solar applications, such as, TESOS (Kentischer et al 1998), Imaging Bi-dimensional Imaging Spectrometer (IBIS) (Cavallini et al 2010), GFPI (Puschmann et al. 2012), IMAX (Martinez-Pillet et al 2011), CRISP/SST (Scharmer 2006), HELLRIDE (Staiger 2008), USO/SVM (Gosain et al 2007), etc.

5.1.1 Suitability for SPRING

For the SPRING the observational requirements, FPIs seem to be strong contenders. The reason is that (i) they provide the ability to provide snapshot observations of the entire 2D field-of-view, while spectral dimension can be rapidly scanned, in order of few seconds, (ii) together with a simultaneous broadband imaging channel these spectral images can be improved by applying post-facto image reconstruction techniques, such as speckle interferometry (von der Lühe, 1993) and blind-deconvolution techniques (Lofdahl 2002). Such features are typically not available in slit scanning spectrographs, for example.

For FPIs highly sophisticated fabrication and coating techniques together with active control of parallelism in some designs allows very high optical quality to be achieved. FPIs are routinely designed and made for moderate to high spectral resolution and their clear aperture diameters have been demonstrated to work successfully in the order of 10 cm. Larger apertures are must when used with large aperture solar telescopes such as DKIST or when used with large field-of-view such as full disk observations. Much larger etalon apertures are being developed currently, such as the 25-cm aperture FPI, the visible tunable filter (VTF), being developed by KIS, Freiburg. The VTF is a first light instrument for the upcoming 4 m aperture, DKIST telescope at Hawaii (see http://www.nso.edu/dkist for details). Also, INAF, Italy has collaborated with ICOS Optical Systems, UK (formerly known as Queensgate Inc.) to study the development of 15 cm aperture, air gap, piezo based servo-controlled etalons. These developments are encouraging for the FPI based designs for SPRING instruments.

The basic requirement for SPRING is to acquire full-disk spectral images in multiple spectral lines. Adding polarimetry can be accomplished without affecting the FPI performance. By employing a broad-band coating design of FPI plates and relevant narrowband interference pre-filters these devices seem to be adequate for the SPRING observational requirements. Here we will first discuss some basics about the

FPI theory and operation modes and compare their advantages and disadvantages. Then we present a dual etalon based design and compute its expected performance.

5.1.2 Theory:

The performance of a single-pass Fabry-Perot etalon is given by the Airy formula, which essentially describes the intensity distribution of the light as a function of wavelength.

$$I_t = \frac{\tau}{1+F\cdot sin^2\frac{\delta}{2}} I_i \ = \Gamma\tau I_i \qquad (5.1)$$

Where I_i and I_t are incident and transmitted intensity respectively, τ is the etalon peak transmission related to the fraction of light absorbed, A, and reflectivity, R, as

$$\tau = (1 - A/(1-R))^2 \qquad (5.2)$$

The parameter F is related to the etalon surface reflectivity R by the equation

$$F=4R/(1-R)^2 \qquad (5.3)$$

The phase difference, δ, is given by

$$\delta=4\pi\ \mu t\ \cos\theta/\lambda \qquad (5.4)$$

where, t, is the thickness of the cavity, θ is the angle of incidence with respect to the plat normal, μ is the refractive index of the cavity and, λ, is the wavelength of the light. The interference condition is given by

$$2\mu t\ \cos\theta=m\lambda \qquad (5.5)$$

where, m, is the order of interference. The transmission is periodic and the intensity maximum values are reached for $\delta=2m\pi$. The free spectral range (FSR), or the distance between two successive maxima, represents the period

$$FSR = \lambda/m = \lambda^2/2\mu t\ \cos\theta \qquad (5.6)$$

For normal incidence and perfect parallel plates, the fullwidth at half maximum of the transmission profile is given by

$$FWHM=\lambda^2\ (1-R)\ /\ (2\pi\mu t R^{1/2}) \qquad (5.7)$$

The change of peak transmission wavelength with angle of incidence θ is given by the relation

$$\lambda(\theta)= \lambda_0\ (1-\sin^2\theta/\mu^2) \qquad (5.8)$$

where, λ_0, is the transmission maxima wavelength when the thickness of cavity is t_0,
For small angles this shift of transmission peak towards blue wavelengths can be written as

$$\lambda(\theta)= \lambda_0\ (1 - \theta^2/2\mu^2) \qquad (5.9)$$

The parameters F is related to so called reflective finesse, N_R by

$$N_R=\pi R^{1/2}/(1-R) = \pi\ F^{1/2}/2 \qquad (5.10)$$

For perfect plane parallel plates the finesse is dictated by the reflectivity of the coatings and absorption (absorption +scattering). However, in practical etalons the departure of the etalon plates from perfect flat surface and parallelism as well as

micro-roughness of surfaces leads to various degrading terms that can lead to a smaller value of finesse called effective finesse.

$$F_{eff} = \left(\frac{1}{F_R^2} + \frac{1}{F_S^2} + \frac{1}{F_G^2} + \frac{1}{F_P^2} + \frac{1}{F_I^2} + \cdots\right)^{-1/2}$$

$$= \left(\frac{(1-R)^2}{\square^2 R} + \frac{4\delta t_s^2}{\lambda^2} + \frac{22\delta t_g^2}{\lambda^2} + \frac{3\delta t_p^2}{\lambda^2} + \frac{m^2\theta^4}{64} + \cdots\right)^{-1/2}, \quad (5.11)$$

Where δt_s is the peak-to-valley deviation from perfect flatness, δt_g is the plate rms-deviation, δt_p is the plate deviation from parallelism, and θ is the angular size of the accepted beam.

The absolute phase of the wave front after passing through the filter for the case of single etalon is given by

$$\emptyset = arctan\frac{R\sin\delta}{(1-R\cos\delta)} + \frac{2\pi\ \mu t}{\lambda} \quad (5.12)$$

5.1.3 Classic versus Collimated Mount:

Two ways in which a FPI can be mounted in imaging instruments are the (i) collimated and (ii) telecentric modes. Let us first discuss the collimated or sometimes called classical mount. In collimated mount (CM) the FPI is placed near the image of the entrance pupil. The bundle of rays from the pupil travels through an imaging lens onto the detector. Thus, the rays corresponding to each pixel propagate through the interferometer at the same angle with respect to the optical axis. This leads to a field-dependent wavelength shift of the transmission passband. In practice, the ray bundle associated with each image pixel covers an area of the FPI plates within which the plate separation fluctuates due to imperfections of plates. Thus, in this case the FWHM of each order of the FPI is larger than the perfect reflective case (i.e., case of perfect plates and coatings, limited only by reflectivity). For the case of normal incidence this is given by second term in the equation:

$$\delta\lambda_{cl} = [\ \delta\lambda_R^2 + \delta\lambda_D^2]^{1/2} = [\ (\lambda^2(1-R)/2\pi\mu t\sqrt{R})^2 + (\ \lambda^2/pt)^2\ ]^{1/2} \quad (5.13)$$

where p is the large-scale flatness error in fractions of λ.

The field-dependent wavelength shift is given by

$$\Delta\lambda_\theta = -\lambda\theta^2/2\mu. \quad (5.14)$$

In case of the telecentric mounting (TM), the entrance pupil is collimated and the FPI is placed near the image plane. Consequently, all image points are formed by ray cones normally incident on the interferometer and containing all possible directions allowed by optics. In this case, the FWHM of each order of the FPI is larger than the reflective perfect case, because the ray bundle corresponding to each image point contains a range of θ values. Moreover, as the plate separation is not infinitely small, the ray cones always cover a small but finite area of the FPI plates, and therefore, on

each point of the final image plane, the FWHM of each order is also broadened by small scale flatness fluctuations. The FWHM ($\delta\lambda_{tc}$) of the interferometer orders will be broadened by the flatness errors as well as by the varying angle θ, accounted for by the 2nd and 3rd terms respectively on the following equation:

$$\delta\lambda_{tc} = [\delta\lambda_R^2 + \delta\lambda_D^2 + \delta\lambda_\theta^2]^{1/2}$$
$$= [\ (\lambda^2(1-R)/2\pi\mu t\sqrt{R})^2 \ + (\lambda^2/\bar{p}t)^2 + (\lambda\theta^2/8\mu)^2\ ]^{1/2} \qquad (5.15)$$

where $\bar{p}$ is the small-scale flatness (microroughness) errors in fractions of λ. Large scale flatness errors manifest as spatially varying transmission function across the field-of-view.

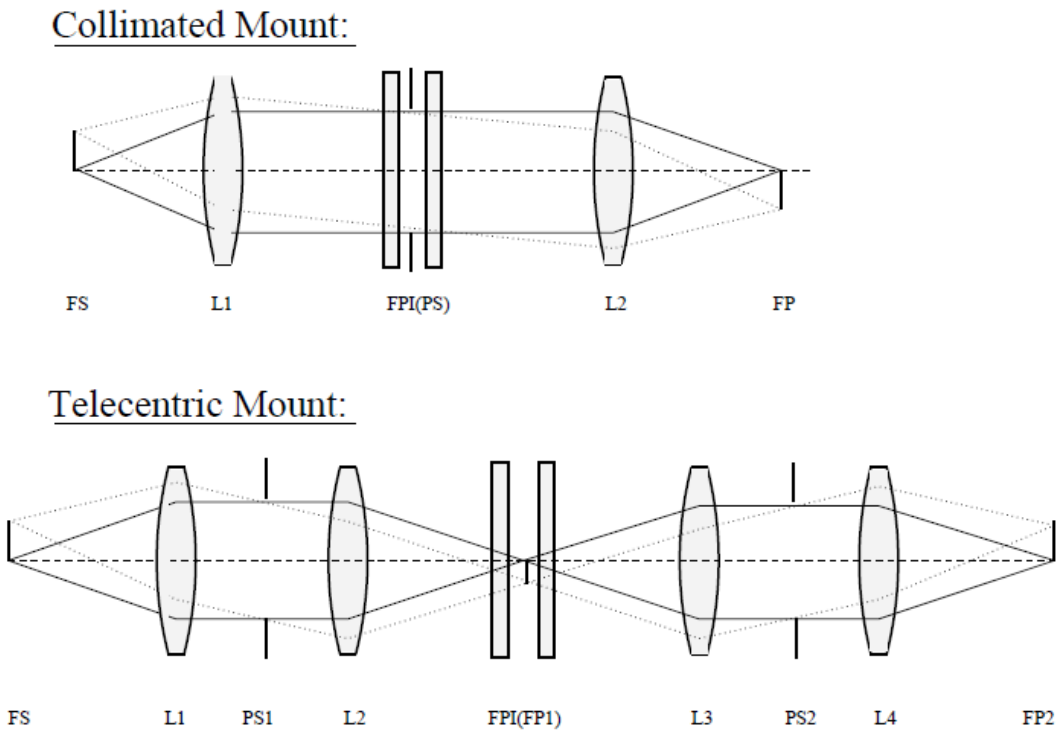

Figure 5.1: The mounting options for FPIs are shown above. In the top (bottom) panel a collimated (telecentric) mount is shown. In the collimated mount the telescope aperture (PS) is imaged into the interferometer, L2 is a reimaging lens. In the telecentric configuration, lenses L1 and L2 project the solar image (FS) into the interferometer. Lenses L3 and L4 image the solar image onto the detector.

5.2 Collimated v/s Telecentric for SPRING

5.2.1 Telecentric Mount Option:

The comparison between the TM and CM mounts in the previous section is basically the discussion in Cavallini (2006), and Kentischer(1998) summarized in Table 5.1. It is clear that for a proper mapping of full disk velocity signals one would require a uniform filter transmission across the field-of-view. Due to plate flatness errors the

field dependent transmission profile shape and transparency can be very troublesome and tedious to correct specially with such high data rates (tens of spectral lines every minute, 24x7). Even if differential velocity measurement may not be an issue for high L modes, for low L values this may be a problem.

Table 4.1 A comparison between collimated and telecentric Fabry-Perot interferometer mounts.

	Collimated	Telecentric
Broadening mechanisms	reflectivity and plate shape	reflectivity and f-number
Wavelength shift across	yes	No
Wavefront distortion	large	low
Influence of Dust on the	low	large
Alignment sensitivity	large	low
Blocking Ghost reflections	difficult	easy
Influence of plate shape	broadening	λ-shift
λ related pupil apodization	No	Yes

Another issue with the telecentric option is that the passband broadens significantly at low f-numbers (f#=f/D ratio <100). For large field-of-view observations such as full solar disk (0.54 degrees) with a 25 cm telescope would need a path length >>3 meters. This will be a major issue when multiple telescopes are housed on single mount/platform. It should be emphasized that even with moderate aperture size of 25 cm this is an issue, hence larger aperture telescopes can be ruled out with telecentric mounting for full disk observations especially when designed to work on equatorial mounts.

5.2.2 Collimated Mount Option:

Now we consider the collimated mount option for SPRING FDIS. Fig. 5.2 below shows how the passband of the FPI of various aperture sizes, commercially available, would shift (blue-wards) from disk center to limb position, as a function of wavelength. It is seen that for a moderate sized FPI of 7.5 cm aperture the shift is as high as 1.7 Å for the Fe I 1.5 micron spectral line, while for most shorter wavelengths, i.e., lines from 3933 to 6767 Å, the shift is < 0.75 Å. For a 10 cm aperture etalon, this value is 0.9 Å for the Fe I 1.5 micron line and is <0.4 Å for

shorter wavelengths mentioned above. Finally, for a 15 cm aperture etalon the shift for the IR 1.5 micron line is 0.4 Å and for all shorter wavelength lines are < 0.2 Å. The typical scan step size during the FPI wavelength scan is 10-40 mÅ, depending upon the spectral line. This means that to compensate this shift we would need to scan extra steps towards the red. The number of extra steps needed to compensate for a passband shift across field-of-view is typically 10-15 for a 15 cm aperture etalon, and 20-30 steps for a 10 cm aperture etalon. However, the rapid tunability of etalons and fast cameras together would allow to make up for the passband shift across the field-of-view.

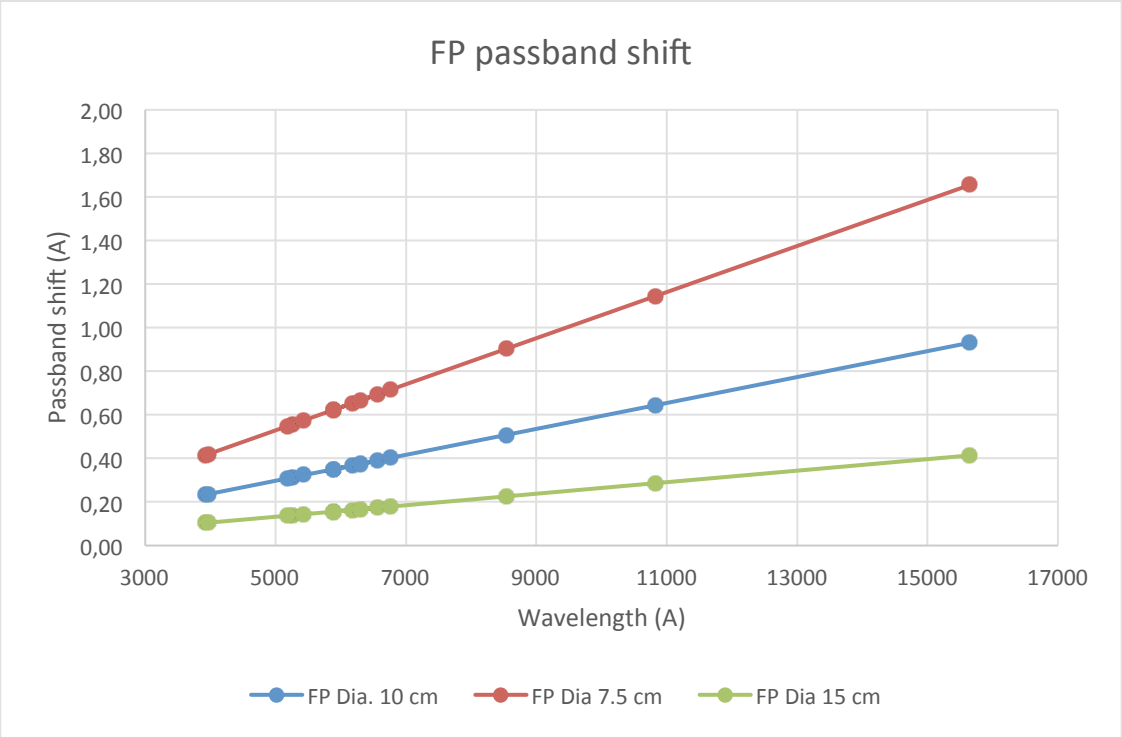

Figure 5.2: FPI passband shift with field-of-view for etalons of various aperture sizes when used with telescope FDIS of aperture 25 cm. The passband shift is shown as a function of spectral line and increases with wavelength.

The table 5.2 below shows the list of spectral lines, the number of wavelength scan steps needed to scan the line with 40mÅ sampling, time required to acquire the scan with desired SNR for full Stokes polarimetry (therefore it also meets SNR requirements for velocity measurements), and time required when passband shift is also accounted for. It is assumed that the telescope size is 25 cm (FDIS telescope) and the etalon has an aperture size of 10 cm. The total time per channel is shown at the bottom rows. As can be seen that the acquisition time for all channels is still within the 30 second cadence limit. We have also computed the timings when a FPI of 7.5 cm aperture is used with a passband of 80mÅ. System transmission is 3%. The

acquisition time per cycle still remains under the 30 seconds cadence requirements imposed by helioseismology. Details of these computations and assumptions of the observing setup are given in Appendix A.

Table 5.2 The spectral lines, the number of wavelength scan-steps (spaced at 40mA) needed to sample the line with the desired SNR, time required to scan the line (column A) and time required to scan the line including passband shift across the field-of-view (column B) are given. The lines observed by FDIS-B, R and IR channels are shown by blue, red and black color, respectively. The bottom row gives total time for each channel.

Line	No. of wavelength scan steps	(A) Time (seconds) to scan the line with desired SNR	(B) Time (seconds) to scan the line+ shift over the FOV	SNR achieved
Ca II K (3933)	48	2.22	2.55	1979
Ca II H (3968)	30	2.32	2.92	2053
Fe I (5250)	10	1.70	3.61	1590
Mg B2 (5173)	39	1.69	2.00	2058
Fe I (5434)	16	1.73	2.69	1807
Na I D (5896)	35	1.79	2.24	1844
Fe I (6173)	11	2.32	5.70	1757
Fe I (6302)	13	2.02	4.16	1673
H I alpha	54	2.06	2.48	1437
Ni I (6768)	12	1.96	4.30	1326
Na D1 (5890)	37	1.63	1.96	1500
Ca II (8542)	85	1.87	2.15	1489
He I (10830)	35	1.64	2.32	1526
Fe I (15648)	21	1.55	3.05	1421

	Blue	Red	IR
TOTAL TIME Column (A)	9.67 (s)	11.79 (s)	5.07 (s)
TOTAL TIME	13.75 (s)	20.85 (s)	7.52 (s)

Column (B)			

5.2.3 Number of FPIs in tandem configuration

The SPRING FDIS requires a narrow passband of ~80 mÅ for scanning the spectral lines. For the given FPI however this passband will vary with wavelength thus the passband should remain on an average ~80mÅ within the wavelength range such as in the FDIS B, R and IR channels. The spectral resolution $R=\lambda/\Delta\lambda$ would therefore be in the range 50,000 to 200,000 in all FDIS channels. This resolution is adequate to sample the solar photospheric spectral lines and more than adequate for chromospheric lines.

Although the spectral resolution mentioned above can be achieved with a single FPI, however, the free spectral range (FSR) would be rather small which will limit the useful wavelength scanning range and will lead to a significant amount of parasitic light from side orders contaminating the spectra and affecting the SNR. For example, for a typical finesse of 50, with passband of 80 mÅ we get a FSR of 4 Å, which would then require the use of a very narrow pre-filter (~1.5 - 2Å) and will limit the useful wavelength range. Typical solar chromospheric lines would require a much larger scanning range than this value. The FSR can be increased with multiple FPIs operating in tandem, i.e., one following another. Typically, the cavity spacing are chosen such that the interference orders of the two FPIs overlap at significant spectral distance. This increase in FSR is a function of number of FPIs. Three FPIs would give a much larger FSR advantage than two FPIs, but the complexity and associated problems of maintaining the passbands synchronized during scan, inter-etalon reflections and impact on image quality also increase.

Here we consider a dual FPI design for the FDIS instruments to keep the complexity of the instrument low while meeting the requirements for SPRING. We remind ourselves that FDIS will be three identical separate instruments mounted in parallel on a equatorial platform. Each channel observes a wavelength range as described below

FDIS-B: 3933, 3968, 5173, 5250, 5434 Angstroms →(380-550nm)
FDIS-R=5890, 5896, 6173, 6302, 6563, 6768 Angstroms →(550-850nm)
FDIS-IR=8542, 10830, 15648 Angstroms →(850-1600 nm)

5.2.4 Characteristics and Optical Setup of FDIS

The optical setup for FDIS would be a collimated mount with an FDIS telescope of 25 cm aperture. The optical layout of the FDIS instrument is shown in Fig. 5.3 below. The primary imaging system is a Ritchey-Chretien telescope (RCT), based on the SOLIS/VSM design, scaled down to 25 cm aperture. The secondary mirror also acts

as active tip-tilt correction system (ATTS). PCU is the polarization calibration unit that can be inserted into the beam during calibrations. BS is a beam splitter which taps 5% to the main beam for white light camera (WLC), which also provides correction signal for ATTS. FCL is field correction lens system and F1 is the prime focus. FW is the filter wheel which hosts sequence of interference filters for multiline observations, done sequentially. PM is the polarization modulation assembly. CL (focal length=800mm), FP1, FP2 and IL (focal length=600mm) are the collimating lens, Fabry Perot etalons no1 & 2, and imaging lens, respectively. PBS is the polarizing beam splitter, which analyses the polarization of light and sends two orthogonal components to cameras, CAM1 and CAM2. The etalons FP1 and FP2 are assumed to be 10 cm aperture etalons. The cameras are assumed to be 4k x 4k, 6.5 micron pixels, full well 40ke$^-$, and readout speed of 100 frames per second, 14-bit digitization. Cameras would need to be chosen for maximum quantum efficiency (QE) in respective wavelength range. BS, FP1, FP2, PBS, would need to be optimized for coatings for each wavelength channel. The image size, solar disk, in the camera focal plane is 24 mm.

The PCU will consist of a linear polarizer and achromatic retarder for polarization calibration. To prevent damage to PCU optics from high solar flux a broadband pre-filter cantered around each line in that FDIS channel would need to be placed via a filter wheel or sliding assembly located just in front of the PCU (as a part of PCU). During solar observing the PCU optics would be removed from the optical path via computer control. The filter wheel FW will always be in the beam during calibration and solar observations, with appropriate filter in the optical path. The FW will house several filters either as a circular wheel or translation two-axis stage that will allow automated fast positioning of filters during solar observations and calibration. These filters will prevent the heat load and ultra-violet damage to the polarization modulator optics which will be based on liquid crystal retarders.

The FPIs will be kept as close to each other as possible, so that the image of the entrance pupil is located in between the two etalons. The outer surfaces of FPIs will have optimized anti-reflection coatings for specific wavelengths to reduce fringes. Also, the ghost images from back reflections from rear surfaces of etalons will be displaced in the image plane due to wedge angle in them. The gravitational flexure problem in 10 cm aperture etalons is assumed to be negligible compared to 15 cm aperture etalons, as their weight is only 400 g compared to 1.5 kg for 15 cm etalons. However, this needs to be carefully studied in detailed design phase.

The housing of etalons would need to be designed as a stable thermal environment. One can also think of containing the entire FDIS assembly (telescope and backend) in a sealed environment filled with Helium, which can help minimize internal seeing in the instrument and keeping thermal environment stable by circulating Helium inside the instrument via a temperature control system.

Dual cameras will need to be synchronized with each other and with the polarization modulator and the FPIs. This would need a hardware trigger mechanism to synchronize all devices very precisely.

Figure 5.3: Schematic of FDIS generic design. The primary imaging system is a Ritchey-Chretien telescope (RCT), based on SOLIS/VSM design, scaled down to 25 cm aperture. The secondary mirror also acts as active tip-tilt correction system (ATTS). PCU is the polarization calibration unit that can be inserted into the beam during calibrations. BS is a beam splitter which taps 5% to the main beam for white light camera (WLC), which also provides correction signal for ATTS. FCL is field correction lens system and F1 is the prime focus. FW is the filter wheel which hosts sequence of interference filters for multiline observations. PM is the polarization modulation assembly. CL, FP1, FP2 and IL are collimating lens, Fabry Perot etalons no1 & 2, and imaging lens, respectively. PBS is polarizing beam splitter which analyses the polarization of light and sends two orthogonal components to cameras, CAM1 and CAM2.

4.2.5 Choice of FPI spacing ratio

For each spectral channel, we need to decide a pair of FPIs with cavity spacings such that the requirement of spectral resolution is met with a pre-filter of reasonable bandpass. The decision is made by using the approach followed by Cavallini (2006) for the IBIS design. The optimum ratio between the interferometer cavity spacings is given by the ratio that, for a given pre-filter (PF), gives the least amount of parasitic light, P, which is defined as the ratio of the light passing within the common transmission passband and outside of it, as

$$P = \left[\int_0^{\lambda_1} \mathcal{T}(\lambda)\,d\lambda + \int_{\lambda_2}^{\infty} \mathcal{T}(\lambda)\,d\lambda\right] \Big/ \int_{\lambda_1}^{\lambda_2} \mathcal{T}(\lambda)\,d\lambda, \tag{5.16}$$

Where, $T(\lambda)$ is the product of the transmission profiles of the two etalons and the order sorting pre-filter (an interference filter), and λ_1 and λ_2 are two wavelengths on either side of the combined peak FPI transmission profile at λ_0, where $T(\lambda_1)=T(\lambda_2)<<T(\lambda_0)$. The outer range of integration are taken to be +/- 2 nm on either side of the peak transmission of the dual etalon. The transmission profile of a single FPI is given by equation (5.1). Let $T_{IF}(\lambda)$be the transmission function of the pre-filter which can be approximated as a Lorentzian function,

$$\mathcal{T}_{IF}(\lambda) = \tau_{IF}\left[1 + (2\Delta\lambda/\mathrm{FWHM}_{IF})^{2n}\right]^{-1} \tag{5.17}$$

Where, $\tau_{IF,}$ is the peak transmission of the pre-filter and $\Delta\lambda$ is the wavelength offset from the combined peak transmission of the two FPIs, and $FWHM_{IF}$ is the full-width at half maximum of the pre-filter. Thus, $T(\lambda)$ is given as

$$\mathcal{T}(\lambda) = \tau_{IF}\left[1 + (2\Delta\lambda/\mathrm{FWHM}_{IF})^{2n}\right]^{-1} \times \\ \times\, T_0^2 \prod_{i=1}^{2}\left[1 + 4R\,(1-R)^{-2}\sin^2(2\pi t_i/\lambda)\right]^{-1}, \tag{5.18}$$

where, μ is the refractive index of the air in between the FPI plates, $\theta=0$ (normal incidence). We assume the same value of R, A, flatness, microroughness and parallelism errors for the two FPIs. The parasitic light, P, is then evaluated using Eq. (5.16) for the different spectral FDIS channels blue, red, and infra-red. We allow a different choice of $FWHM_{IF}$ for each line, since each line has a different width, mostly broader pre-filters for chromospheric lines. The Table 5.3 lists the etalon cavities for the three FDIS channels. The value of FWHM varies within each channel for different lines, narrower for shorter wavelengths and broader for longer. Further, it should be noted that this is the nominal spacing ratio, shown here as working solution. The other good ratios obtained were 0.272, 0.6 etc for different wavelength regions. However, in detailed design one needs also to study in detail more realistic case when the pre-filter shapes (2 v/s 3 cavity design), different reflectivity of the two etalons and distribution of errors etc. are also considered.

5.3 A software simulator tool for tandem FPI design

We have developed an interactive FPI simulator for studying tandem FPI systems. The graphical interface is developed for windows and uses an IDL program in background. The interface is displayed in Fig 5.4.The parameters of the individual FPI can be tuned and transmission profiles visualized. Using interactive cavity tuning options one can visualize combined profiles for the two etalons. The solar flux atlas is built-in for simulating synthetic solar scans and the effect of various parameters on the resulting profiles. The value of parasitic light can also be computed for various configurations. The software also allows generate pre-filter profiles of various bandpass and shapes and simulates 12-bit digital tuning of the etalon cavity as done in piezo driven systems.

Table 5.3 FPI cavity ratios for the three channels FDIS-B, R and IR

	Cavity length (microns)
FDIS-B	RatioFP1/FP2: 0.4
FP1	216
FP2	540
FDIS-R	Ratio FP1/FP2=0.4
FP1	416
FP2	1040
FDIS-IR	Ratio FP1/FP2=0.4
FP1	1400
FP2	3500

In Fig 5.5 and 5.6 we show the parasitic light analysis for the blue and red channels, the infra-red channel is not shown for brevity. In summary, a spacing ratio of around 0.4 works well for suppressing sidebands and provides least parasitic light. Using this ratio, we use our simulator to observe the solar spectrum under various settings and reproduce the synthetic observations. The solar spectrum for all the lines is well reproduced and are shown in the Appendix B. The scan was simulated as if the CS100 servo controller that is used with the FPI from IC Optical systems (the only company with makes air gap etalons with capacitive gap sensing, servo controlled and piezo driven).

The software tool also allows the visualization of the spectra derived for various pre-filter passbands so that optimal value can be specified when ordering the pre-filters. Further, the coatings of two etalons were assumed to be the same. The simulator allows to vary the reflectivity, surface flatness and cavity errors, absorption etc. between the two etalons so that a best combination can be ordered when specifying the etalons for fabrication.

5.4 Simulation using Solar Data from SOLIS:

It is insightful to simulate the performance of the theoretical instrumental profile with real solar data. While realistic MHD simulation data is used in various studies where instrument performance is to be evaluated, full-disk simulations of that nature are not available. Thus, we chose to use the real solar data for this purpose. One of the possibilities was to use SDO HMI full-disk data for this purpose, however, due to the limited wavelength span of these data (HMI samples only 6 positions across the spectral line) it is less favorable. GONG is even less as it scans only three positions across the line. The only high resolution fulldisk spectra is then from SOLIS/VSM and possibly from the Solar flare telescope (infra-red polarimeter). We decided to use the SOLIS/VSM full disk spectral cubes $I(x,y,\lambda)$ to simulate the synthetic observations as would be expected from the FDIS dual FP instrument, for the full disk field-of-view.

SOLIS/VSM is a long slit spectropolarimeter that obtains, via slit scanning, the 3D data cube of the full disk at a spectral resolution of 40mÅ, in Fe I 6301 line pair. In Figure 5.7 we can see the Fe I 6301.5 spectral line as a dark concentric ring (due to angular shift of FP passband the spectral sampling over full disk is shifted in wavelength space, which leads to this concentric ring appear to grow from disk center to limb as one proceeds with the wavelength scan with the FPI). The disk center and limb spectra are shown in the bottom two panels, with prefilter-profile modulating the solar spectra obtained by sampling the SOLIS data with dual FP transmission profile. The shift in the sampled spectra is evident in solar spectral lines displayed in bottom panels.

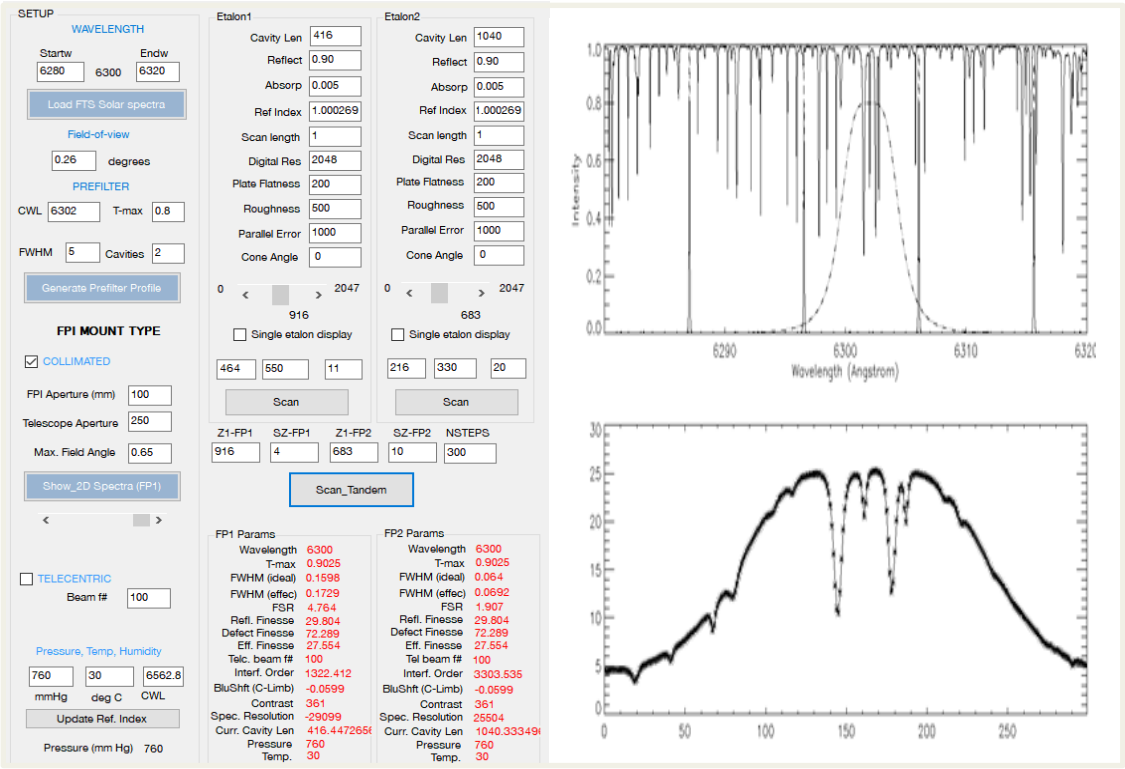

Figure 5.4 A graphical interface to simulate the FPI transmission. The optimum ratios were obtained using this software by analyzing parasitic light. Using that ratio, the observations of the solar spectrum (bottom right) were simulated, where input solar spectrum (top right) is from FTS atlas.

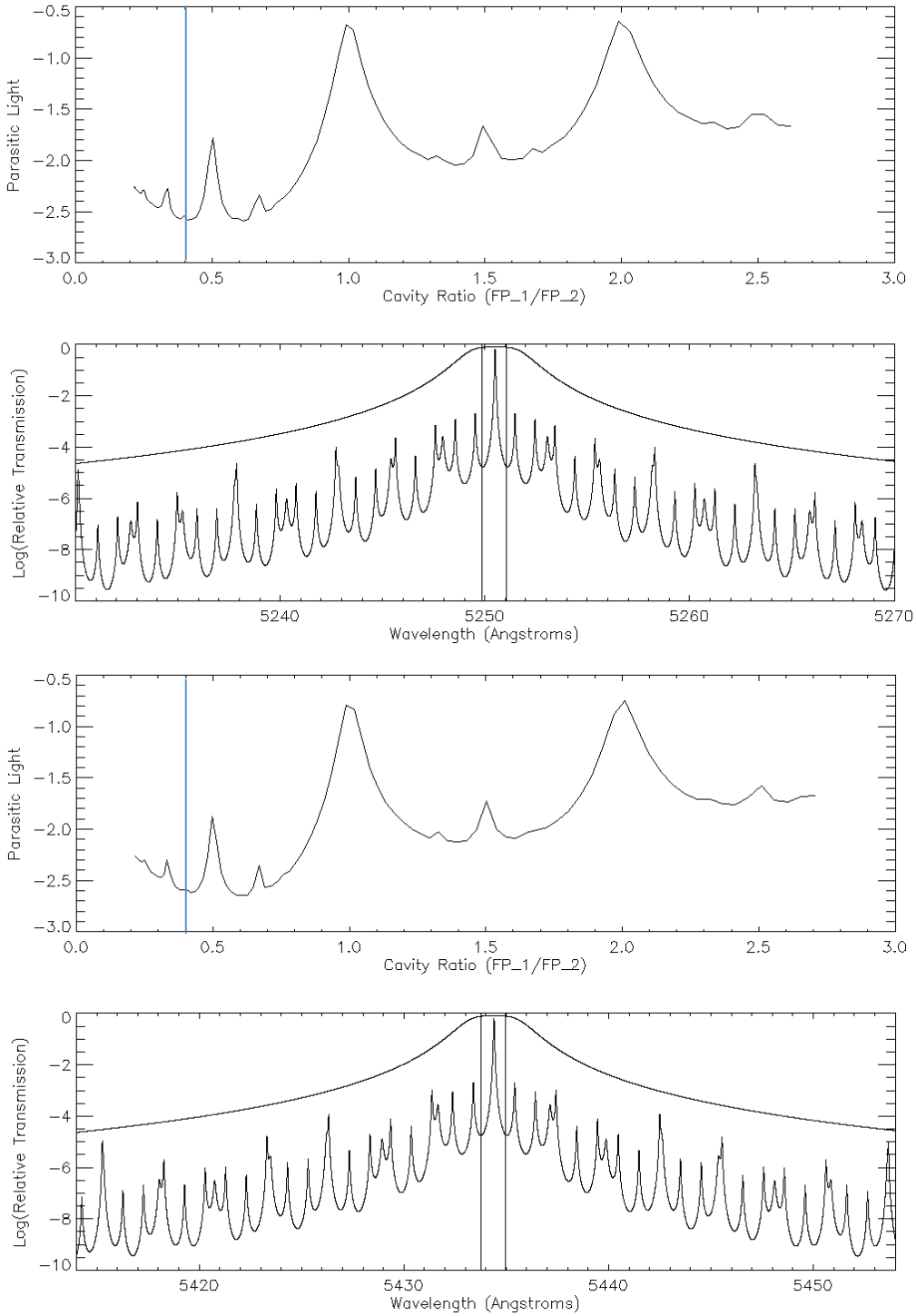

Figure 5.5: Parasitic light analysis for the representative lines Fe I 5250 (top panel) and Fe I 5434 (bottom panel) is shown for the FDIS-Blue channel. The cavity length ratio of 0.4 is selected as the region of least parasitic light.

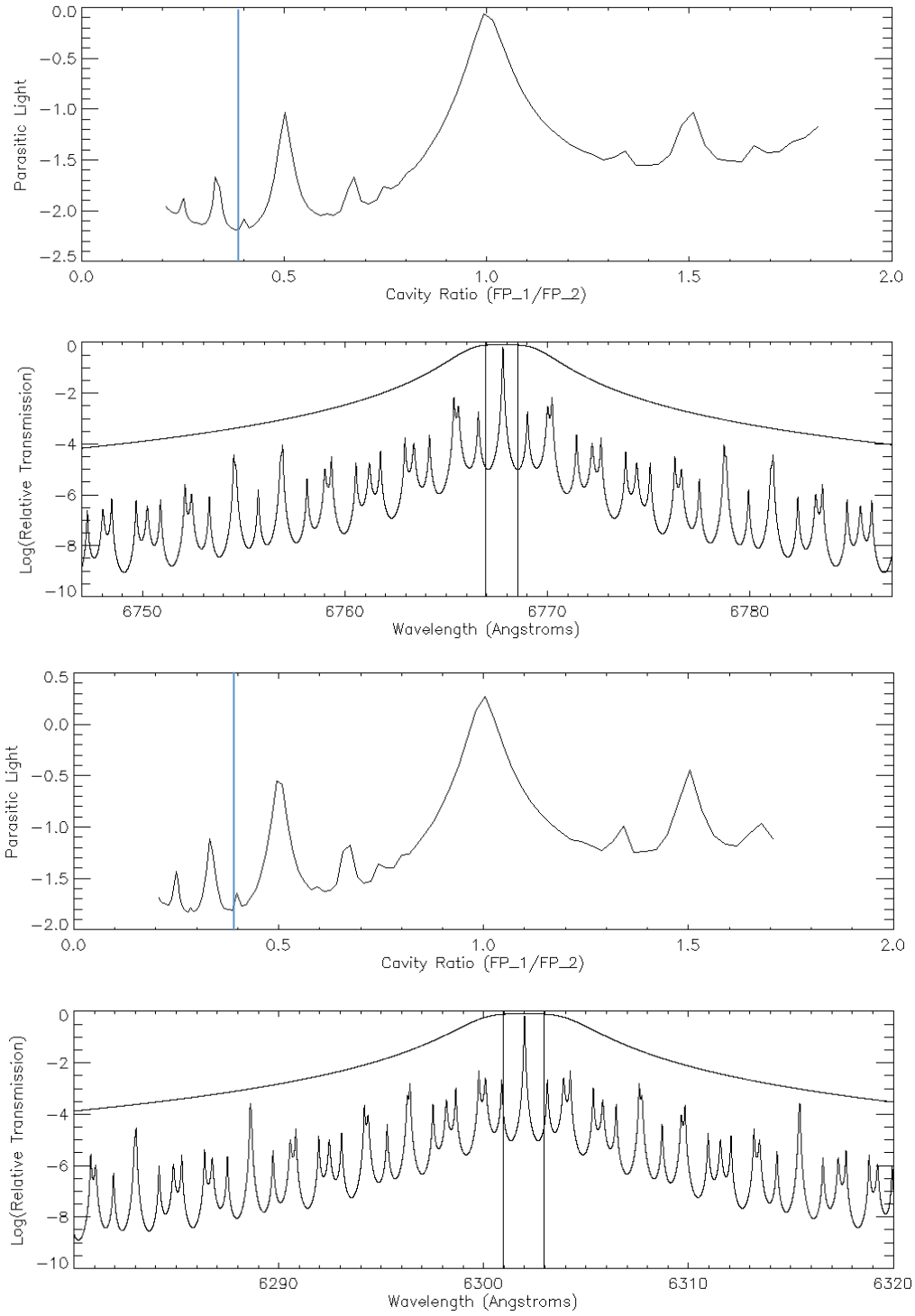

Figure 5.6: Same as Fig. 5.5, but for the representative lines Ni I 6768 (top panel) and Fe I 6302 (bottom panel) is shown for FDIS-Red channel. The cavity length ratio of 0.4 is selected as the region of least parasitic light.

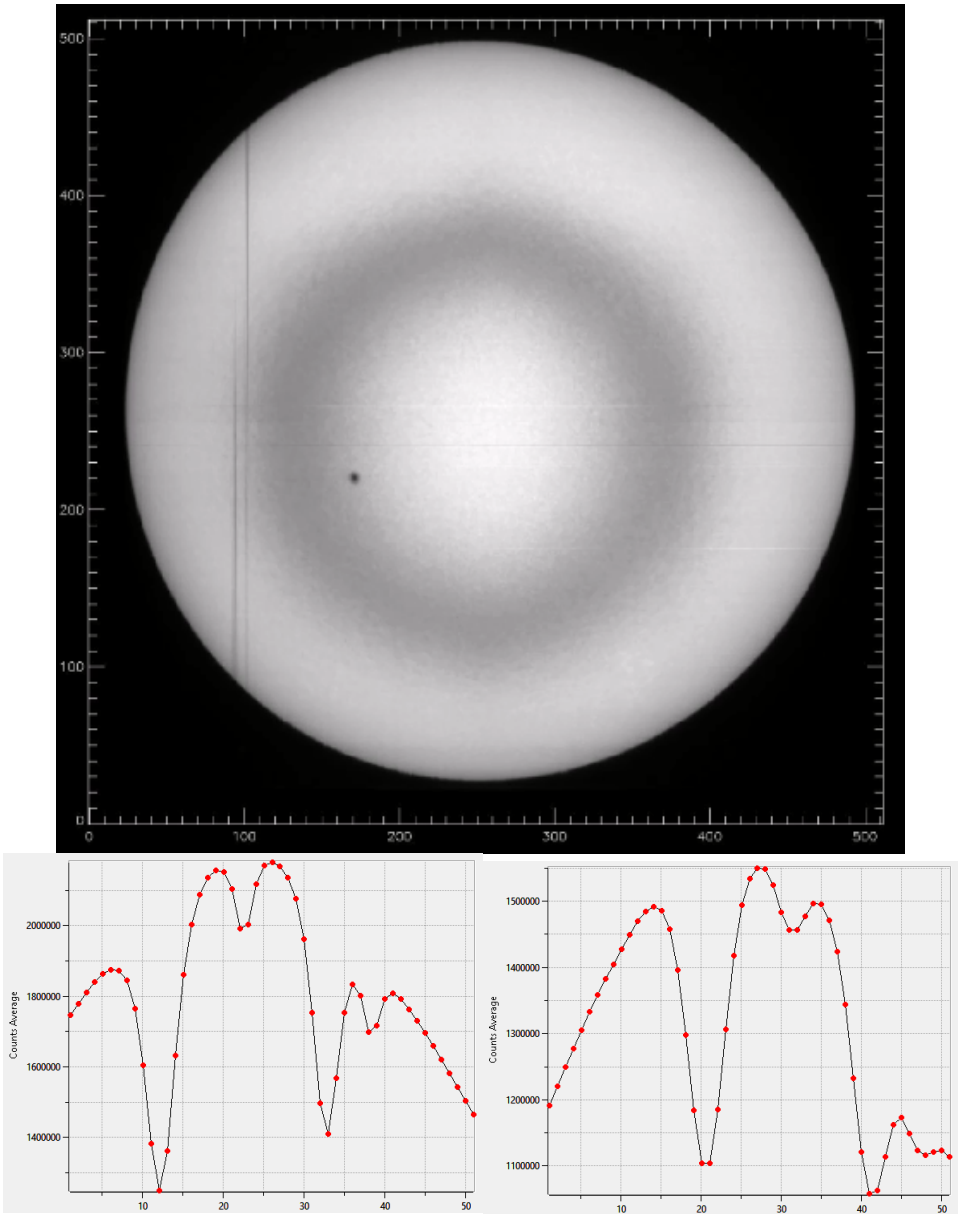

Figure 5.7: In this figure the top panel shows the snapshot of the simulation of the FPI observation of full disk using 3D data cube from SOLIS/VSM for Fe I 630 nm line pair. The spectral line is seen as concentric ring (due to angular shift of FP passband the spectral sampling over full disk is shifted in wavelength space, which leads to this concentric ring appear to grow from disk center to limb as one proceed with wavelength scan with FPI). The disk center and limb spectra are shown in the bottom two panels, with prefilter-profile modulatingthe solar spectra. The shift in the sampled spectra is evident in solar spectral lines.

5.5 Proof of concept: Test observations at VTT, Tenerife:

Finally we decided to test the proof of concept of using dual etalon FPIs to obtain full disk Dopplergrams. Such facilities do not yet exist for fulldisk field of view, albeit for limited field many instruments are available. One of the instruments is the HELLRIDE (Helioseismic Large Region Interferometric Device) instrument at the VTT (Vacuum Tower Telescope) Tenerife. The dual FP based device was designed for multi-line studies of large area (100 arcsec field) mainly for local helioseismology. We modified the HELLRIDE setup for obtaining fulldisk observations in multiple lines. Since the VTT does not allow a fulldisk image we proceeded to the guider port where a full disk image can be made with the simple refractor by tapping portion of the beam from the auxilliary port. A simple setup is shown in below in Fig 5.8. See caption for details of the setup.

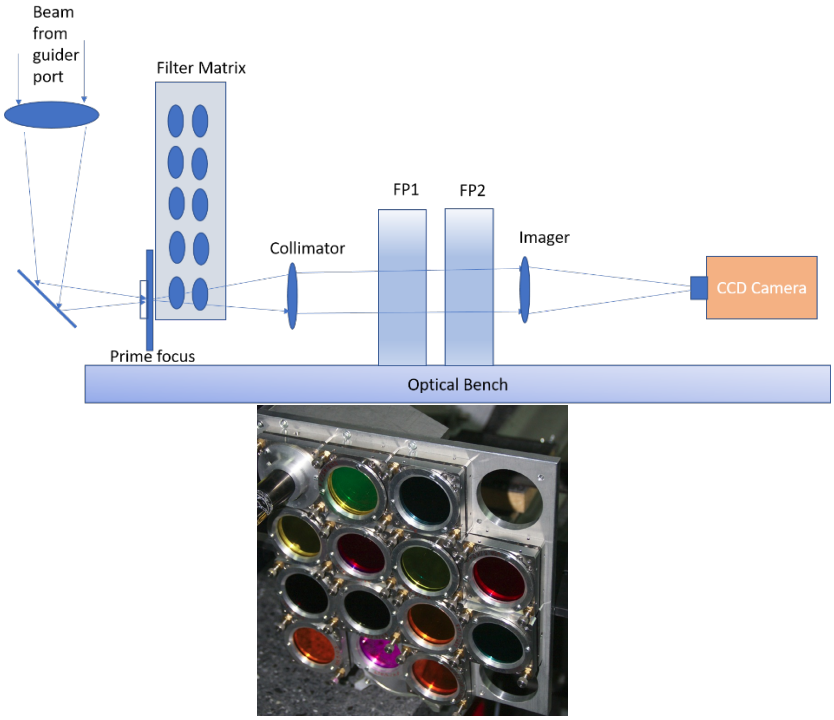

Figure 5.8 Optical schematic of the HELLIRDE instrument modified for full disk observations on the 9th floor of VTT telescope at Tenerife is shown on the left panel. A refractor is used to make primary image of the full disk. A large iris is used to allow little more than full solar disk (to avoid stray light from mirror reflections). The filter matrix is a 4x4 array of pre-filters than can be moved quickly into the optical path immediately following the prime focus. A collimator lens then collimates the solar beam through the two FPIs and a imager lens makes full disk image of the sun on the DALSA 1kx1k CCD camera. The panel on the right shows the actual picture of the filter matrix housing several filters. Sample Dopplergrams in Fe I 16173 line is shown below on the left, while on the right is the running difference of 1 minute Dopplergrams.

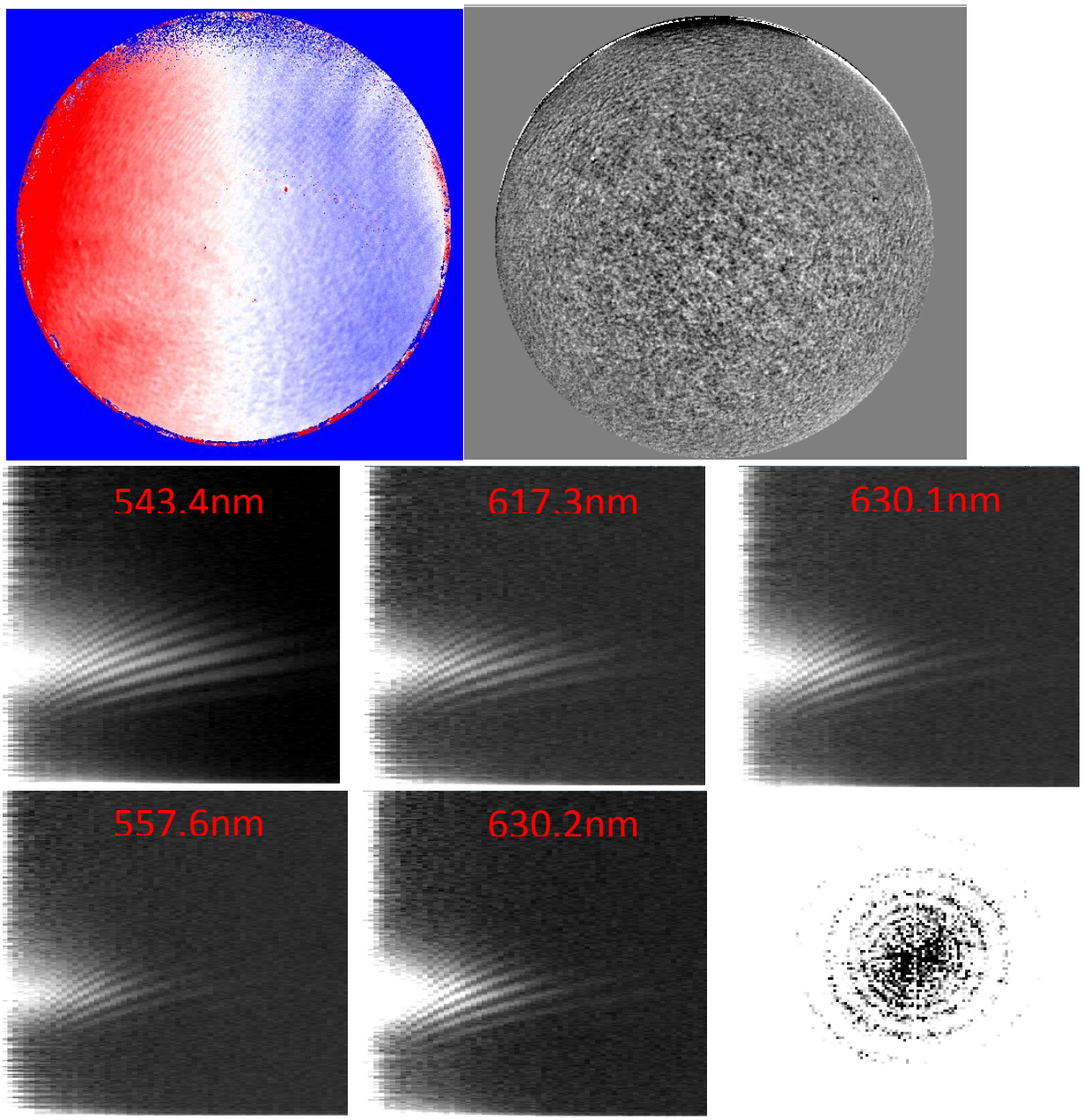

Figure 5.9 Power spectra of the full disk oscillations in various spectral lines are shown here. The power spectra correspond to the spectral line labelled in red. The bottom right plot shows the example of ring diagram derived from the observations.

The full disk observations were obtained in 10 different spectral lines with a cadence of 1 minute. Data reduction procedures such as flat field, dark and velocity computation were done on-the-fly. The ring diagram over a large field near the disk center was derived as shown in the bottom right panel of Fig. 5.9. The k-ω diagram for various spectral lines is displayed in Figure 5.9. The ridges are resolved quite well even when the time series only lasts 5-6 hours. This gives confidence that multi-line

oscillation studies to study waves in solar interior and atmosphere can be accomplished with a FPI based design.

5.6 Polarimetery

Polarimetry is an integral part of the SPRING observational requirements. Like many other instruments, as GONG, HMI, MDI etc., adding polarimetry to the spectroscopic measurements needs addition of a polarization modulator optics in the optical path. At least four different states of modulation are needed to derive the full Stokes vector. Thus, dividing the spectroscopic observable into four repeats, one for every unique state of polarization optics (which could be of any type such as liquid crystals), accomplished the observables for polarimetry. The intensity spectra naturally come out of such measurements as Stokes-I parameter, simply by adding all four repeats (all four modulation states). Most importantly the SNR in the velocity measurement is not compromised due to polarimetry, in fact the higher SNR requirements of polarimetry make velocity measurements even more sensitive. Next step is to demodulate the four recorded intensity measurements and derive the Stokes parameters, I, Q, U and V, i.e., the Stokes vector, S=[I,Q,U,V], at each wavelength position.

5.6.1 Choice of Modulator:

The multiwavelength nature of the observations from SPRING would require use of an achromatic modulator or a tunable retarder such as a liquid crystal variable retarder (LCVR). Two LCVRs are needed to perform full Stokes polarimetry. Such modulators are available with very high quality, i.e., good optical quality and uniformity of retardance over the clear aperture. These are available with large clear apertures also, i.e., up to 10 cm clear aperture LCVRs are commercially available. This is more than enough for the FDIS polarimeters. The choice of design is the standard four state modulation used in many imaging polarimeters. The optimum modulation scheme is proposed by del Toro Iniesta & Collados (2000) so that highest possible modulation efficiency can be achieved. Further, for polychromatic application the orientation of the two modulators can be designed such that the demodulation efficiency is optimum for all the wavelengths that will be used with the polarimeter (J. Hou et al. 2013).

5.6.2 Dual Beam Analyzer and Calibration Optics:

For countering seeing induced effects in the polarimetery dual beam analysis technique is very crucial to reach high polarimetric sensitivity and hence high magnetic field sensitivity. This will be accomplished with the polarizing beam splitter analyzing the two orthogonal components of polarization simultaneously with two cameras synchronized with each other.

5.6.3 Note on polarization effects in Fapry Perot interferometers:

Since the oblique ray reflectivity of the coatings is in general polarization dependent, the influence of thin film multilayer coatings of the FPI need to be investigated. Doerr et al. (2008) studied such effects using Jones calculus for telecentric as well as collimated configurations and found that for slow f-ratio (f/128) beams the effect is negligible (10^-5 level) and even for f/28 the effect is small (10^-4 level). This means for collimated arrangement (f# >>128) the polarization effects can be neglected.

Concept 2: Multi-slit Spectrograph based design

Massively Multiplexed Spectrograph (mxSPEC)

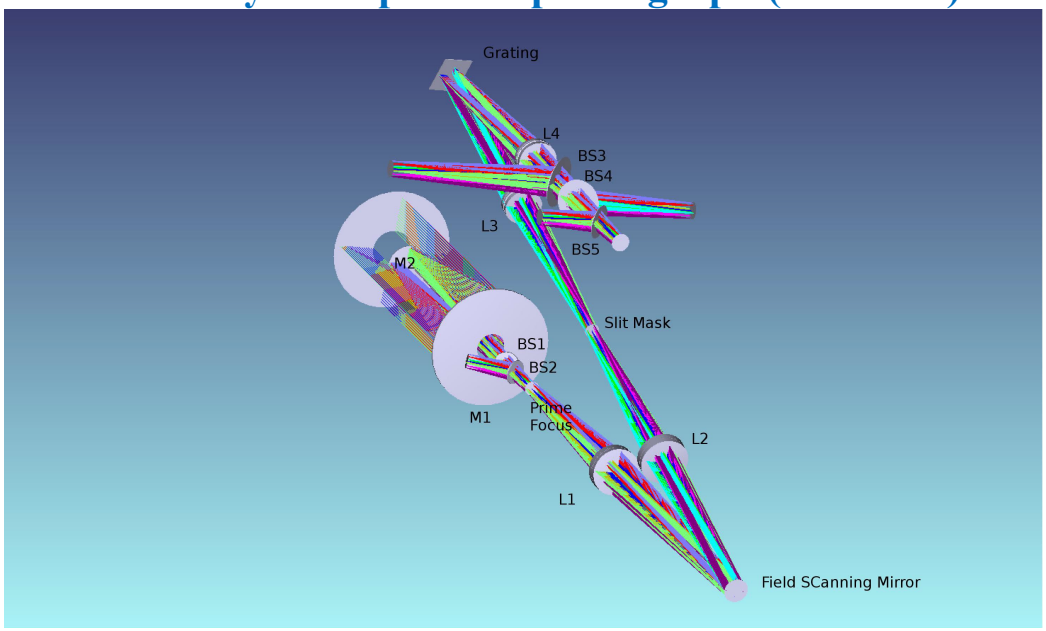

5.7 Multi-channel Spectrograph Concept

Accurate magnetic field measurements of the sun demand a high polarimetric sensitivity and accuracy together with a good spectral resolution. There is a long heritage of such instruments in solar physics designed for long term accurate monitoring of solar magnetism. Some examples relevant for full disk observations are: KPVT spectromagnetograph and SOLIS/VSM at NSO, and SFT at NAOJ. One of the limitations of such slit-scanning full-disk spectropolarimeters is that the time required to acquire a single magnetogram is several tens of minutes. For example, SOLIS/VSM equipped with a 50 cm aperture telescope can obtain a full-disk vector magnetogram in Fe I 630 nm line pair in about 25 minutes. For the chromospheric line Ca II 854 nm the cadence is even longer, ~45 minutes, due to the lower detector response and weaker chromospheric magnetic fields.

To improve the cadence of such instruments, which are limited due to single slit sampling of the solar disk, one must use a multi-channel or multi-slit spectrograph. For example, if SOLIS/VSM was equipped with a multi-slit spectrograph of 50 parallel slits instead of just one, then the observing time per magnetogram would reduce drastically to 30 seconds per photospheric and one minute per chromospheric magnetogram. However, multi-slit designs with large number of slits poses many challenges specially concerning an order-sorting filter and large format high-speed detectors. Further challenges with using a multi-slit methodology is the data reduction and calibration, as the response of each channel is unique. Further, some science studies such as helioseismology require very precise image geometry calibrations. Merging the data from each channel to reconstruct an undistorted solar image is a major challenge with this methodology.

Basically, the concept of a multi-slit spectrograph is quite simple: place regularly spaced multiple slits at the focal plane to sample multiple portions of the field-of-view simultaneously. The spectra corresponding to each slit is displaced by a regular amount depending upon the slit spacing and the angular magnification in the spectrograph. The overlap of the spectra corresponding to the multiple slits is sorted by placing a narrowband interference filter near the multi-slit. The amount of physical spacing between adjacent slits is dictated by the, choice of spectral dispersion, free-spectral-range, and physical size of the detector.

Here we present the conceptual design of a multi-slit spectrograph, mxSPEC, that can provide orders of magnitude improvement in system efficiency using only existing technologies. We discuss how this design will work for SPRING and in order to perform spectropolarimetry and provide high-cadence vector magnetograms in different spectral lines.

5.7.1 Optical Design:

Figure 5.10. below shows the Zemax shaded model of an optical system with up to 45 slits with a 1" spatial resolution over a 0.75 deg field-of-view, covering spectral lines from 500 nm to 1,600 nm simultaneously. The system consists of a telescope, a two-lens image relay and field scanning unit, and a two-lens grating based multi-slit, multi-wavelength spectrograph. The lenses of the image relay system and the spectrographs are an identical air-spaced triplet.

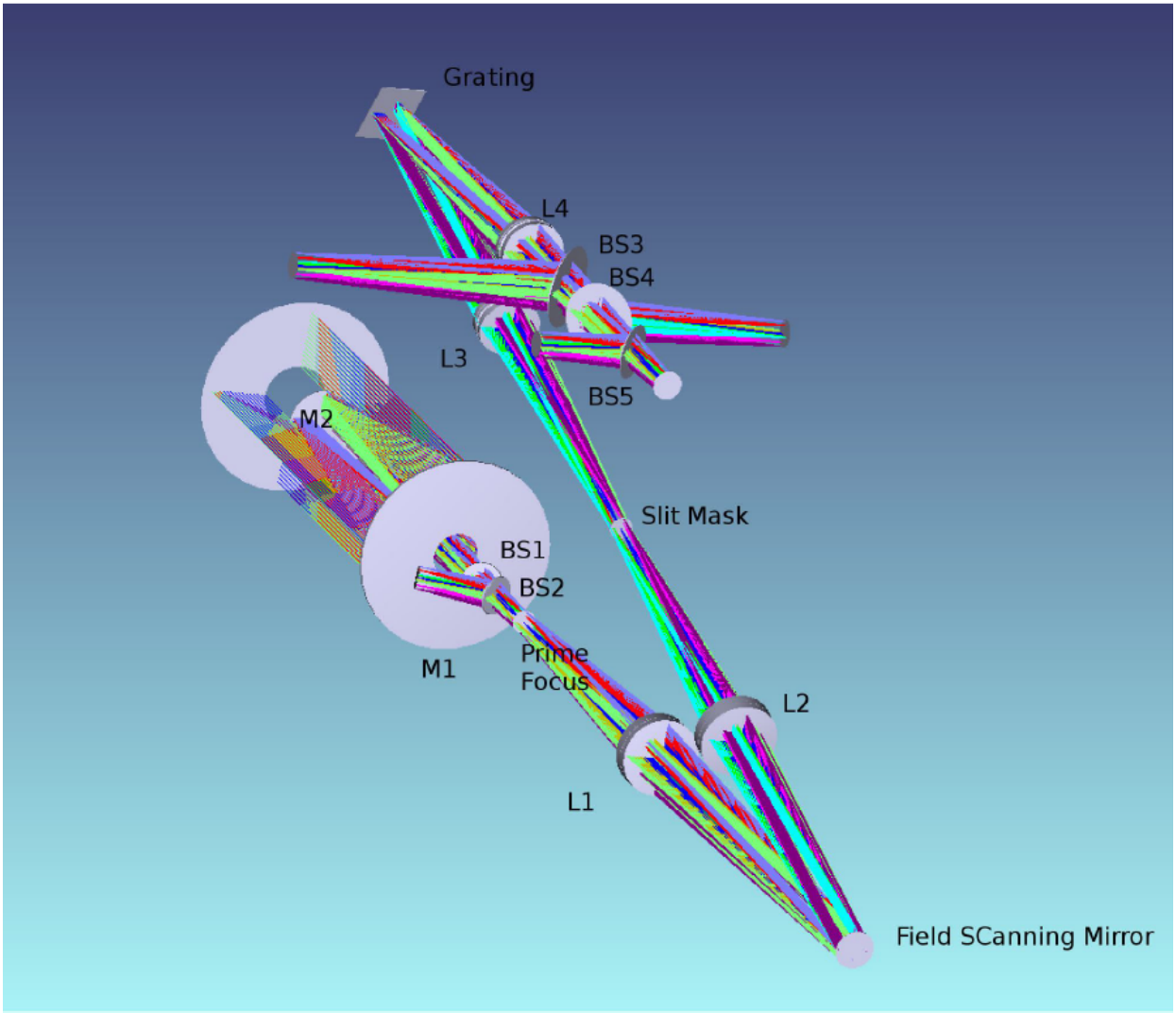

Figure 5.10. Zemax model of a 4-line mxSPEC optical system.

The telescope of this mxSPEC conceptual design is based on a 200 mm aperture, F/11.25 wide-field Ritchey-Chretien telescope. A beam splitter (BS1) before the prime focus diverts 4% of the light to a full-disk image motion sensor (IMS). The

secondary mirror (M2) of the Ritchey-Chretien telescope will be mounted on a fast tip/tilt stage, and using the image motion signals provided by the IMS, will correct for the full-disk image motion induced by atmospheric seeing or instrument platform tracking error. While the Ritchey-Chretien telescope is achromatic, the introduction of the beam splitter introduces a chromatic image shift. A second beam splitter BS2 compensates for the chromatic dispersion and can be used to feed an optional imager to allow for real-time monitoring of the performance of the image motion compensation system. An achromatic 1:1 relay system based on two identical F/5, 100 mm diameter air-spaced triplet lenses transfer the prime focus image to the entrance slit of the spectrograph. The first triplet lens (L1) is placed at one focal length away from the prime focus to collimate the diverging beam from the telescope and form a pupil image 756 mm away. A field scanning mirror (FSM) mounted on a tip/tilt stage is placed at the pupil plane to scan the field across the slit mask. A second triplet lens (L2) mounted at one focal length away from the FSM forms a telecentric image on the entrance slit plane of the spectrograph.

The spectrograph of the mxSPEC conceptual design is based on the same air-spaced triplet lenses used in the relay and field scanning system. The first triplet of the spectrograph (L3) re-collimate the solar image at the slit mask and forms a 2nd pupil of the system one focal length away from L3. A coarsely-ruled, 7.9 line/mm plane reflecting grating blazed at 26.7 deg, placed at the 2nd pupil plane, serves as the dispersing element of the spectrograph. Because of the low groove density of the grating, most of the spectral lines in the visible and near-IR wavelength regimes are diffracted into approximately the same direction with only a small difference in the grating β angles. This can be demonstrated by Table 5.4 which shows the Littrow angle, the diffracting order, and exit slit separation at the focal planes of the spectrograph for four spectral lines commonly used for observation of the chromosphere. Therefore, a single camera lens (L4) and a series of dichroic beam splitters (BS2, BS3, and BS4) can be used to form four separate spectral images of four spectral lines, with the respective bandpass isolation filters placed near the focal planes. The number of spectral lines that can be observed simultaneously
in this system is only limited by the available space between L4 and the final focal planes.

5.7.2 Spatial and Spectral Sampling

The mxSPEC conceptual design was based on a Truesense KAI-20950 6,576 X 4,384 format, 5.5 micron square pixel CCD camera with a 4 fps frame rate. Given the plate scale of the 2,250 mm focal length Ritchey-Cretien telescope, this corresponds to a 0.5"/pixel spatial sampling resolution in the direction parallel to the slit. The field-of-view in the slit direction will be 2,192", or +/- 1.13 R_{sun}. The slit mask of mxSPEC

will have 55 slits with 11 micron slit width separated by 0.55 mm. This will result in a spatial sampling of 1" in the dispersion direction. It will require 50 scan steps to complete a full-field scan. Although the 200mm aperture yields better than 1" diffraction-limited resolution below 800 nm wavelength, the spatial resolution of the instrument is limited by the spatial sampling resolution of the instrument.

Table 5.4. Spectrograph configurations for four chromospheric lines with the incident angle to the grating set to 16.754 deg for the spectrograph of the conceptual of mxSPEC.

Spectral Line	Diffracting	Littrow Angle	Exit Slit Separation
He I D_3 587.6	191	20.000	0.657
Hα 656.3 nm	171	19.996	0.657
Ca II 854.2 nm	131	19.813	0.656
He I 1083.0 nm	103	19.615	0.654

The spectrograph of this conceptual design operates in the inverse configuration (i.e., grating $\alpha < \beta$) with a nominal Littrow angle of 20 deg to take advantage of the rectangular format of the sensor. In this configuration, the nominal separation between the slits is 0.79 mm due to the anamorphic magnification. The CCD will see the spectra from 55 slits simultaneously, with 38 slits covering the sun. The field of view in the direction perpendicular to the slits is 3,640", or +/- 1.88 R_{sun}. Given the spectrograph configuration, the spectral sampling resolution will be ≈100,000, or $\Delta\lambda = \lambda/100{,}000$, with only a weak wavelength dependency. The nominal separation between slits at the spectrograph focus will be 0.66 mm due to the anamorphic magnification of the spectrograph operating in inverse configuration. The resulting free spectral range will be about $\lambda/840$, again with only a weak wavelength dependency.

5.7.3 System Performance Summary, Photon Flux & Sensitivity

Table 5.5 summarizes the instrument characteristics of the conceptual mxSPEC. It should be noted that while the inverse grating configuration provides higher dispersion, it yields lower system efficiency due to partial blocking of the diffracted beam by the grating facets. However, this is not a serious concern since with the 200mm aperture and the design spatial and spectral sampling resolution, the expected photon flux reaching the final focal planes of the conceptual mxSPEC instrument is between 1 to 2 $x10^6$/sec/pixel, assuming a system efficiency of just 1%. This flux far exceeds the photon collecting capability of all the CCDs and visible CMOS cameras that are available to date. In fact, the only camera systems we are aware of with sufficient full well capacity and readout speed are 1) the Virgo 2K IR camera system

with a 100,000 e^- full well capacity and 10 Hz frame rate used for this proof of concept observation, 2) the HAWAII-2RG fast mode camera with 100,000 e^- full well capacity and 64 Hz frame rate, and 3) the HAWAII-4RG-10 camera with 80,000 e^- full well capacity operating at 32 fps. If a HAWAII-4RG-10 camera operating at 32 fps is used for mxSPEC, we can expect to achieve 200:1 signal to noise ratio per spectrum over the entire disk of the sun with less than 2 sec temporal resolution.

Table 5.5. Instrument characteristics of mxSPEC conceptual design assuming a Truesense KAI-20950 CCD operating with a 4 Hz frame rate.

Instrument Characteristics	Value
Spatial Sampling Resolution	1.0" × 0.5"
Field of View	3,640" × 2,192"
Spectral Sampling Resolution	$\approx \lambda/100,000$
Free Spectral Range	$\approx \lambda/840$
Number of Slits	45
Minimum Full Field Scan Time	15 sec
Number of Spectral Lines Observed simultaneously	4

5.7.4 Application for Spectropolarimetry

Although the mxSPEC design demonstrates the massive-multiplexing strategy with a full-disk spectroheliography setup, this strategy obviously can also be easily implemented for spectropolarimetry. The addition of a polarization modulator immediately in front or behind the multi-slit can be easily accomplished without affecting the multi-slit operation. The polarization analyzer however needs to be a dual beam system to avoid seeing induced spurious signals and to make best use of all available photons. This can be done in two ways, (i) using a Savart plate, or (ii) using a polarizing beam splitter (PBS), in front of the detector. In the former case the slit spacing would need to be doubled (i.e., the number of slits would need to be reduced by 50%), to accommodate dual, displaced, orthogonally polarized beams on the same detector, whereas in the latter case two cameras would be needed to image the orthogonal polarized beams. The grating should be selected to be polarization insensitive, i.e., the s- and p- reflectivity of the grating should be of similar magnitude. While a Savart plate has a wide spectral range, the thickness of the calcites and the intermediate half wave plate are wavelength specific. On the other hand, if a PBS is selected then the coatings in the PBS would need to be designed for specific wavelength ranges.

5.7.5 Proof of Concept: Full Disk Setup at the Dunn Solar Telescope

To demonstrate the feasibility of the mxSPEC concept, a simple, proof of concept bench-top 40-slit full-disk spectroheliograph was assembled at the Dunn Solar Telescope (DST) of the National Solar Observatory (NSO) located at Sunspot, New Mexico, for demonstration using the He I 1083 nm line. Figure 5.11 shows the layout of the optical setup. While the DST was designed as a high-resolution solar telescope, its 24-inch diameter exit port No. 2 allows the full-disk light of the sun to pass through unobstructed. A collimating mirror re-collimates the beam to form a 232 mm diameter pupil image at the level of the co-rotating observing floor. The solar beam from a 56 mm sub-aperture of the pupil was then used to feed an achromatic objective lens with 800 mm focal length, which forms a 25.6 mm diameter full-disk solar image. A large iris shutter was placed at the primary focal plane to reduce the field-of-view of the instrument to a circle with a radius of approximately 1.3 solar radius. A 400 mm focal length achromatic doublet lens then re-collimates the solar beam to form a 28 mm pupil on a field scanning mirror. A second 400 mm focal length achromatic doublet lens re-collimates the pupil image to form a telecentric full-disk solar image on the slit mask of the spectrograph. The slit mask (Figure 5.12) was constructed with a photolithographic technology on a 50 mm x 50 mm x 5 mm glass substrate. It has 49 slits of size 45 mm x 0.0125 mm, with separation of 0.750 mm between adjacent slits. With a full disk image size of 25.6 mm, the solar disk is nominally covered by 34 slits. However, at some locations, the sun can be seen simultaneously in 35 slits.

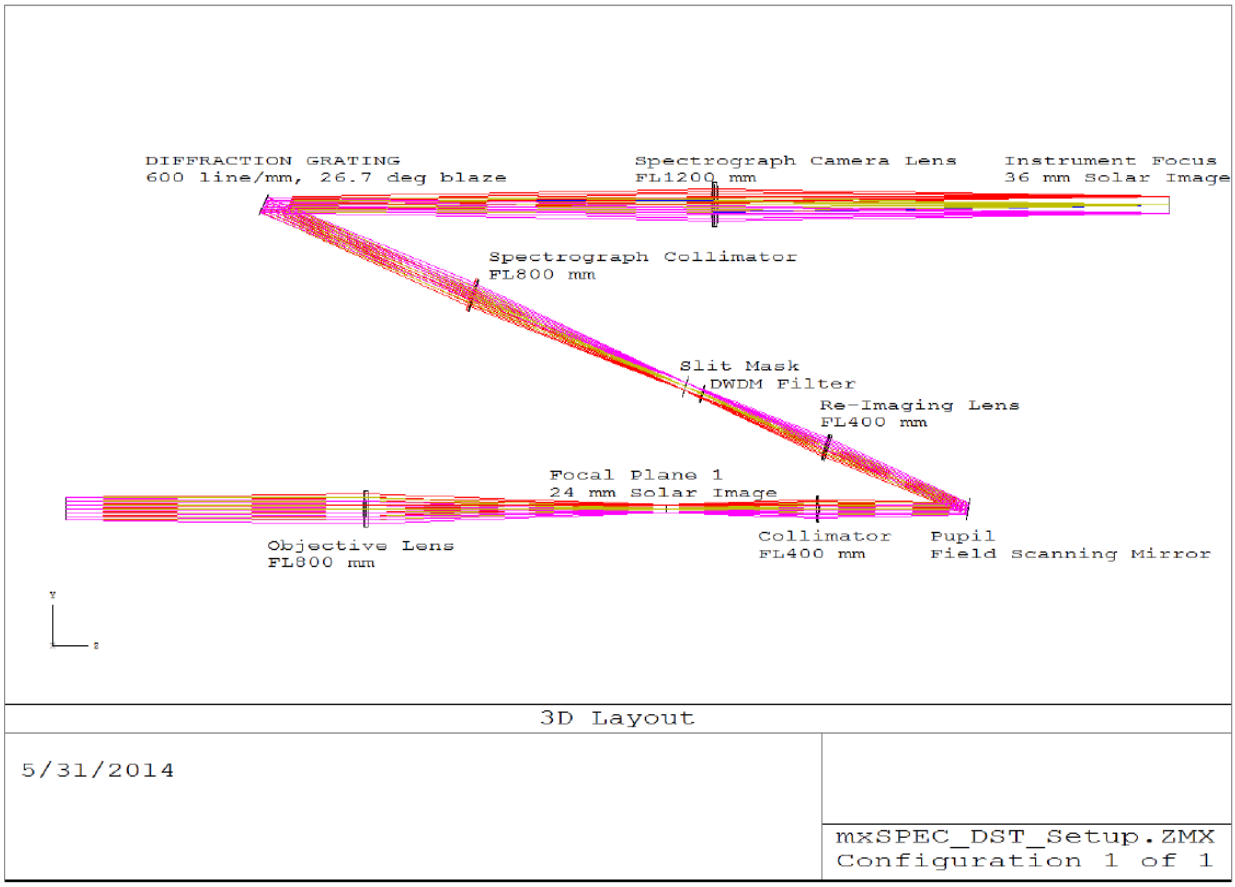

Figure 5.11. Optical Layout of mxSPEC Proof of Concept Spectrograph at the Dunn Solar Telescope

Table 5.6 Instrument Characteristics of the Proof of Concept Setup.

Instrument Characteristics	**Value**
Spatial Sampling Resolution	0.94” × 1.0”
Field of View	2,256” × 2,048”
Spectral Sampling Resolution	27.4 nm/pixel
Free Spectral Range	1.36 nm
Maximum Temporal Resolution	35 sec

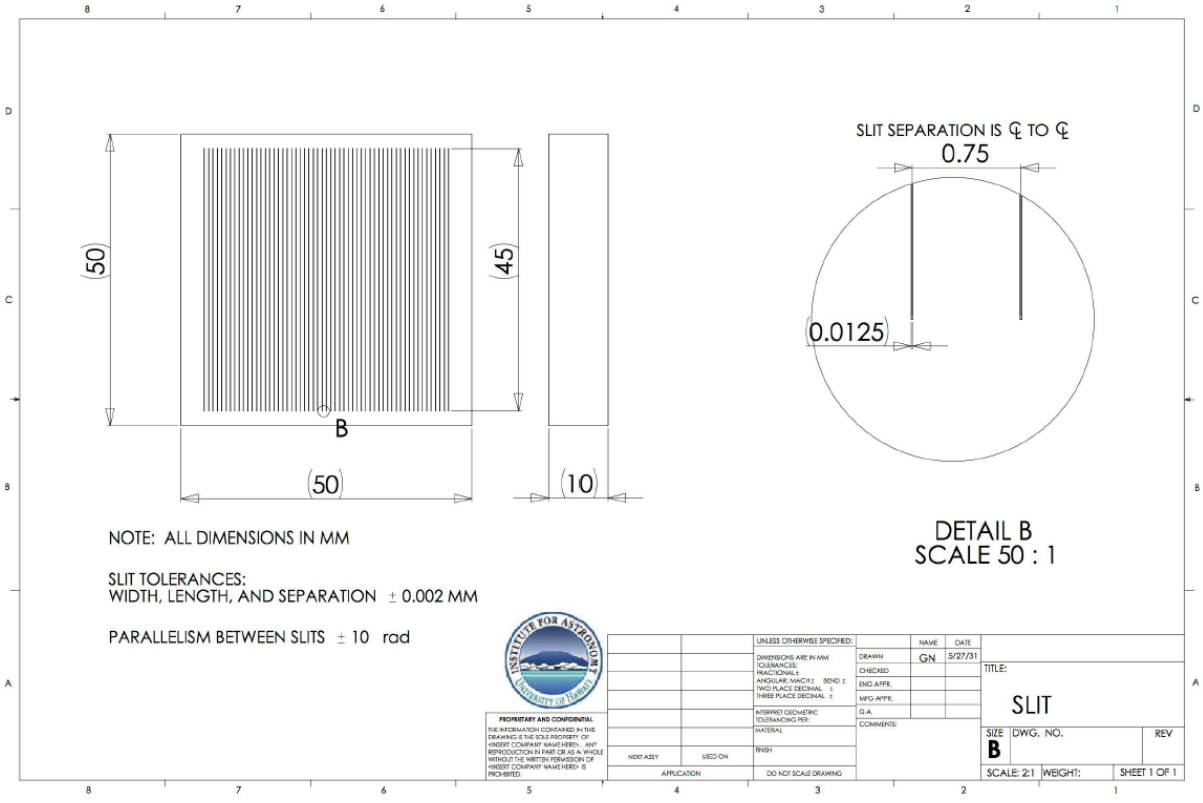

Figure 5.12: A 49-slit mask for mxSPEC Proof of Concept Spectrograph

5.7.6 Spatial Sampling

The slit width of 12.5 μm samples the sun with a 0.94" resolution. The spectrograph consists of an 800 mm focal length collimator, a 1200 mm focal length camera lens, and a 50 mm x 50 mm size 600 line/mm grating with 26.7 deg blaze operating in the first order. The angle between the incident and exit beam is set to 20 deg. The system forms a 38.4 mm image of the whole sun at the spectrograph focal plane. Data were recorded by an IR camera based on an engineering-grade 2048 x 2048 format Raytheon Virgo 2K focal plane array (FPA). With a pixel size of 20μm, the Virgo 2K IR camera samples the sun with a 1"/pixel resolution along the slit direction.

5.7.7 Spectral Sampling Resolution and Free Spectral Range

The 1200 mm focal length camera lens and the 20 deg Littrow angle yield a linear dispersion of 0.73 nm/mm. Therefore the 20 μm pixel of the IR camera samples a 27.4 pm spectral window in the He I 1083 nm spectral window. The 20 deg Littrow angle also introduces a 0.88 anamorphic demagnification which, when combined with the 1:1.5 magnification of the spectrograph, results in a 1.0 mm separation between the slits at the spectrograph focus, and spectra from 40 slits can be recorded simultaneously on the IR camera.

The slit separation of 1.0 mm at the spectrograph focal plane corresponds to a free spectral range of 1.36 nm. A high transmission efficiency bandpass isolation filter with a 1.3 nm -25 dB bandwidth centered at the Si I 1082.7 nm line was placed in front of the slit mask to isolate the spectral windows formed by the multi-slit mask. The band pass isolation filter was fabricated with the Dense Wavelength Division and Multiplexing (DWDM) technology. It has a 0.7 nm -0.5 dB (90%) bandpass and a 1.3 nm -25 dB (0.003%) bandpass.

5.7.8 Flatfield Correction and Sample Spectral Images

A snapshot of the full-disk multi-slit spectra image is shown in Figure 5.13, and Figure 5.14 shows the close-up of the active regions marked by the boxes in Figure 5.13. The multi-slit spectral data were processed with the typical dark and flatfield correction. The flatfield was constructed from a combination of lamp and solar flatfields. The solar flat was obtained by off-pointing the telescope to the four corners of the field of view, and then co-adding 64 exposures with the telescope was commanded to perform an automatic random pointing exercise with a rms amplitude of off-pointing from its nominal position of about 200". This process was repeated at the same pointing offset position with the telescope coude floor rotated 180 deg to reduce the effect of dark spots introduced by the presence of sunspot groups. Due to the weak solar limb darkening function at the 1,000nm wavelength regime, we could obtain a uniformly illuminated image to serve as a flatfield of the instrument. This solar flat can be used to correct for the non-uniform intensity modulation of the instrument along the slits. However, due to the presence and the solar spectral features in the data, this solar flat cannot be used to correct instrumental non-uniformity in the spectral direction. To remove the solar spectral lines from the solar flat, we inserted a Quartz Tungsten Halogen light source before the primary focus of the system and used a lens to generate a diffused light field at the focal plane to serve as a 'spectral flat', i.e., a flatfield without any spectral feature.

While this spectral flat is far from uniformly illuminated in the spatial direction, dividing the solar flat by the spectral flat removes most of the spectral features in the multi-slit spectra, except for the solar and telluric absorption lines. This step creates an intermediate flat with an average solar spectrum but with a spatially non-uniform attenuation. This allowed us to fit and remove the spectral lines in every spectrum individually to create an absorption-line-free spectral flat. The product of this spectral-line-free intermediate flat and the lamp flat is the final flatfield used to correct all the multi-slit spectral images like the one shown in Figure 4.13 The strong absorption lines at the center of each spectral window in Figure 4.13, and more clearly seen in Figure 4.14, are the Si I 1082.7 nm line. Longer wavelengths are to the right, and the persistent weak absorption lines at the right edge of every spectral

windows are due to telluric absorption of O_2 molecules. Strong He I 1083 nm absorption are seen only in spectra from active regions such as those shown in the closeups. While the sampling resolution of 27.4 nm was not sufficient to resolve the two components of He I 1083 nm line, Doppler velocity variations can be seen at different locations in the images.

5.7.9 Temporal Resolution

With a slit width of 12.5 μm and slit separation of 0.75 mm, it requires only 60 scan steps to complete a full-field scan. The Virgo 2K IR camera operates in a continuous readout mode with a frame rate of 10 Hz, and in theory it is possible to obtain the full-disk scan in 6 seconds. However, in this proof of concept observation, the coordination between the field scanning motion and the data acquisition have not been optimized. The system operated in a step-and-stare mode in which the positioning of the field scanning mirror, the acquisition of the data at the scan position, and the storage of the data were executed sequentially. This results in a lower operating efficiency, and it takes approximately 36 seconds to finish a full-field scan. Nevertheless, it is obvious that by optimizing the scan and data acquisition and storage sequence the temporal resolution of the full-field scan can be reduced to 6 sec, limited only by the camera readout speed of 10 Hz.

5.7.10 Sample He I 1083 nm Spectroheliograms

The instrument characteristics of the proof of concept setup at the DST are summarized in Table 5.6. We have obtained a 3-hour long time sequence of full disk He I 1083 nm spectrogroheliogram on February 18, 2014, under good sky conditions. A total of 192 spectral data cubes were obtained. The raw data for each scan is a 2048 x 2048 x 60 format datacube. This data is then re-organized into a 2400 x 2048 x 50 datacube in (x; y; λ) format. The line center position of the Telluric lines at 1083.2 nm in each slit were used to align the spectra in the datacube. Figure 5.16 shows a full disk He I 1083 nm line spectroheliogram constructed from 60 40-slit spectral images in one full-disk scan. The helium spectroheliogram were obtained by integration of a 0.1 nm (4 pixels) spectral window in the rest frame of the Earth. The vertical strips are due to imperfect flatfield calibration.

Nevertheless, playback of the time sequence of the full-disk spectroheliograms reveals the highly dynamic nature of the solar chromosphere, even for areas outside of the active regions. For example, we can notice in a sample time sequence, the activation of a small jet in the active region near the limb. In another location, we notice persistent apparent motion of a filament that can be seen to lift off near the end of the observation. Many prominences, in both active and polar regions latitudes are seen to exhibit highly dynamic motion. While these behaviors of the chromospheric

and coronal features have been observed with high cadence imaging instrument, this is the first instrument that can provide both high cadence imaging and high resolution spectra simultaneously. The high-resolution spectra not only provide information about the Doppler motion, but also thermodynamic properties of the plasma under investigation. These test observations show that multi-slit spectrographs have huge potential.

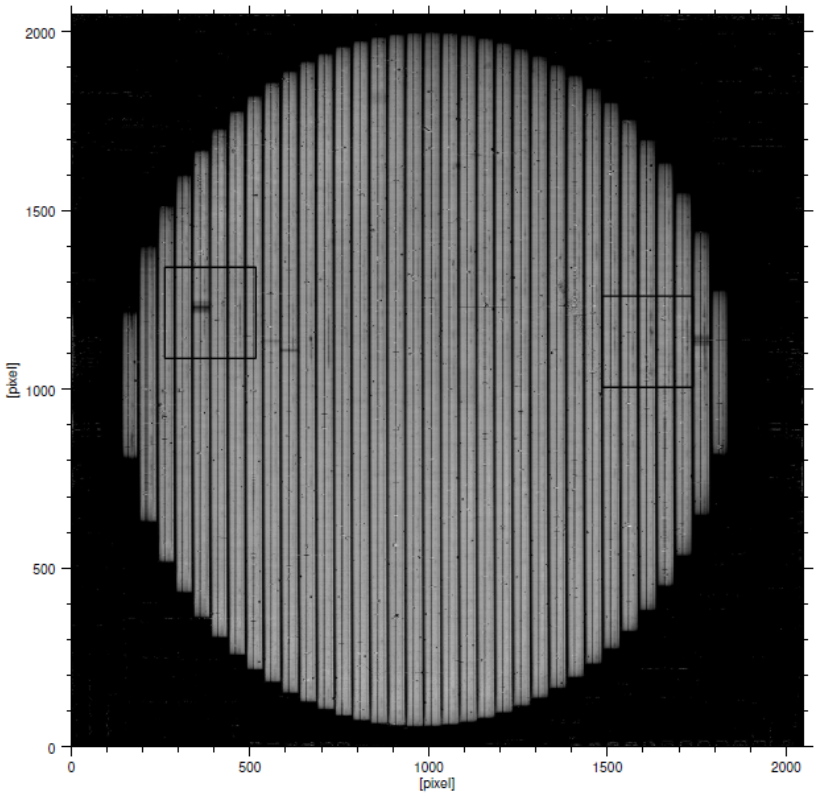

Figure 5.13 Sample 40-slit spectral image with two young active regions. The sun is seen simultaneously in 34 slits. Due to anamorphic demagnification of the spectrograph operating in the normal configuration (when grating $\alpha > \beta$) the solar disk appears to be elongated in the direction along the slits.

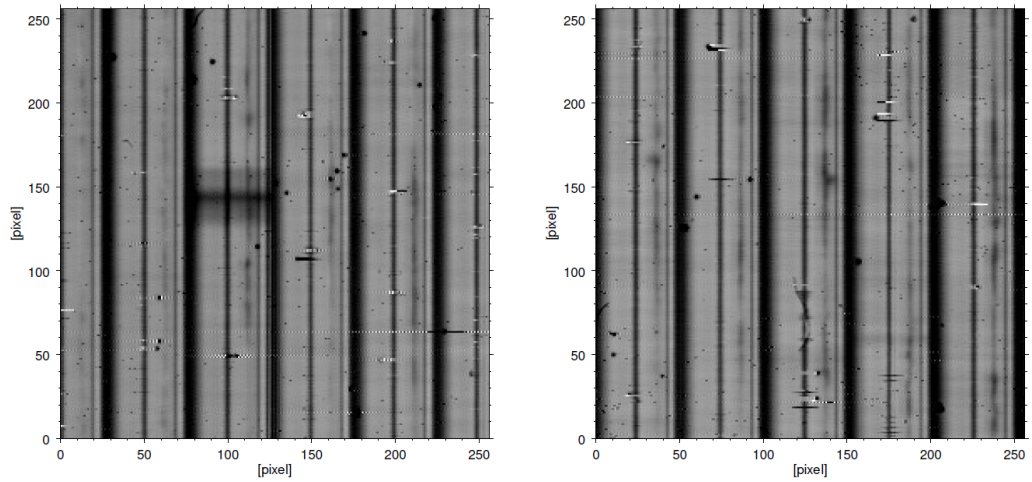

Figure 5.14. Close-ups of the two active regions marked in Figure 5.13. The deep absorption lines at the centre of the bandpass are the absorption of the Si I1082.7 nm line, and the weak lines at the right edge of each slit spectra are a Telluric O2 line. He I 1083 nm absorption appears only in some of the slits. A slice across a sunspot is the dark band in the third slit from the left in left panel.

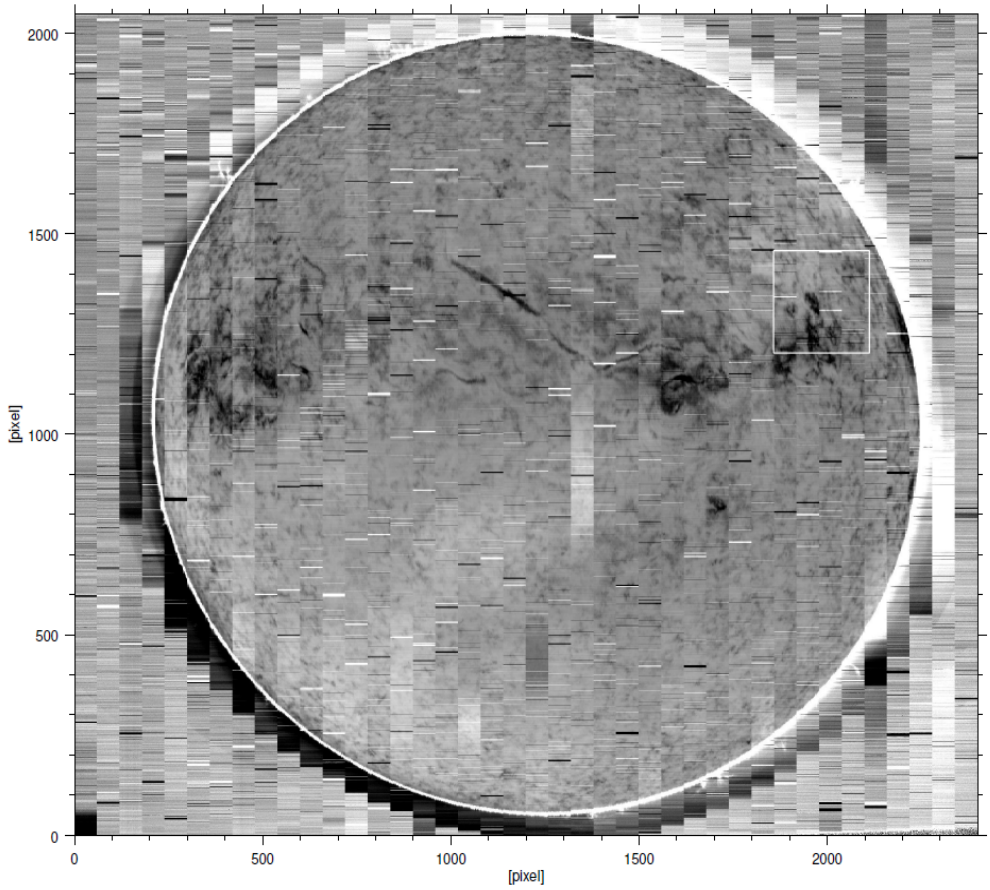

Figure 5.15. Sample mxSPEC He I 1083 nm full disk spectroheliogram normalized by the continuum intensity. The vertical striping were due to imperfect flatfield calibration, and the horizontal lines were due to bad pixels on the focal plane array. A thin bright ring above the limb is due to the He I 1083 nm line emission from the chromospheric fibrils. Prominences can be seen in both active and polar regions.

5.7.11 Summary

The experimental instrument at the Dunn Solar Telescope demonstrates the feasibility and potential of the mxSPEC concept, and it should be obvious that further optimization of the implementation, even with existing technologies, can immediately yield orders of magnitude improvement of our observing capability for helioseismology, dynamics and magnetometry of the sun and its corona. Furthermore, the scale of multiplexing and the improvement of the capabilities of instruments based on the mxSPEC concept will continue to increase with future advancement of high-speed large-format cameras.

Of the many potential applications of the mxSPEC concept, instruments optimized for observations of the line-of-sight velocity oscillations for helioseismic research should prove to be very interesting alternative to the conventional narrow band filter based instrument. Conventional filter based instruments measure the Doppler velocity by measuring the differential intensity of narrow band images obtained at the blue and red wings of a spectral line, and are subject to large velocity error for regions with high velocity along the line of sight direction.

Observations of the full spectral line profiles with high spectral resolution over a large spectral window by an instrument based on the mxSPEC concept can provide very accurate velocity measurement even for areas with high velocity. Furthermore, the large spectral window coverage of instrument of the design can capture highly dynamic events in which very high line of sight velocity shifts spectral lines outside the spectral window of narrow bandpass imaging instrument.

The mxSPEC concept also allows for the implementation of a laser comb or other stable wavelength reference to provide an absolute velocity reference, thereby achieving velocity accuracy that cannot be attained with conventional filter based systems. The possibility to observe multiple spectral lines simultaneously through the same optical system further provides a very efficient way to study the propagation of waves through the solar atmosphere. We will first further analyze the February 18, 2014 Helium data to derive the Doppler velocity of the Si I 1082.7 nm and He I 1083.0 nm lines to further evaluate capability of the mxSPEC concept for the dynamics of the chromosphere. We also plan to optimize the operational efficiency of the proof of concept instrument to improve its temporal resolution and to further evaluate the potential of mxSPEC for high precision Doppler velocity measurements for helioseisomology research.

SPRING multi-line study with mXSPEC: Similar to mxSPEC presented here, one will need to design three channels, mxSPEC-B (Blue channel: for lines in 370-550nm range), mxSPEC-R (Red channel: for lines in 550-800 nm range), and mxSPEC-IR (infrared channel: for lines in 800-1600nm range, as presented here). These will provide an alternative design (to FDIS channels) to achieve SPRING goal of multiline measurements.

6. STUDY OF THE DUTY CYCLE AND SEEING CONDITIONS AT THE GONG SITES

We have carried out an extensive study of the duty cycle and the seeing conditions at the currently existing observing sites of the Global Oscillations Network Group (GONG). This study includes data measured at all six GONG sites in the years 2013 and 2014. These sites have been selected as baseline for the proposed SPRING network since they have proven to enable high-quality solar observations with a very high duty-cycle. The goal of this study is to find out if these sites can fulfill the scientific requirements for SPRING. Of course, one has to keep in mind that GONG had more relaxed science goals than SPRING and therefore, many quality requirements of the GONG sites (e.g. the housing of the telescopes) will be higher for SPRING.

The six sites of GONG are: Big Bear, California; Mauna Loa, Hawaii; Learmonth, Australia; Udaipur, India; El Teide, Canary Islands, Spain; and Cerro Tololo, Chile. The instrumentation and telescope housing at the six sites are essentially identical. They all acquire full disk images of the sun in several passbands with relatively low resolution (1 pixel corresponds to 2.5 arcsec). The telescope apertures are approximately 1.5 meters above the ground which is well within the turbulent ground layer (<10 m). Therefore, one can expect that the local seeing is affected by the surroundings of each telescope, and the heating of the ground by the Sun can be expected to have significant influence on seeing conditions during the day

6.1 Observing Statistics and Duty Cycle

Synoptic observations of the Sun require a duty cycle as high as possible. Gaps in the observed time series (e.g. caused by the day-night-cycle, bad weather, or technical issues) can lead to spurious frequencies when looking at the Fourier domain and transitional solar events can be missed when observations are not available. These are the main reasons why we need to observe the Sun from a number of sites around the world.

We studied the conditions at the six GONG sites in the years 2013 and 2014. The results are presented in Figure 6.1. This figure displays the percentage of successful observing time compared to the theoretically possible observing time of the Sun for each site separately. Additionally, the overall duty cycle for the combined network is displayed a thick red line. It can be seen that although the individual variations of successful observing time of each site from month to month are rather large, the overall duty cycle remains at about 90 % throughout the year. Such a high percentage is essential for successful compliance with the science requirements defined in this document. The low observation rate of some sites during some months (e.g. Udaipur from July to September 2013) are due to technical issues at the site. Still, even during such periods, the duty cycle stays at 90 % due to the presence of the five other sites.

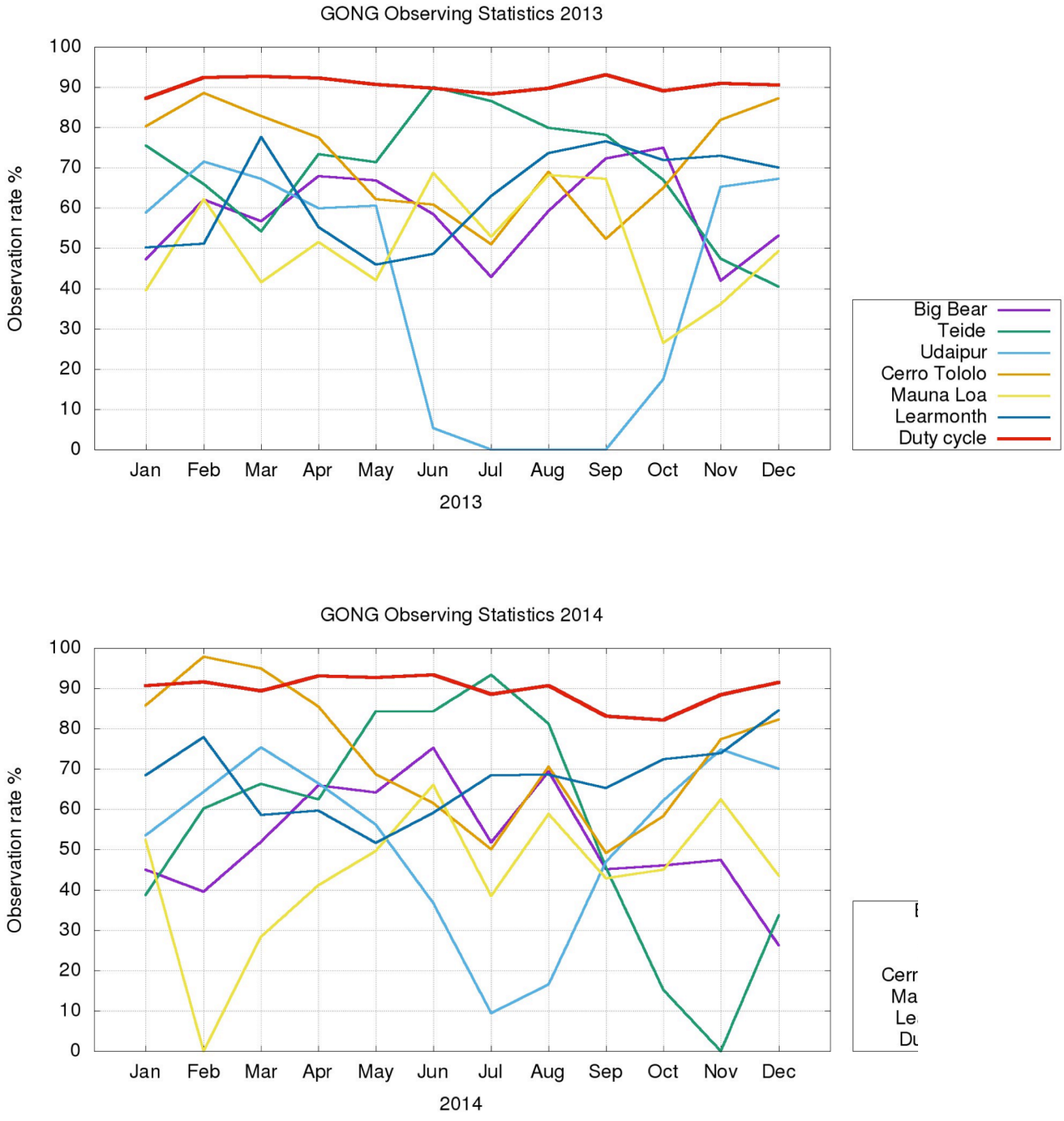

Figure 6.1: Duty cycle (red) and percentage of possible observing time for the six GONG sites for the years 2013 and 2014.

6.1.1 Previous Studies of Seeing at GONG Sites

A study of the seeing-quality at the GONG sites has been carried out for pre-1999 data by Bell et al. (Solar Physics, 185, 15, 1999), hereinafter referred to as Bell (1999). At that time, a 256 x 256 CCD had been used which resulted in a pixel size of 8 x 10 arc sec. By computing a modulation transfer function (MTF) through Hankel transforms using the complete limb of the Sun, the radius of the Sun could be measured to about 0.01 pixels or 0.1 arc sec. Bell (1999) analyzed the seeing quality using the MTFs of the years 1995/96 (details can be found in Bell (1999)). Their investigation revealed that the seeing at all sites typically lies between 2.5 and 10 arc sec with a strong variation during the day.

6.1.2 Data and Analysis Methods

We carried out a similar study based on the method described by Bell (1999), but for more recent GONG data from upgraded CCDs. The currently installed CCDs have a size of 1024 x 1024 pixels which results in a resolution of 2.4 arc sec per pixel for a solar image which is 750 pixels wide. The MTFs are automatically computed every minute from averaged exposures with the GONG pipeline and are used to correct for the distortion of the solar image. We used the MTFs of the years 2013 and 2014 of all six GONG sites for our analysis of seeing quality.

The smaller pixel size of the CCDs compared to the pre-1999 data enabled us to measure the position of the solar limb to an improved precision of about 0.025 arc sec, and therefore also to determine the seeing with similar precision. For the latter, we used a model that describes the shape of the MTF as a function of seeing or atmospheric turbulence. Bell (1999) developed such a model based on the theory of atmospheric turbulence and seeing, which we used in our study to fit the observed MTFs with modeled MTFs as a function of the Fried parameter r_0. The parameter r_0 (Fried, Proc. IEEE 55, 57, 1967) is the length scale over which the wavefront varies by 1 radian² and can be translated to angular resolution (or seeing) by using

$\alpha = (206265/0.91)\frac{\lambda}{r_0}$(Korff, J. Opt. Soc. Am. 63, 971, 1973)

where alpha is the angular resolution in arc sec and lambda is the wavelength. For our data this can be written as $\alpha = \frac{15.34}{r_0[cm]}$. Following Bell1999 we use the following expression for modeling the amplitude B(f) of the MTF at a spatial frequency f:

$B(f) = \mathrm{e}^{-3.35(\lambda f/r_0)^n}$.

We neglected light scattering in our fitting expression since Bell (1999) had showed that fitting only the linear part of the MTF yields the same result compared to fitting the complete MTF with a scattering term.

6.1.3 Results of the Seeing Study

Our study shows significant differences in the seeing quality of the different sites. Variations of the seeing during the year are not very prominent but diurnal changes of the seeing dominate. This is caused by the heating of the air around the telescope sites which produces a shallow turbulent layer. This layer usually has a depth of a few tens of meters and can be avoided by putting the telescope onto a tower which is normally done for large solar telescopes such as the VTT on Teneriffa.

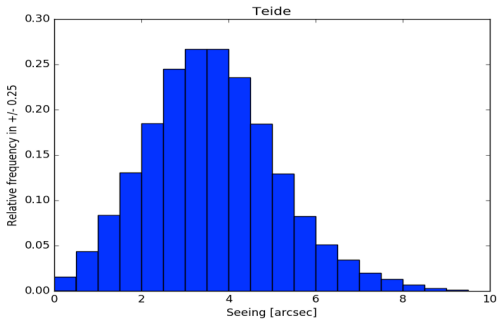

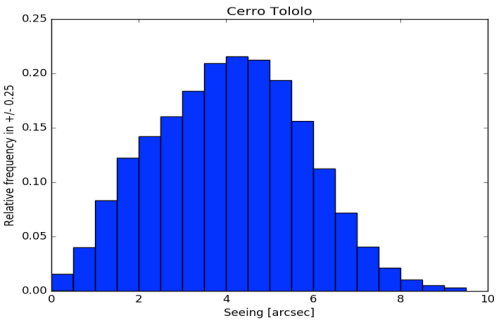

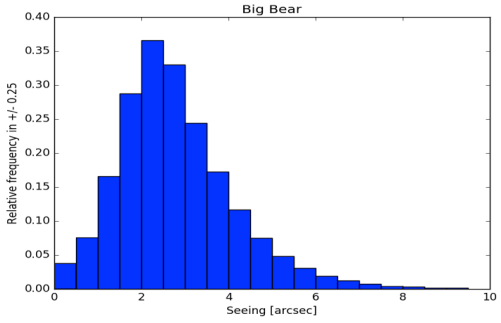

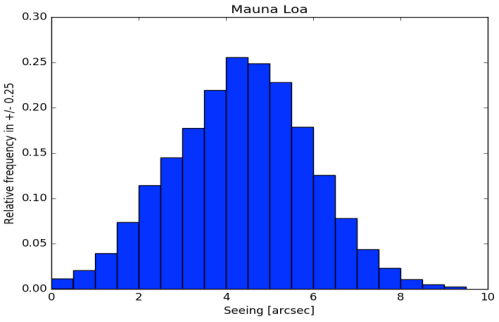

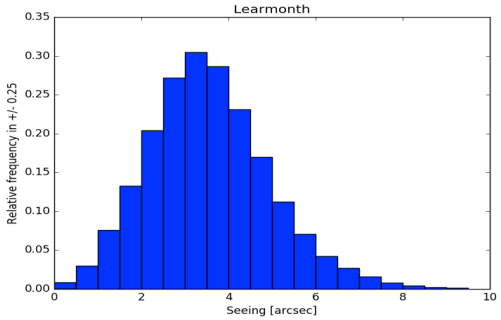

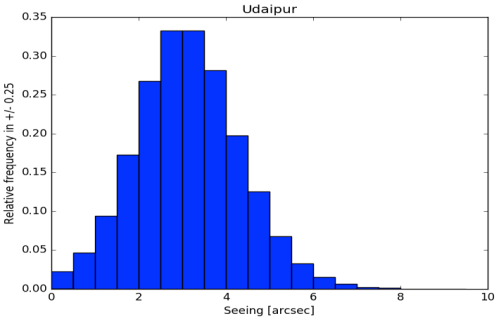

Figure 6.2: Distribution of the seeing for the six GONG sites in the year 2014.

For all six GONG sites, the seeing typically lies between 1 and 10 arc sec, but there are significant differences between the sites, which are summarized in Table 6.1. The two observatories, Big Bear and Udaipur, which are located directly at a lake have the best seeing on average of the network. The close water stabilizes the air of the low atmospheric layers close above the ground.

Site	**Average seeing in 2013 in arc sec**	**Average seeing in 2014 in arc sec**
Teide	3.8 ± 1.7	3.6 ± 1.5
Cerro Tololo	4.2 ± 1.6	4.1 ± 1.6
Big Bear	2.7 ± 1.6	2.8 ± 1.4
Mauna Loa	4.4 ± 1.6	4.4 ± 1.6
Learmonth	3.6 ± 1.4	3.6 ± 1.4
Udaipur	3.2 ± 1.2	3.1 ± 1.2

Table 6.1: Average seeing at the GONG sites in 2013 and 2014.

When we look at the seeing during the day as a function of the altitude of the Sun, we see that there is a dependence of the seeing with the time of day respectively the altitude of the Sun. Figure 6.3 shows the measured seeing for Cerro Tololo and Big Bear for a complete month. The color represents the azimuth of the Sun. E.g. for Cerro Tololo, the seeing in the morning (solar azimuth at around 90) is significantly lower than in the afternoon (azimuth around 270). For Big Bear, such a dependence is not as pronounced.

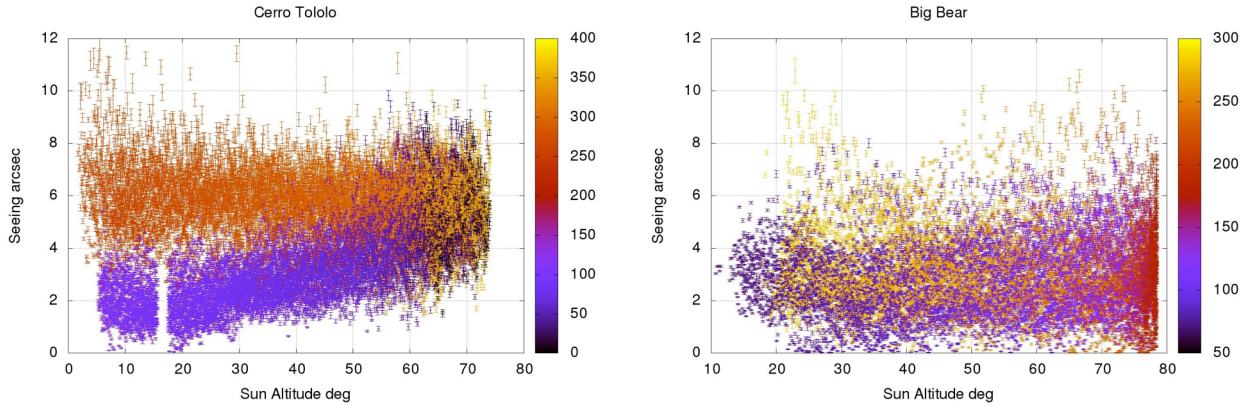

Figure 6.3: Seeing as a function of the Sun's altitude above the horizon. The Sun's azimuth is color-coded. Data are from May 2014.

Figure 6.4 shows the same parameters as Figure 6.3 but smoothed with a running mean. All six sites show similar behavior, only for Teide and Cerro Tololo the variation throughout the day is more pronounced. The data from other months in 2013 and 2014 show a similar trend.

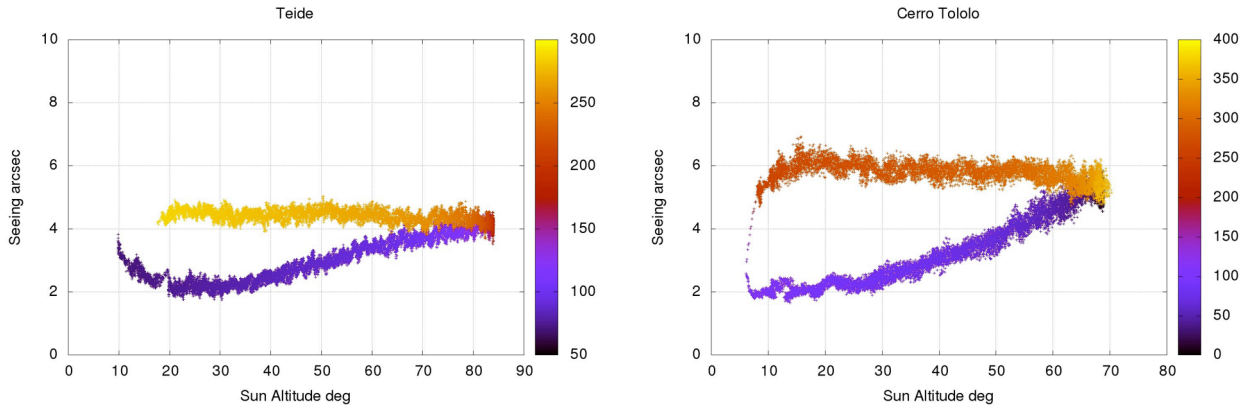

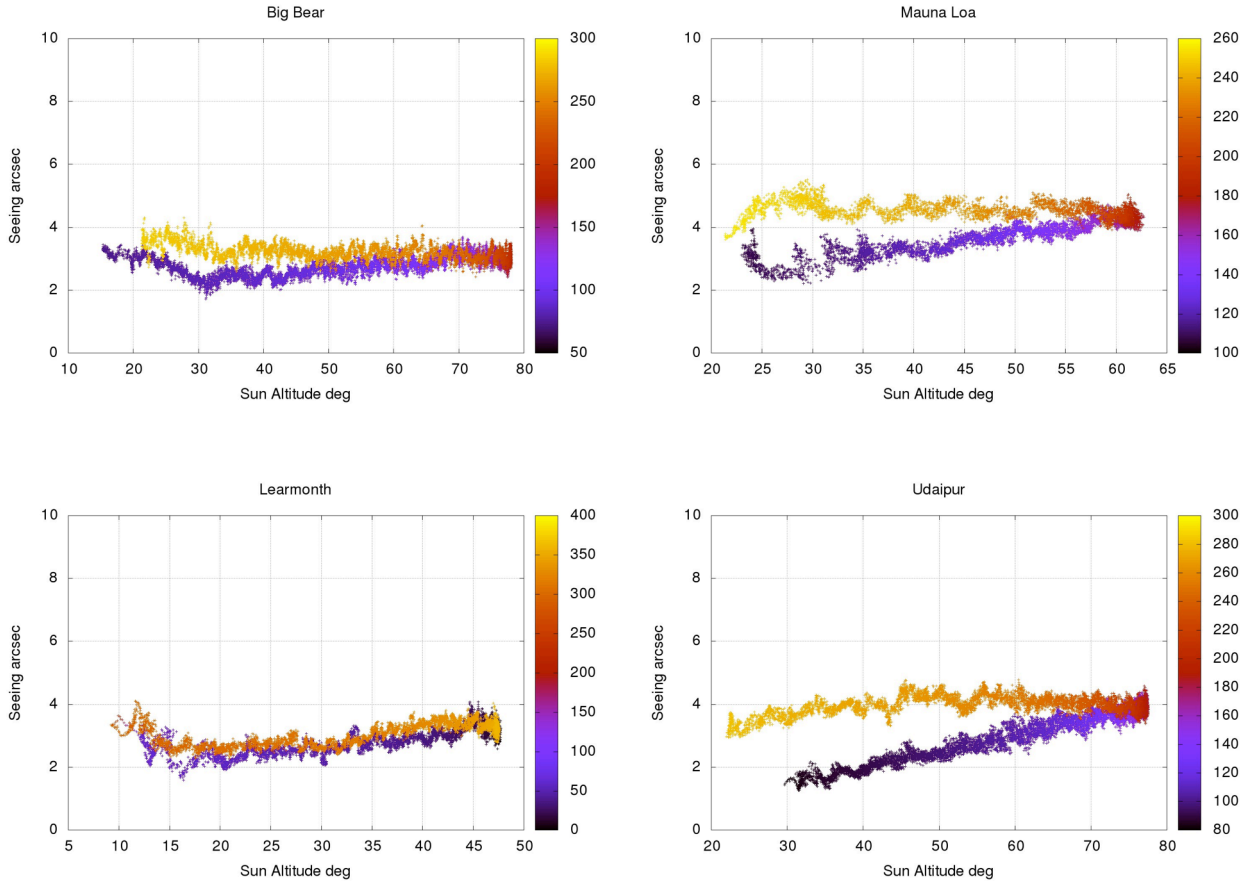

Figure 6.4: Running mean of the seeing as a function of the Sun's altitude above the horizon. The Sun's azimuth is color-coded. Data from May 2014.

The effect of seeing on the acquired images of the Sun is displayed in Figures 5 and 6. The respective seeing values were determined in this study. With a seeing of 2.5" in the leftmost frame of Figure 6.5, fine structures such as granulation are visible. These fine structures are washed out when seeing degrades. The images are averaged over one minute of observation.

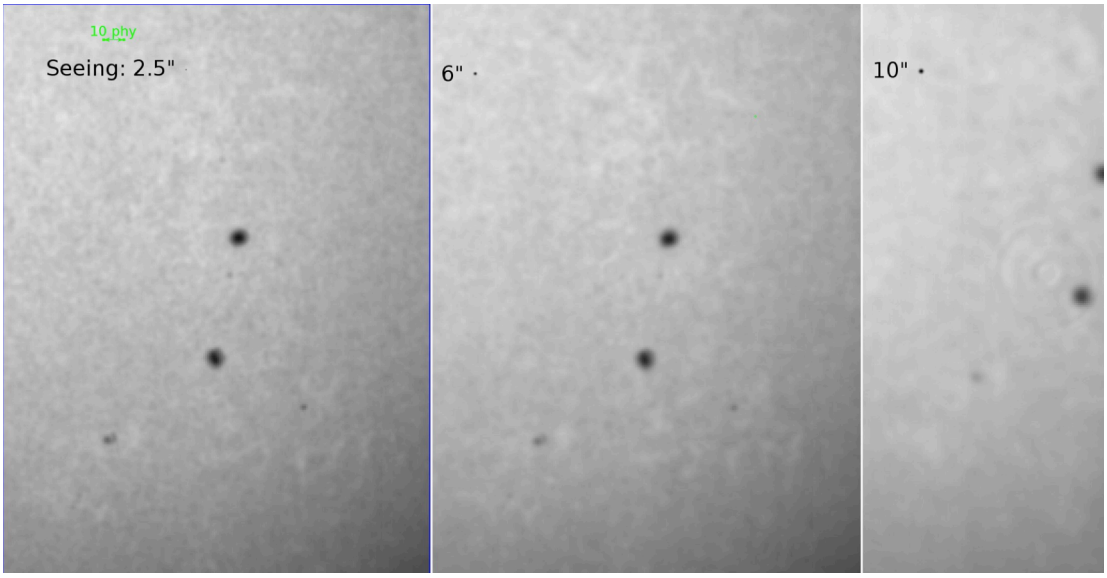

Figure 6.5:Detail of the Sun close to the center of the visible disk at different instances during the same day. From left to right with a seeing of 2.5, 6, and 10 arc sec. Granulation is visible in the leftmost frame. (Images from GONG, El Teide, January 7, 2013)

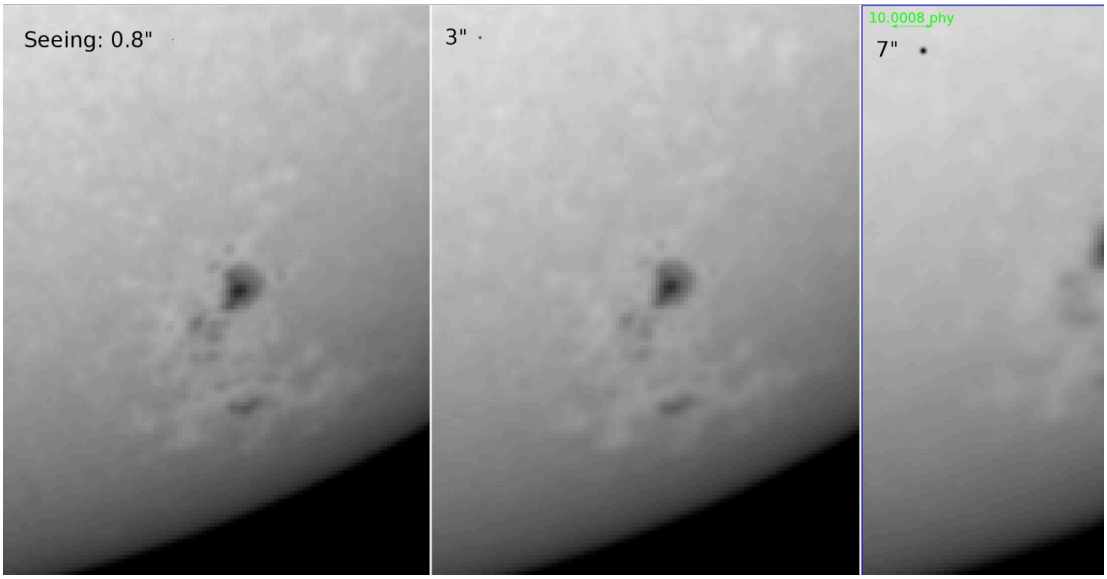

Figure 6.6: Detail of the Sun close to the limb at different instances during the same day. From left to right with a seeing of 0.8, 3, and 7 arc sec. (Images from GONG, El Teide, January 6, 2013)

According to our study, a seeing better than 1” can only be achieved for short periods

of time at all six GONG sites. It is known that putting a telescope higher above the ground will improve the seeing conditions. Especially the diurnal variations which are caused by the heating of the ground through solar radiation can be avoided or at least reduced.

7. ESTIMATION OF THE EXPECTED DATA RATE OF SPRING

We describe here the expected data rates for one node of the network which follow from the Scientific Requirement Document (SRD).

Combining the science requirements defined in Section 3 of the SRD we arrive at the following specifications: The Sun has to be observed in full-disk mode with a spatial resolution of 1 arc second and a temporal cadence of 10 s in photospheric velocity and intensity as well as in the line-of-sight magnetic field and the full-vector magnetic field. Five spectral lines should be observed with the same temporal cadence at 20 wavelength-bins per line. For a full-disk image of the Sun, a resolution of 1 arc sec can be achieved with a 2048 x 2048 pixel² CCD.

Specifications of the expected observations:

- 2k x 2k camera, 16 bits
- Five spectral lines
- 20 wavelength bins per spectral line
- Cadence: 10 sec
- Full Stokes vector (=4 components)

Estimation of the expected data rate:

- Size of one image uncompressed: 2048² x (16/ 8) = 8388608 Bytes = 8 MB
- Number of images per cycle (=10 sec): 5 x 20 x 4 = 400
- Data rate per cycle: 8 MB x 400 = 3 200 MB = 3.1 GB
- Expected data rate: **18.7 GB/minute**
- After data compression (gzip): **~10 GB per minute** or **~7 TB per day (assuming 12 hours of data)**

A data rate of 10 GB per minute or 7 TB per day is high but can be handled with

existing hardware.

In 2013 and 2014, the per-site duty cycle at the GONG sites has been on average between 40 and 90 %. For a mean value of 65% duty-cycle per site, the daily mean observation time is approximately 8 hours. This would result on average in 4.5 TB of compressed raw data per day and per site.

A connection with a speed of 1 GB/s can transfer a maximum of ~10 TB per day which would be sufficient to transfer the raw data from an observing site to a Data Centre, where further data processing would be carried o

Even when transferring all raw data to a Data Centre, it is necessary to provide sufficient data storage on-site to prevent data loss during network failures. Such storage must be of sufficient capacity to store the data of several weeks. A storage buffer for 10 weeks of acquired raw data needs to have a capacity of 70 x 7 TB = 490 TB of storage at each of the six observing sites.

8. ONLINE CLOUD DETECTION IN SOLAR FULL-DISC WHITE-LIGHT IMAGES

8.1 Introduction

Ground-based solar observations can be significantly affected by clouds. The shadows of clouds decrease the brightness of parts of the solar disc and sometimes obscure them completely. For automated routine synoptic observations, there is a need to detect the presence of cloud shadows and to evaluate how strong their effect is. For this purpose, it is useful to define four degrees of the image degradation by clouds (a *cloud score*):

0 – Clean Sun (Fig. 8.1a), no clouds; the images can be used for automatic solar activity detection.
1 – Weak clouds (Fig. 8.1b); the images cannot be used for automatic detection but they are still useful.
3 – Strong clouds (Fig. 8.1c, d); the images are severely affected and it is not worth to store them.
4 – No Sun; the solar disc is completely obscured by clouds.
Feng et al. (2014) published a method of automatic detection of cloud shadows and their removal in full-disc images, based on a comparison of observed images with a reference one. The method, which requires a centering of the full-disc image and an analysis of its radial profiles, is computationally expensive and it is intended mostly for a post-processing.
We present a method that analyses each observed image individually and does not need a reference frame or a cross-comparison between the images. This makes it possible to determine the cloud score immediately after taking the image and to decide about its further processing.

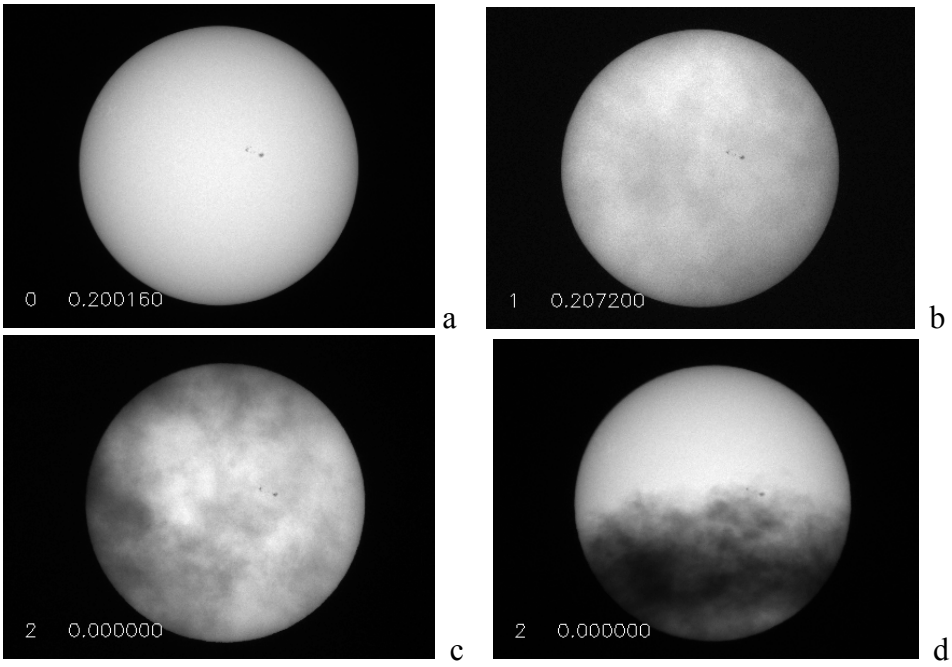

Figure 8. Examples of the cloud effects: a - clean Sun; b - weak clouds; c, d - strong clouds.

8.2 Data Sets

To elaborate the method, we used several data sets of white-light images obtained by the Ondřejov D = 50 mm, f = 500 mm full-disc patrol telescope with a wavelength band width of 7 nm centered at 536 nm. The 8-bit images are 1600 x 1200 pixels large and the image scale is 1.83"/pixel. Six data sets include periods of clean Sun, weak cirrus clouds, and other clouds with different transmissivity. Two long data sets with 1010 and 2270 frames cover periods with variable cloudiness.

8.3 Criteria

Minimum brightness – this criterion checks if the brightness signal is sufficient for further evaluation. Its value, *maxdark*, is set well above the dark noise, in the case of 8-bit data to 10. If the observed intensity maximum I_{max} is smaller than *maxdark*, the Sun is completely obscured by clouds and no further evaluation is made.

Criterion 1 – A ratio of average intensities of the solar disc and of the rest of frame.

$$crit1 = \text{mean}\,(I_{disc}) \,/\, \text{mean}\,(I_{non\text{-}disc}) \qquad (1)$$

The pixels belonging to the solar disc are separated from the non-disc pixels by the threshold intensity 0.2 I_{max}. This threshold is based on the theoretical center-to-limb variation curve.

The criterion, a contrast of the solar disc to its surroundings, is independent of image scale but it depends on number of bits per data pixel. Due to the scattered light, it may slightly depend on the field of view, i.e., on the number of non-disc pixels. In our data, the area covered by the disc is 43.7 % of the full FOV.

For a correct exposure time, when nearly the whole dynamical range of intensities is used, and for clean Sun conditions, the intensity ratio is 50–51 in our 8-bit data.

The typical values of Criterion 1 in 8-bit data are as follows:

crit1 = 0 ... is set for too dark images, $I_{max} <$ *maxdark*, no Sun
crit1 = 20 ... is the minimum value for using Criteria 2 and 3; 0 < *crit1* < 20 means strong clouds
crit1 = 40 ... is the minimum value for a clean Sun (it depends on exposure time and Sun elevation)
crit1 = 50 ... is typical for a clean Sun

These values have to be determined experimentally.

Criterion 2 – A ratio of observed and calculated disc areas. It is applied only when *crit1* > 20.

$$\begin{aligned} crit2 &= N_{pix\_obs} \,/\, N_{pix\_calc} && \text{for } crit1 \geq 20 \\ crit2 &= 0 && \text{for } crit1 < 20. \end{aligned} \qquad (2)$$

Here, N_{pix_obs} is a number of pixels brighter than 0.2 I_{max} (disc pixels) and $N_{pix\_calc} = \pi(r\odot /scale)^2$ is the calculated disc area depending on the image scale and the apparent angular solar radius $r\odot$, calculated by an ephemeris program for the date of observation.

When *crit2* < 1, a part of the solar disc is covered by a strong cloud (Fig. 1d). If *crit2* = 1 ± 0.01, the full disc is seen and the necessary condition for clean Sun or weak clouds is met.

Criterion 3 – A normalized standard deviation of the full-disc intensity. Applied only when *crit2* ≈ 1.

First, the full-disc image is smoothed by a boxcar of 0.5'x 0.5' to remove random noise and diminish the effect of sunspot groups and plages. Then the standard deviation of disc intensities is calculated and divided by their mean value.

$$crit3 = \text{stdev}\,(I_{disc\_smoothed}) \,/\, \text{mean}\,(I_{disc\_smoothed}) \qquad (3)$$

The value of *crit3* is given by the center-to-limb variation and its perturbation by clouds. The unperturbed value is close to 0.205 (clean Sun) and for weak clouds it ranges between the limits 0.18–0.22. Values out of this range correspond to strong clouds (Fig. 1c). This criterion is used to distinguish between the clean-Sun conditions (in the range 0.199–0.202), weak clouds (in the range 0.18–0.22), and strong clouds. These values have to be determined experimentally.

8.4 Cloud Score

The cloud score is obtained by a combination of conditions derived from the criteria described above:

Condition for minimum brightness	$cr0 = 1$	for $I_{max} > maxdark$	else $cr0 = 0$
Condition for clean Sun	$cr1 = 1$	for $crit1 > 40$	else $cr1 = 0$
Condition for clean Sun or weak clouds	$cr2 = 1$	for $crit2 \approx 1$	else $cr2 = 0$
Condition for clean Sun	$cr31 = 1$	for $crit3 \approx 0.205$	else $cr31 = 0$
Condition for weak clouds	$cr32 = 1$	for $0.18 < crit3 < 0.22$	else $cr32 = 0$

The combination of conditions corresponding to individual cloud scores is shown in Table 1.

Cloud score	*cr0*	*cr1*	*cr2*	*cr31*	*cr32*
0 – clean Sun	1	1	1	1	1
1 – weak clouds	1	0	1	1	1
1 – weak clouds	1	0 or 1	1	0	1
2 – strong clouds	1	0 or 1	1	0	0
2 – strong clouds	1	0 or 1	0	n/a	n/a
3 – no Sun	0	n/a	n/a	n/a	n/a

Table 8.1: Cloud score and the corresponding combination of conditions. Filled cells show the decisive conditions for cloud scores 1–3.

8.5 Results

The criteria, conditions, and their relations were included in the CLOUD_TEST routine written in the IDL language (see Appendix for the source code). The code, running on an ordinary PC, analyzes 35 frames per second when the frames are stored on a local disc and 15 fps if they are transferred by a local network. This is sufficient for online processing. Three data sets, 130528 (161 frames), 130608 (1010 frames), and 130613 (2273 frames), covering periods of clean Sun, weak clouds, strong clouds, and the totally obscured Sun, were used to check the performance of the method. Plots of *crit1*, *crit2*, and *crit3*, together with the cloud score, are shown in Fig. 8.2 for the three data sets.

The results were compared with the visual assessment of processed images. The errors occur mainly at subtle transitions between the clean Sun and weak clouds and between the weak and strong clouds. The decisive criterion is *crit3*, which is the weakest of the criteria due to the fact that the clouds may both increase and decrease the normalized standard deviation of disc intensities. These changes may compensate each other in some cases. In the test runs, 3.3 % of weak-cloud frames were classified erroneously as a clean Sun and 2.7 % of strong-cloud images as weak clouds. These plausible results show that the suggested method might be useful.

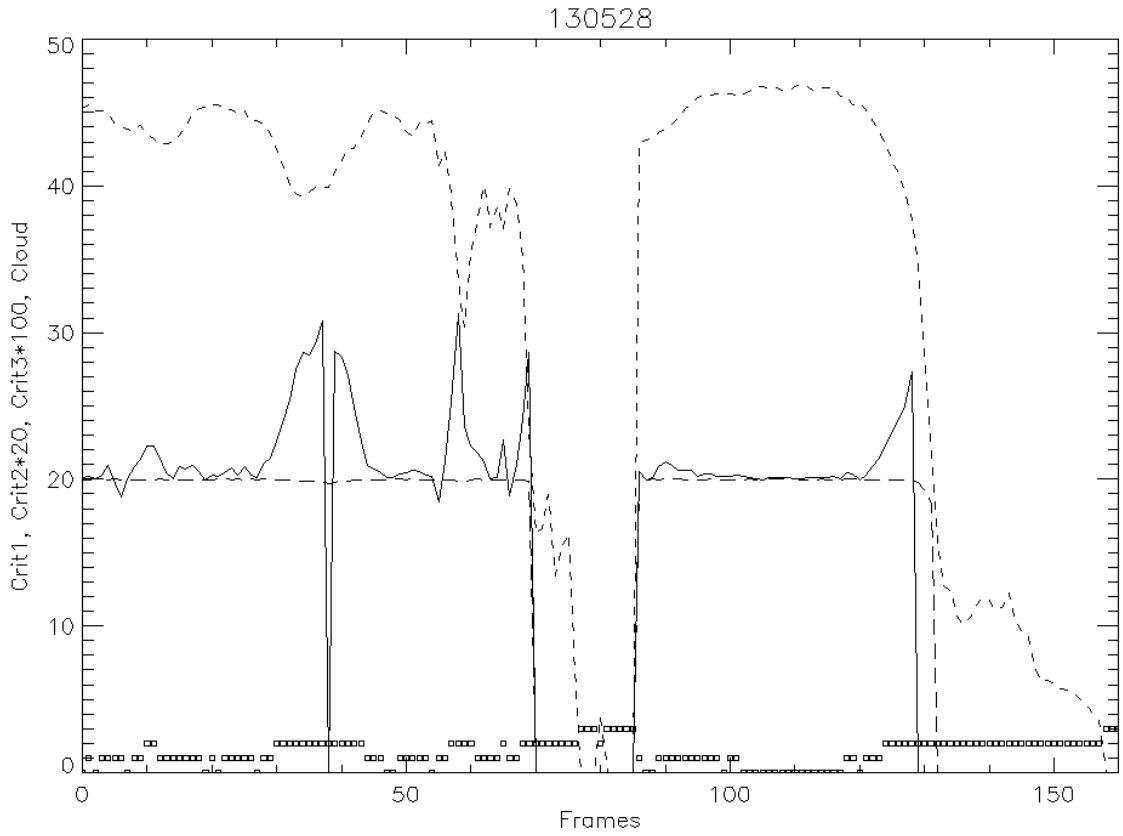

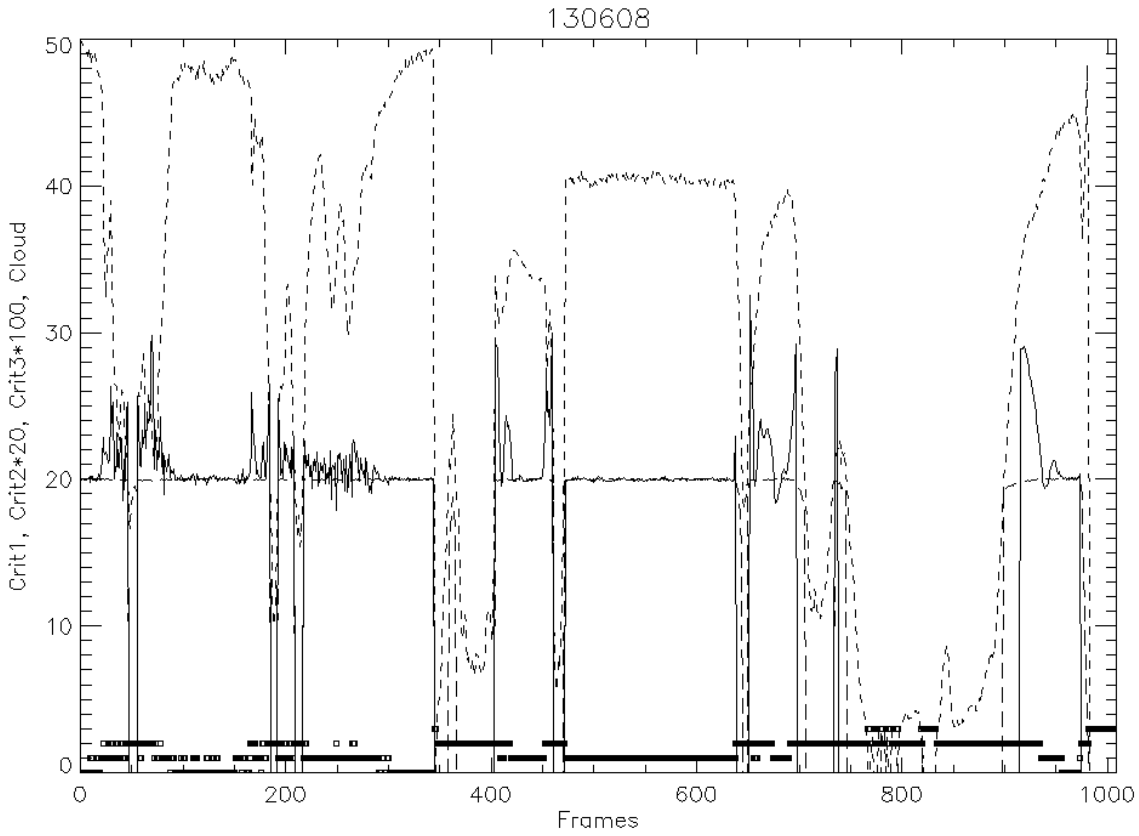
130608
Crit1, Crit2*20, Crit3*100, Cloud
Frames
0
10
20
30
40
50
0
200
400
600
800
1000

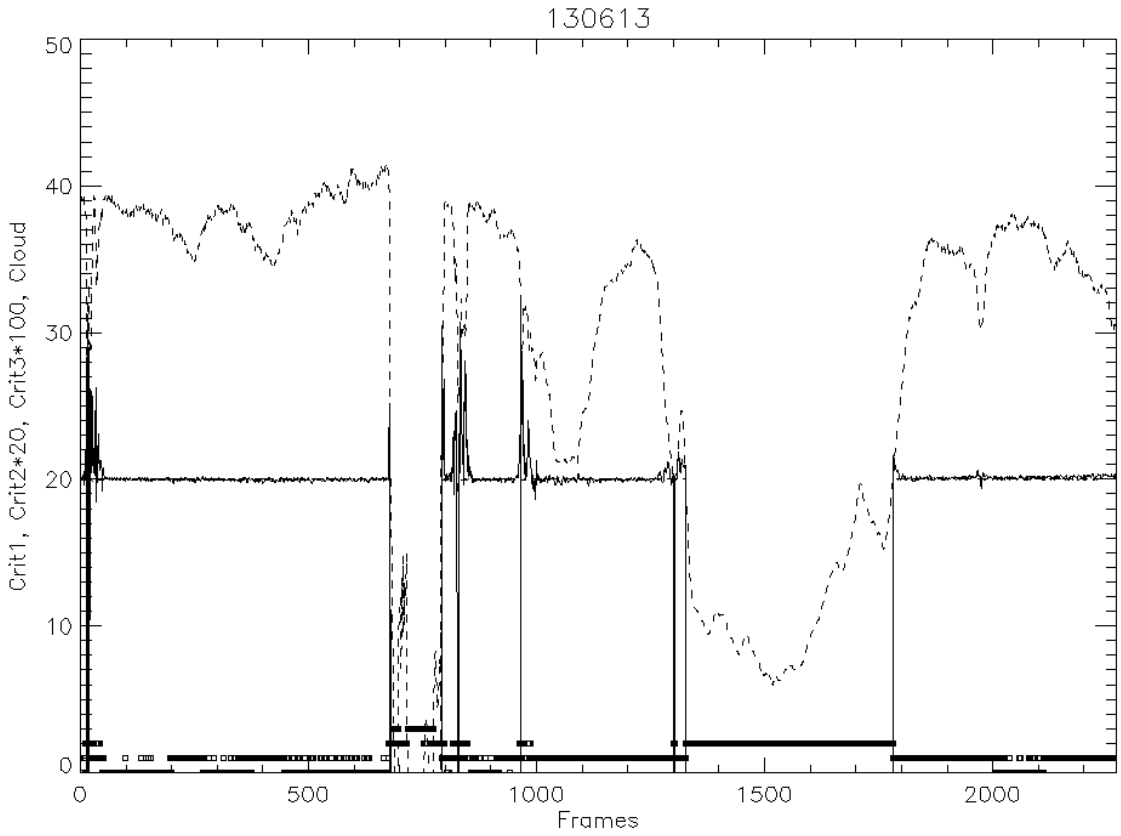

Figure 8.2 Plots of criteria and the cloud score in three data sets. *Crit1* (dashed) was set to 43 for the sets 130528, 13608 and to 37 for 130613. *Crit2* (long dash) is multiplied by factor of 20 and *Crit3* (solid line) by factor of 100. Small squares at the bottom of the plots denote the cloud score 0–3.

References

Feng, S., Lin, J., Yang, Y., et al. 2014, *Automated detecting and removing cloud shadows in full-disk solar images*, New Astronomy, 32, 24-30

ANNEX A

Computation of the exposure times and the observations cycle time uses the overall system transmission to be about 3% Table below lists the computation of system transmission.

System transmission	
M1	**0.95**
M2	**0.95**
M3/Miscell	**0.1**
Prefilt	**0.8**
FP1	**0.95**
FP2	**0.95**
Lenses	**0.9**
Polariz/Calcite	**0.5**
Total Transmission	**0.029322225**

This Table shows the passband shift across the field of view and time it takes to acquire the full data set when accounting for this shift. The different spectral channels are shown in different colors.

		FPI passband shift from center to limb (in milli Angstroms)			Scan time 2*FWHM of solar line + extra steps to compensate for FPI passband shift		
Wavelength (Angstroms)	FWHM of solar line	100mm	75 mm	150mm	100mm	75mm	150mm
3933	0.888	0.23	0.42	0.10	2.55	2.80	2.37
3968	0.517	0.24	0.42	0.10	2.92	3.39	2.58
5250	0.115	0.31	0.56	0.14	3.61	5.10	2.55
5173	0.691	0.31	0.55	0.14	2.00	2.24	1.83
5434	0.244	0.32	0.57	0.14	2.69	3.44	2.16
5896	0.612	0.35	0.62	0.16	2.24	2.60	1.99
6173	0.144	0.37	0.65	0.16	5.70	8.32	3.82
6302	0.179	0.37	0.67	0.17	4.16	5.82	2.97
6563	1	0.39	0.69	0.17	2.48	2.80	2.25
6768	0.166	0.40	0.72	0.18	4.30	6.12	3.00
5890	0.664	0.35	0.62	0.16	1.96	2.22	1.78
8542	1.617	0.51	0.90	0.23	2.15	2.36	2.00
10830	0.618	0.64	1.15	0.29	2.32	2.84	1.94
15648	0.34	0.93	1.66	0.41	3.05	4.23	2.22
				Total	13.77	16.97	11.49
					20.85	27.89	15.82
					7.52	9.43	6.16

ANNEX B

The simulation of solar spectral line observation with the FDIS dual FP etalon system. Various lines in the blue, red and IR channel are simulated. Top panels show solar FTS atlas spectrum superimposed with pre-filter profile and dual etalon FPI transmission profile.

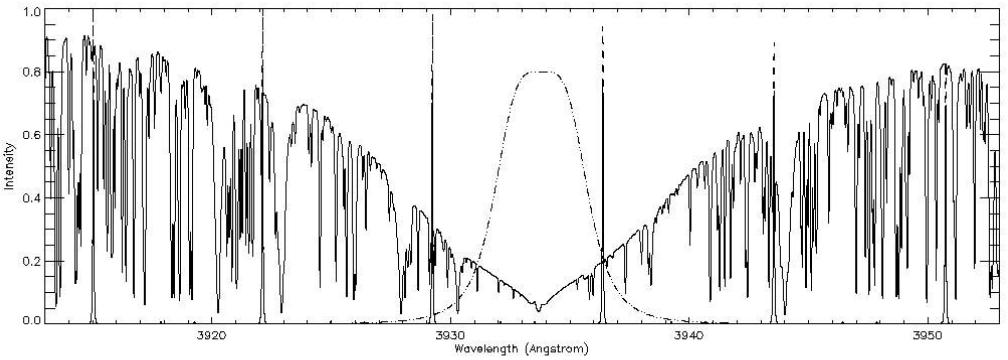
Intensity
Wavelength (Angstrom)

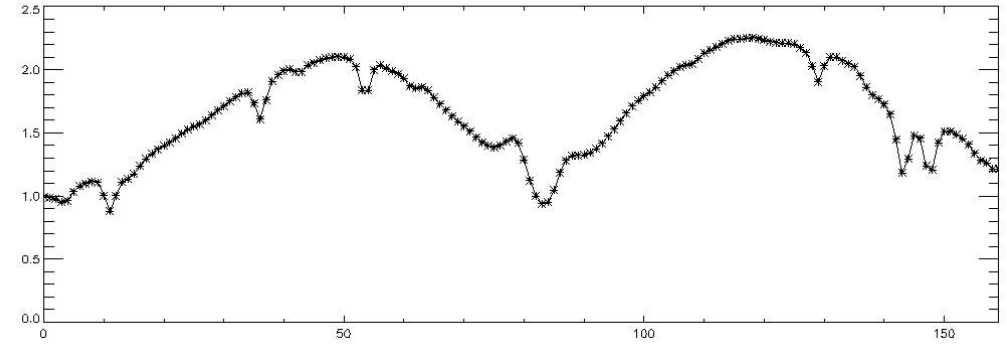

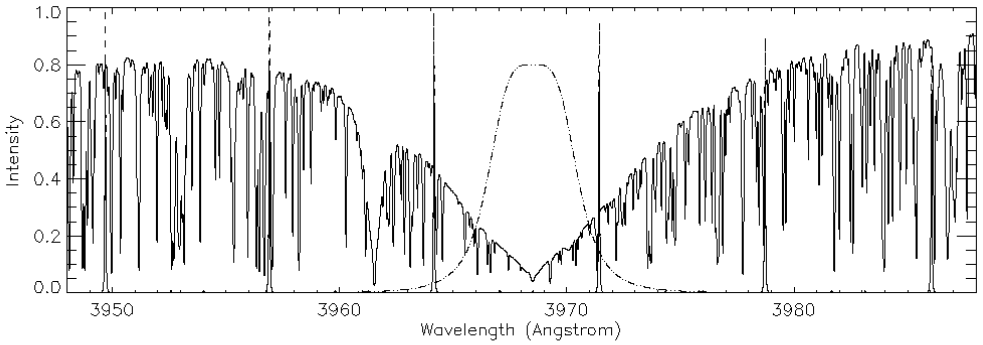
Intensity
Wavelength (Angstrom)

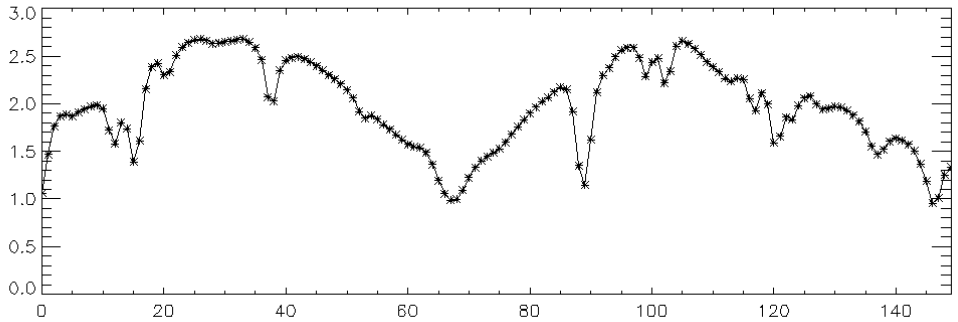

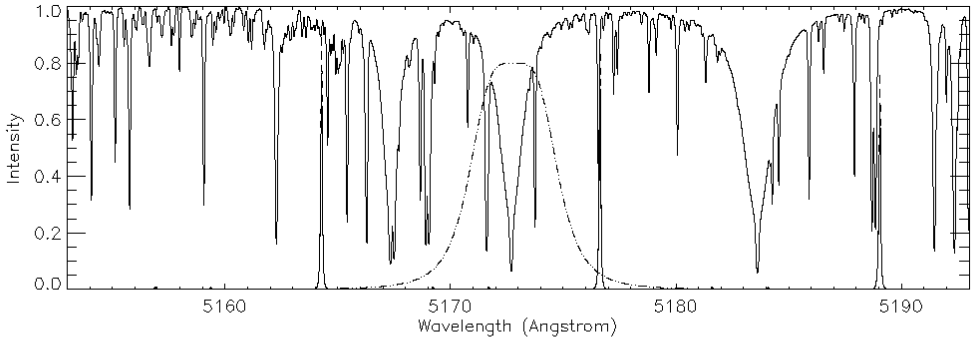
Intensity
Wavelength (Angstrom)
1.0
0.8
0.6
0.4
0.2
0.0
5160
5170
5180
5190

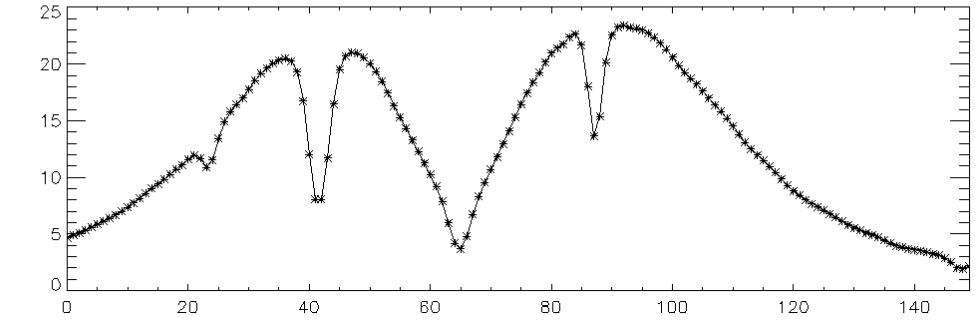
25
20
15
10
5
0
0
20
40
60
80
100
120
140

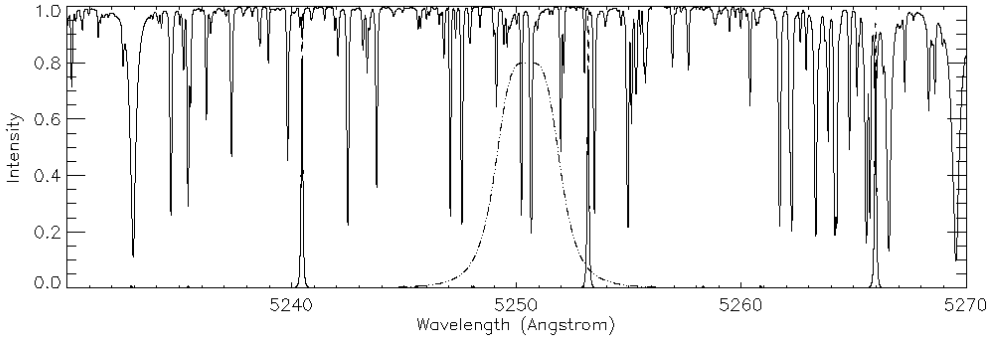
Intensity
Wavelength (Angstrom)
1.0
0.8
0.6
0.4
0.2
0.0
5240
5250
5260
5270

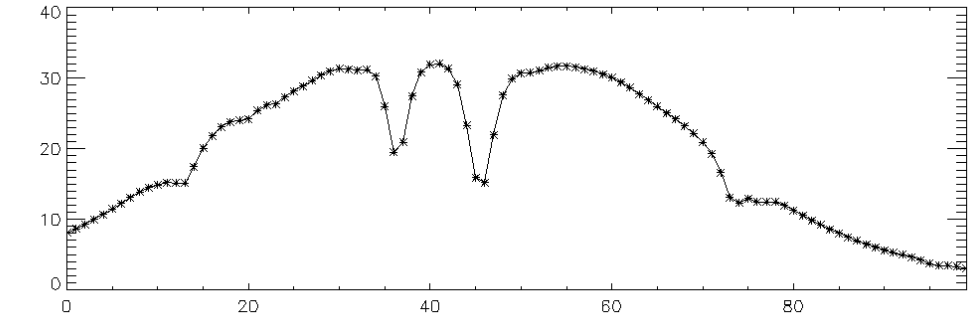
40
30
20
10
0
0
20
40
60
80

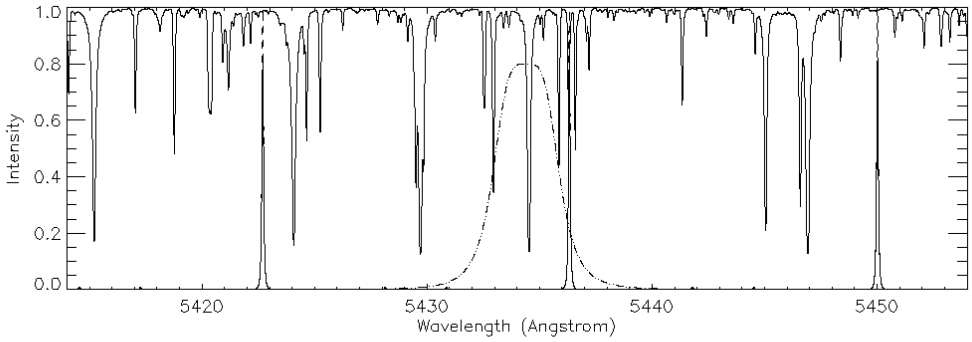
Intensity
Wavelength (Angstrom)

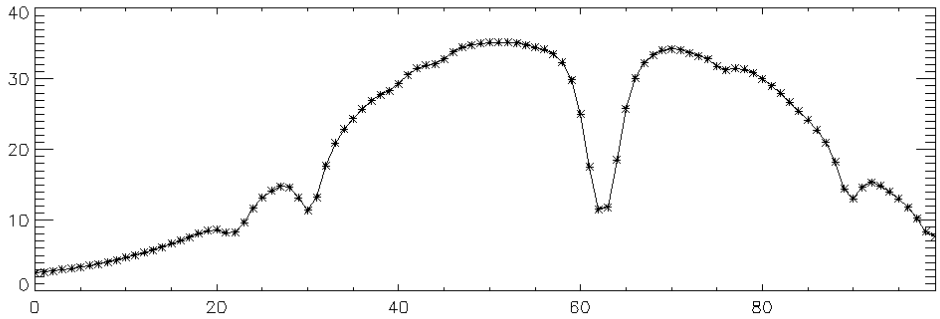

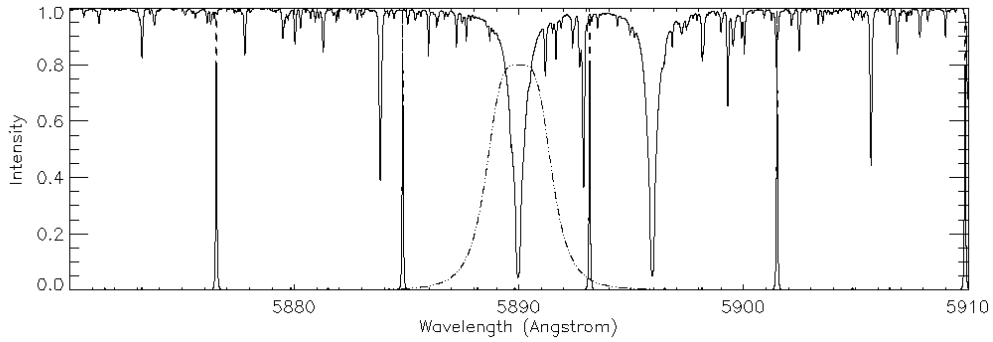
Intensity
Wavelength (Angstrom)

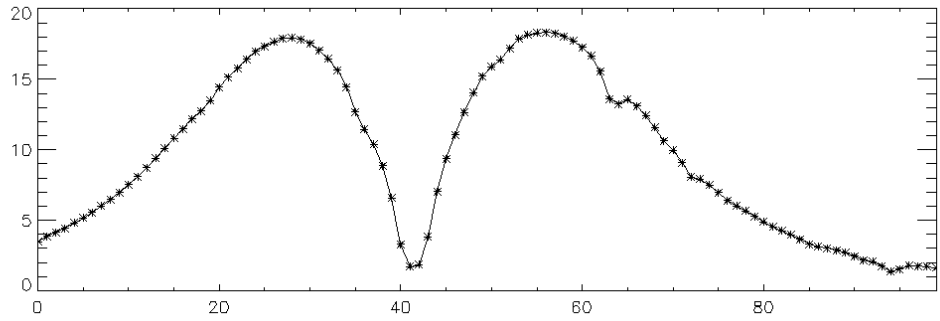

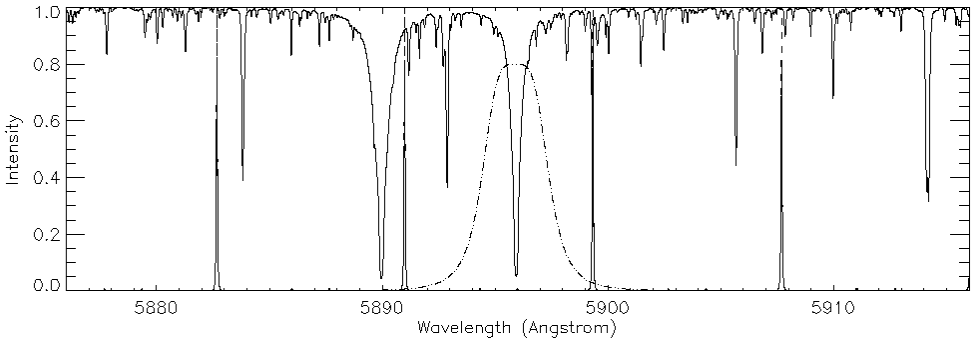
Intensity
Wavelength (Angstrom)
5880
5890
5900
5910

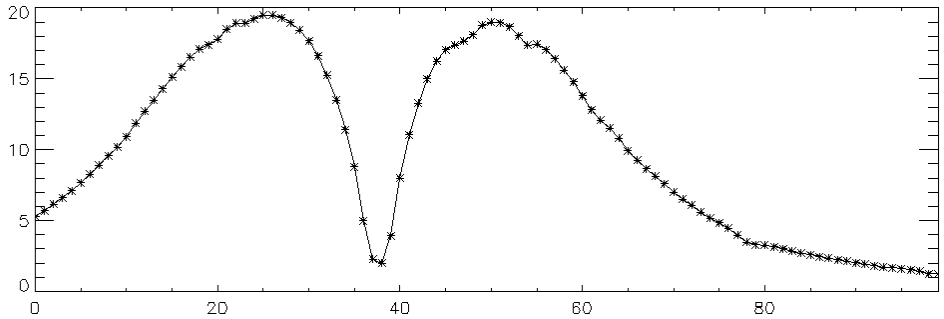

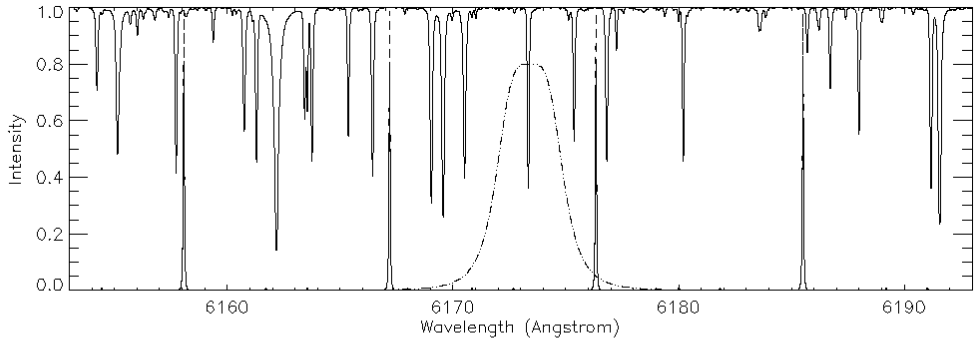
Intensity
Wavelength (Angstrom)
6160
6170
6180
6190

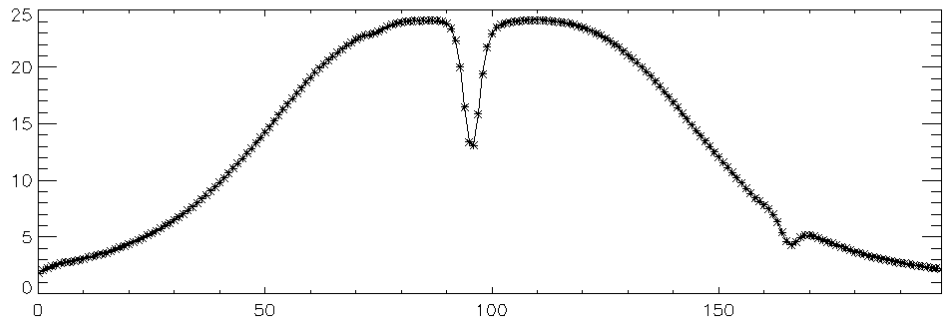

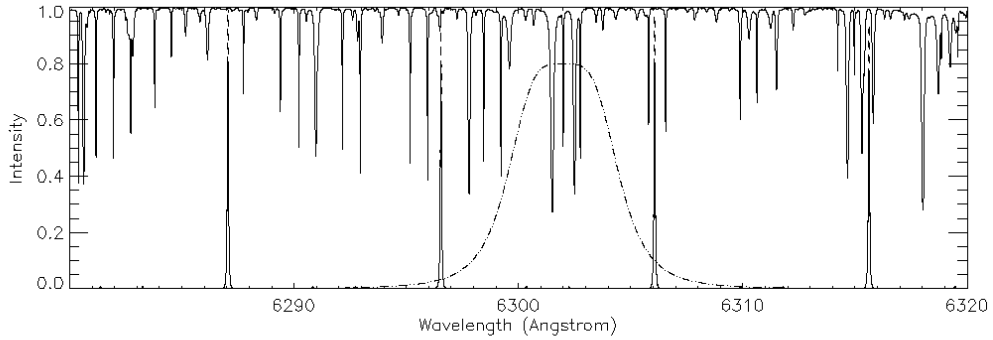
Intensity
Wavelength (Angstrom)

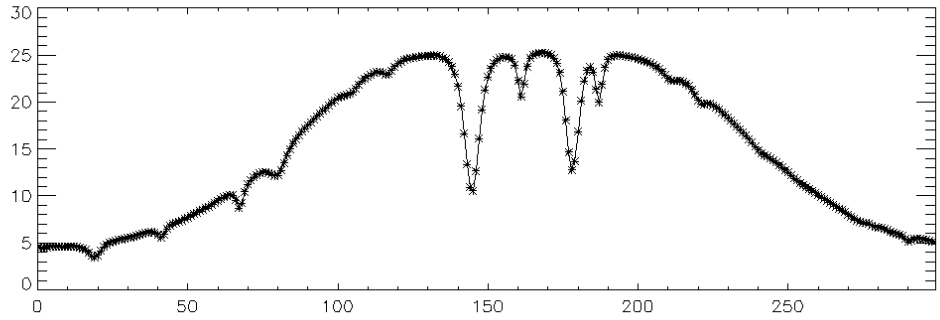

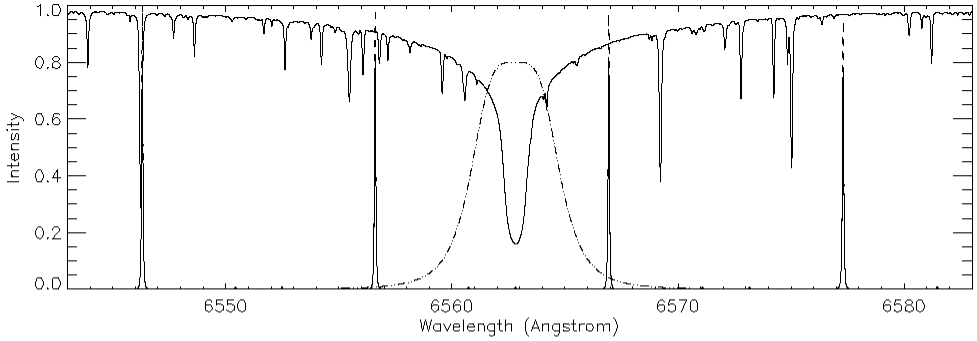
Intensity
Wavelength (Angstrom)

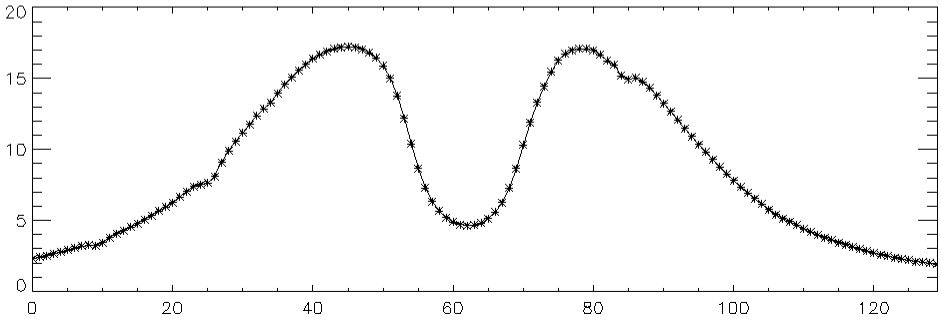

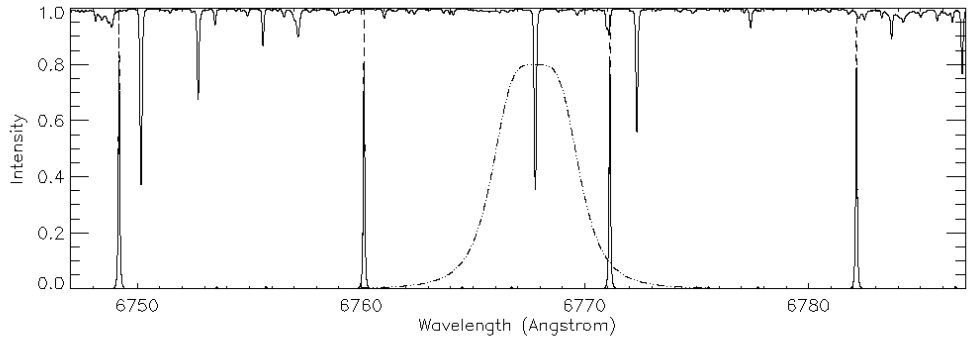
Intensity
Wavelength (Angstrom)

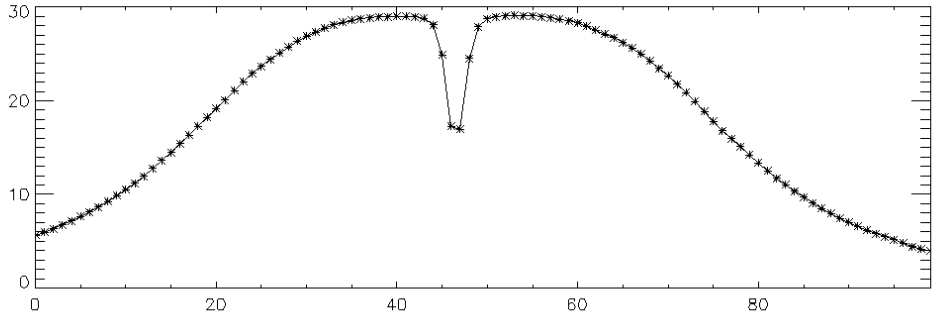

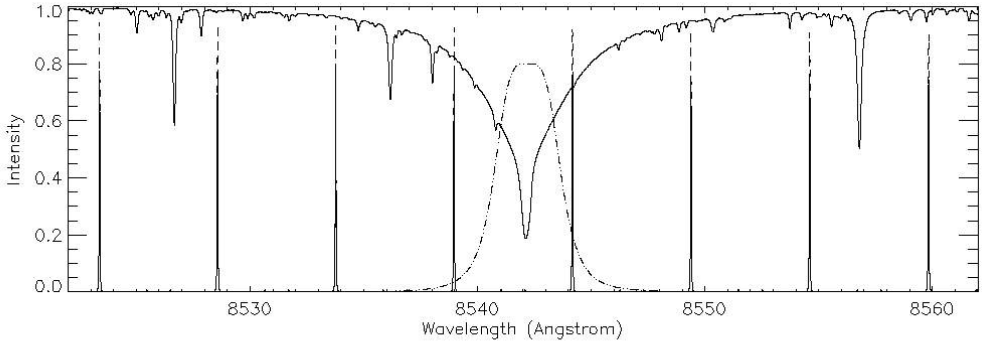
Intensity
Wavelength (Angstrom)

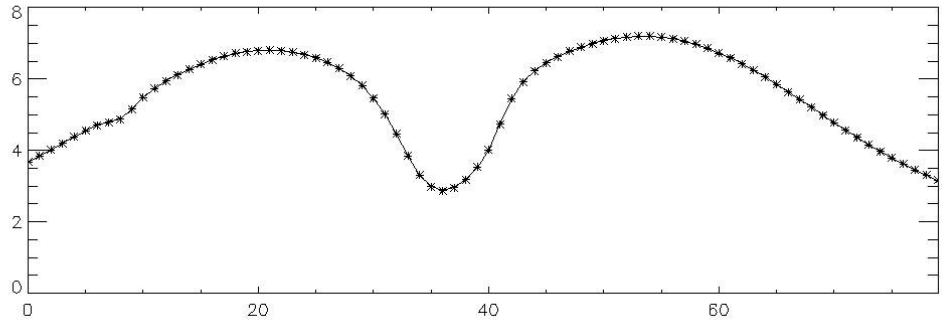

ANNEX C

The following is the listing of the cloud dection IDL program CLOUD_TEST.PRO

```
PRO cloud_test,directory,cloud,mov
;
; Test of clouds in full-disc frames in white light
;
; INPUTS: directory - frame folder name (string)
;
; OUTPUT: cloud - cloud score: 0-clean Sun, 1-weak cloud, 2-strong cloud, 3-no Sun
;         mov - movie (byte) of downscaled images with cloud score and Crit.3
;
; METHOD:
; 1. Ratio of average intensities on the disc and out of the disc (Criterion 1)
; 2. Area above an intensity threshold 0.2 / calculated full-disc area (Criterion 2)
; 3. Normalized standard deviation of disc intensity (Criterion 3)
;
; CALLED: L0B0P0.pro to calculate theoretical solar radius for a given date.
; 18 August 2016, Michal

; PARAMETERS ----------------------------

image_scale=1.8303877   ;arcsec/pixel
maxdark  =10            ;"no-Sun" threshold to avoid division by zero (counts)
minbright=20            ;minimum average I_disc / average I_nodisc

; evaluation criteria limits
cri1min =43    ;37-43, minimum average I_disc / average I_nodisc for a clean Sun
               ; - CAUTION: sensitive to exposure changes and the Sun elevation
cri2min =0.99  ;Criterion 2 shoud be close to 1 for full-disc visibility
cri2max =1.01  ;  (moreorless fixed parameters)
cri3min1=0.199 ;Criterion 3 is slightly above 0.20 for clean Sun
cri3max1=0.202 ;  (to be tuned but quite stable)
cri3min2=0.18  ;Criterion 3 limits for weak clouds
cri3max2=0.22  ;  (to be tuned)

; INPUT BLOCK ---------------------------

path='TBD'
list=FILE_SEARCH(path+directory+'\*.bmp',count=cnt)  ;list of files

; here the date is derived from the directory name:
year =2000+fix(strmid(directory,0,2))
month=fix(strmid(directory,2,2))
day  =fix(strmid(directory,4,2))
hour=12  ;fixed

; CALCULATED DISC AREA ------------------

L0B0P0,year,month,day,hour,l0,b0,p0,r0      ;L0B0P0 is an ephemeris program
rdisk_arcsec=r0*3600.                       ;disc radius in arcsec, float
rdisk_pixels=rdisk_arcsec/image_scale
ndisk=!pi*(rdisk_pixels)^2

smooth_box=rdisk_pixels/32.                 ;smoothing parameter approx. 30"

; OUTPUT ARRAYS -------------------------

crit1=fltarr(cnt)
crit2=fltarr(cnt)
crit3=fltarr(cnt)
cloud=intarr(cnt)
mov=bytarr(400,300,cnt)      ;check-movie array
window,0,xs=400,ys=300
```

```
; GENERAL LOOP ON FRAMES ---------------

for i=0,cnt-1 do begin

  ima=READ_BMP(list(i))
  ima=fix(ima)            ;conversion to integer
  imax=max(ima)           ;maximum intensity
  limit=0.2*imax          ;disc threshold (a moreorless fixed parameter)

  wdisk=where(ima gt limit,cdisk)   ;cdisk = number of Npix(I>0.2) disc pixels
                                    ;wdisk = list of Npix(I>0.2) disc pixels
  wout=where(ima lt limit,cout)     ;cout = number of out-of-disc pixels
                                    ;wout = list of out-of-disc pixels

  cr1=0   ;condition variables predefined as false
  cr2=0
  cr31=0
  cr32=0

; Criterion 1 - ratio avg. disc intensity / avg. non-disc intensity
  if imax gt maxdark then $
    crit1(i)=(total(ima(wdisk))/cdisk)/(total(ima(wout))/cout) $
  else crit1(i)=0.                  ;imax < maxdark - no Sun
  if crit1(i) gt cri1min then cr1=1    ;Criterion 1 in clean Sun range


  if crit1(i) gt minbright then begin  ;the Sun is not too much covered by clouds
; Criterion 2 - ratio Npix(I>0.2) / Npix(disc) to detect a partial cover of the disc
    crit2(i)=float(cdisk)/ndisk
    if (crit2(i) gt cri2min) and (crit2(i) lt cri2max) then cr2=1  ;full disc seen
  endif

  if cr2 then begin                 ;full disc visible
; Criterion 3 - normalized standard deviation of disc intensity to detect clouds
    sima=smooth(ima,smooth_box)         ;smoothing of the frame to remove noise
    mom=moment(sima(wdisk),maxmoment=2)  ;calculation  of  mean  mom(0)  and  variance
mom(1)
    crit3(i)=sqrt(mom(1))/mom(0)        ;stddev = sqrt(variance)
    if (crit3(i) gt cri3min1) and (crit3(i) lt cri3max1) then cr31=1
                                                ;Criterion 3 in clean Sun range
    if (crit3(i) gt cri3min2) and (crit3(i) lt cri3max2) then cr32=1
                                                ;Criterion 3 in weak clouds range
  endif

  ; EVALUATION ------------------------
  ; cloud = 0 - clean Sun
  ; cloud = 1 - weak clouds
  ; cloud = 2 - strong clouds
  ; cloud = 3 - no Sun

  if crit1(i) eq 0. then cloud(i)=3 else begin    ;no Sun
   case 1 of
    (cr1 and cr2 and cr31)        : cloud(i)=0    ;clean Sun
    (cr2 and cr32 and (not cr31)) : cloud(i)=1    ;weak clouds
    (cr2 and cr31 and (not cr1))  : cloud(i)=1
    abs(not cr2)                  : cloud(i)=2    ;strong clouds
    (cr2 and (not cr32))          : cloud(i)=2
    else                          : cloud(i)=10   ;!undefined!
   endcase
  endelse

; A MOVIE TO CHECK -------------------

  ima=congrid(ima,400,300)
  tvscl,ima
  xyouts,20,20,strtrim(cloud(i),2)+'   '+strtrim(crit3(i),2),charsiz=1.6,/device
  a=tvrd()
  mov(*,*,i)=a

; ------------------------------------
```

```
endfor    ;end of loop on frames

; OUTPUT PLOTS -----------------------

window,0,xs=1000,ys=700
plot,crit1,line=2,/xst,col=0,back=255,charsiz=1.6,title=directory, $
  xtitle='Frames',ytitle='Crit1, Crit2*20, Crit3*100, Cloud'
oplot,crit2*20,col=0,line=5
oplot,crit3*100,col=0
oplot,crit1,psym=1,symsiz=0.6,col=0
oplot,cloud,col=0,psym=6,symsiz=0.6

END
```

ANNEX D

SPRING Network Operations and Data Management:

Network Operations:

Observations:

The SPRING network will be designed to perform autonomously which means it will be programmed to automatically perform the following daily basic operations:

1. Check weather parameters and decide to observe or not.
2. Open the dome/shelter.
3. Point the telescope to the Sun and take test images to adjust exposure time, sun centering etc.
4. Initialize pre-filters, etalons, and camera
5. Perform calibrations (photometric, polarimetric and wavelength calibration)
6. Start observations
7. Take noon/intermittent calibrations and observe again
8. Take final calibrations
9. Park all optics and stages to home positions
10. Stop observations in evening
11. Park telescope and move dome to close position

Onsite processing:

The following tasks will need to be performed onsite

1. Deduce and apply quick-calibration to observations
2. Compute quick-look Dopplergrams and Magnetograms
3. Send computed Doppler and Magnetograms to central data station where real time space weather quantities will be generated.
4. On-site computers will continuously record all instrument and weather parameters and these will be displayed on a website, accessible globally, and updated at minute intervals. Parameters will be displayed graphically and list will be available via ftp.
5. Real-time images will be displayed n website also for realtime monitoring of the sun.
6. Contextual high-resolution broad-band images will be taken in a burst of 10-15 seconds and will be processed on-site for best frame selection. Using these best frames speckle reconstruction will be performed.

Data Transfer:

Daily data will be transferred over internet to central data station at the end of the day. So, there will be typically more than 12 hours available to transfer the data to central station. This will include calibration data, observations and housekeeping data such as weather and instrumental parameters. Data rate computations in section 7 shows that a compressed data of about 7 TB per day would need to be transferred. Such transfers are possible with today's hardware and bandwidths.

Data Processing:

We assume that during phase I of the project a single station prototype will be developed and will be run for about 6 months to acquire meaningful data to characterize systematics for helioseismology and magnetometry. Further, it also helps in understanding systematics due to instrumental response to varying declination angle of Sun (influence of changing gravity vector of instruments, for example.).

Such data series for 6 months, will then be processed at the central data analysis station. A software pipeline will be developed to process & analyze the data to produce the higher level data products or derived data products and make a record of physical quantities in a Synoptic chart manner. A preliminary list of derived products can be

1. Calibrated Dopplergrams and Magnetograms.
2. Synoptic charts of Magnetograms
3. Near surface horizontal flows using local helioseismology techniques
4. Synoptic maps of zonal and meridional flows.
5. Phase analysis of oscillations in different spectral lines and with intensity oscillation spectra as well.
6. Far-side imaging of the sun using acoustic holography.
7. Global coronal field models based on photospheric and chromospheric magnetic field information.
8. Non-potentiality proxies for monitoring active region field evolution.
9. Processing high resolution context imaging data for best inter-channel registration and seeing/geometric distortions.

Data Distribution:

The three streams of datasets will be available. (i) Near real-time data which is processed onsite with quick calibration procedures and is available via an onsite server. These will be available for just 10 days and will then be overwritten. Institutes that require near real-time data will be able to pull the data from these servers,

themselves. (ii) full disk science-ready registered, coaligned, inter-calibrated (between overlapping sites) Doppler and Magnetograms will be available as soon as next day after acquisition. These will be useful for studying near surface horizontal flows, especially in relation to active region evolution, (iii) calibrated long-term time series over month or three month period will be available for global seismology analysis. These will be available on from one month to three month from acquisition. Dedicated web servers will cater to each of these three data streams described mentioned above.

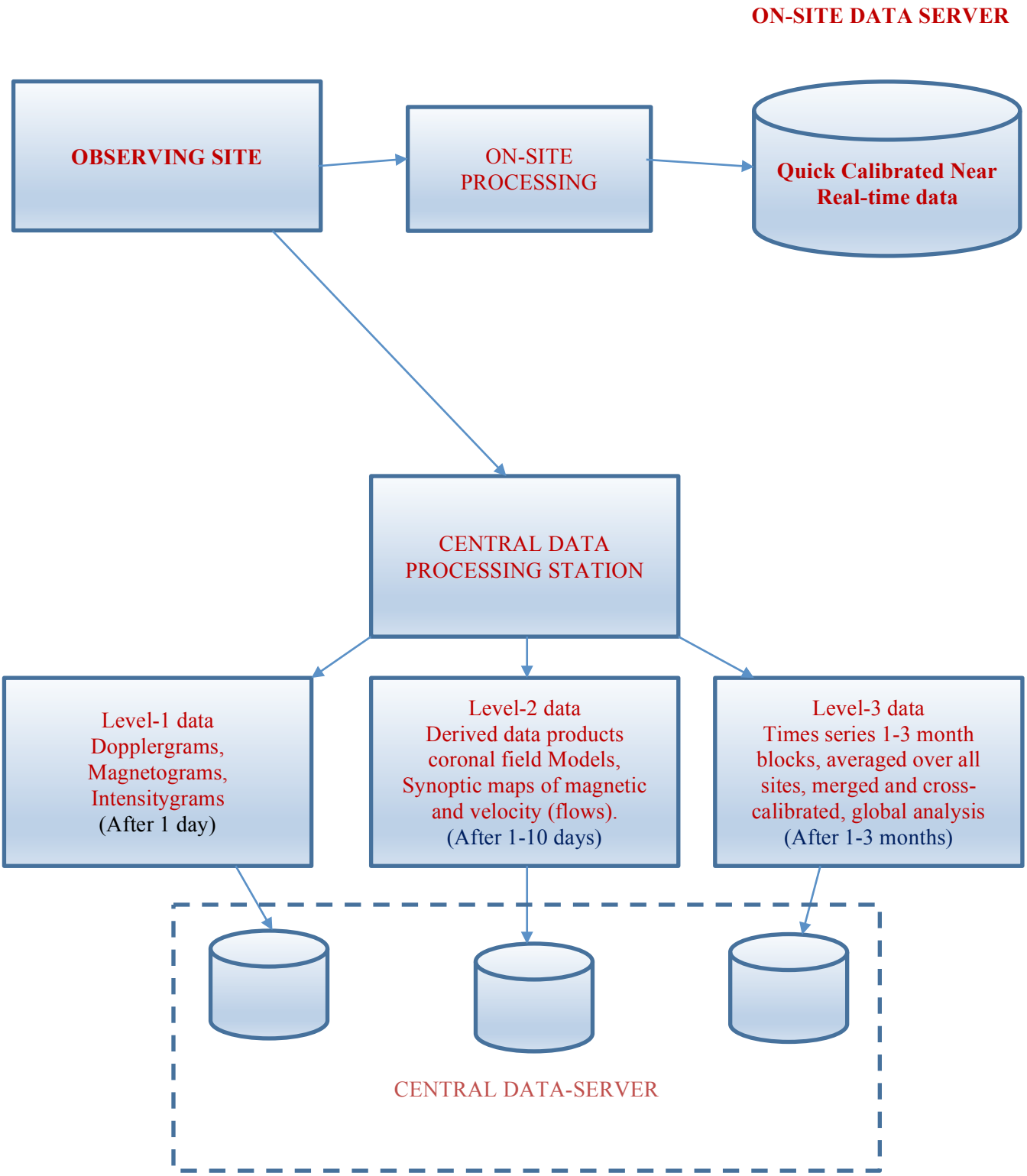
ON-SITE DATA SERVER
OBSERVING SITE
ON-SITE PROCESSING
Quick Calibrated Near Real-time data
CENTRAL DATA PROCESSING STATION
Level-1 data
Dopplergrams, Magnetograms, Intensitygrams
(After 1 day)
Level-2 data
Derived data products coronal field Models, Synoptic maps of magnetic and velocity (flows).
(After 1-10 days)
Level-3 data
Times series 1-3 month blocks, averaged over all sites, merged and cross-calibrated, global analysis
(After 1-3 months)
CENTRAL DATA-SERVER

ANNEX-E

High-Resolution Context Imager (HRCI) for SPRING

To achieve an angular resolution of ~0.5 arcsec in the visible region, 300-600 nm, requires an aperture size of about 25 cm. Thus, the FDIS telescope can also be used for the HRCI telescope.

After the filter-wheel in Fig 5.3, we do not need the FP interferometer, and the bandpass of the filters will be chosen differently. The cameras would be 8kx8k, sampling 0.25-0.3" per pixel. The cameras would be read with short exposure time of < 10 ms to freeze the seeing variations. A series of short exposure images would be taken in interference filters simultaneously with white-light images for about 10 seconds. These will then be processed for best frames in terms of frequency content and these best frames would be further processed by speckle interferometry methods to extract one high resolution image per 10 seconds per wavelength band.

Movies of these images for all bands would be made and be available via a local web server. The images would be registered between multiple bands to facilitate co-registration with small field-of-view images from the large aperture solar telescopes.